Combined Experimental and Computational Study of the Role of Promoters in Selective Hydrogenation

RUZICA TODOROVIC

B.S., University of Illinois at Chicago, 2010
M.S., University of Illinois at Chicago, 2011

THESIS

Submitted as partial fulfillment of the requirements
for the degree of Doctor of Philosophy in
Chemical Engineering in the Graduate College of
the University of Illinois at Chicago, 2016

Chicago, Illinois

Defense Committee:

Randall J. Meyer, Chair and Advisor
Jeffrey T. Miller, Purdue University
Christopher L. Marshall, Argonne National Laboratory
Ludwig C. Nitsche, Chemical Engineering
Robert F. Klie, Physics

ACKNOWLEDGMENTS

For the last four years, the meaning of the word “impossible” has changed. I have seen that no obstacle too big exists if it is worth the effort. This was worth it, as from this point on I get to spend the rest of my life learning and exploring. I owe it all to my advisors Dr. Randall Meyer, Dr. Jeff Miller and Dr. Chris Marshall.

First, I would like to thank Dr. Meyer, for being there since the beginning. He is warm-hearted to people, enthusiastic to work and an inspiring and brilliant researcher. Dr. Miller’s wealth of knowledge in the field of heterogeneous catalysis and Dr. Marshall’s expertise in reactor process and design were invaluable to my success. However, it is the desire with which they unselfishly and enthusiastically help a student in need that will forever be appreciated. Their strict and meticulous attitudes toward research have inspired me greatly and have opened my eyes to the challenges associated with experimental and computational work. I am truly a better scientist because of them.

I would like to thank my other committee members Dr. Robert Klie and Dr. Ludwig Nitsche for their time and expertise. I have been blessed with so much and at the end; it was your help that had lead me across the finish line. Thank you for supporting my aspirations.

I would never have accomplished any of this if not for the support of my family and friends. To my brother Radoslav, your unconditional love and support are the reason my dream has come true.

Thank you all,

Ruzica

TABLE OF CONTENTS

LIST OF TABLES

LIST OF FIGURES

LIST OF FIGURES (continued)

LIST OF ABBREVIATIONS

APS	Advanced Photon Source
CN	Coordination Number
CoIWI	Co-Incipient Wetness Impregnation
DFT	Density Functional Theory
EXAFS	Extended X-ray Absorption Fine Structure
fcc	Face Centered Cubic
FTIR	Fourier Transform Infrared
GC	Gas Chromatograph
IR	Infrared
IWI	Incipient Wetness Impregnation
mIWI	Modified Incipient Wetness Impregnation
MRCAT	Materials Research Collaborative Access Team
mSEA	Modified Strong Electrostatic Adsorption
OD	Outer Diameter
PZC	Point of Zero Charge
SAA	Single Atom Alloy
SEA	Strong Electrostatic Adsorption
STEM	Scanning Transmission Electron Microscopy
TEM	Transmission Electron Microscopy
TOF	Turnover Frequency
UIC	University of Illinois at Chicago
XANES	X-ray Absorption Near Edge Spectroscopy

SUMMARY

Specific physical (i. e. morphology, mechanical strength) and chemical requirements have to be satisfied to develop an appropriate heterogeneous catalyst. Chemically a catalyst has to exhibit high activity and selectivity to desired product with thermal and mechanical stability under typical reaction conditions, and very often requiring a high surface area support that can achieve optimal dispersion of an active component. In general, these requirements are fulfilled by determination of the active metal, its consequent modification to achieve desired reactivity, i.e. promotion, and finally, achieving all of the above through an exact synthesis and pretreatment methodology.

Heterogeneous catalysts often require relatively high temperatures and pressures, and have complex reaction mechanisms that can lead to wide product distribution. Heterogeneity is usually present due to a broad size distribution of the supported metal particles with irregular morphology. This can produce multiple types of active sites, which can significantly alter the reactivity of the catalyst. Additional complications arise in bimetallic catalysts, i. e. metal alloys, due to variations in the bulk and surface composition with the possibility of different oxidation states of both metals, as well as the existence of various alloy phases. Metal alloys can exhibit properties that are quite different from their constituent atoms (ligand, strain and ensemble effects), and as such can substantial alter product distribution, reaction rates or pathways [1, 2]. As such, elucidation of reaction mechanism on supported metal catalysts is rarely straightforward. Alloying often targets dilution of an expensive, active component of the catalyst, usually noble metals, within a more inert, lower cost host metal [2]. Metal alloys can contain various active sites that can efficiently catalyze multiple steps in reaction mechanism. This makes them vary suitable for processes requiring dissociation of molecular hydrogen for

subsequent hydrogenation of various surface bound species (aldehydes, ketones, aromatic rings, CO, CO_2, etc.).

This study provides a systematic insight into the observed catalytic performance of the Pd promoted Ag nanoparticles on SiO_2 support for α,β-unsaturated aldehyde hydrogenation to allyl alcohol, and of V promoted Rh surfaces for CO hydrogenation to C_{2+} oxygenates. It addresses a fundamentally important and interesting problems of regioselectivity with respect to selective hydrogenation of C=O bond vs. C=C bond in unsaturated aldehydes, and with respect to metal-oxide interface mediated hydrogen-assisted CO dissociation vs. the direct CO dissociation mechanism.

1. EXPERIMENTAL STUDY OF SINGLE ATOM ALLOY Pd-Ag CATALYST FOR SELECTIVE HYDROGENATION OF ACROLEIN

1.1 Introduction

Understanding a physical relationship between a promoter and the active metal is decisive to tuning the selectivity of the catalyst. Selectivity can be effected with the nature of the active metal and/or promoter (second metal or metal oxide), particle size and the support [3, 4]. Heterogeneous nanoparticle catalysts consist of various active sites that are very diverse in energetics, activity and selectivity due to the varying morphology of the surface. As such, active sites are nearly impossible to identify and characterize as even a simplistic, single crystal surface contains multiple types of adsorption sites [5]. In addition, nanoparticles are not necessarily identical in size or composition.

Selective hydrogenation of unsaturated aldehydes is an example of a reaction mechanism that exhibits dependence to all of these effects [3]. For acrolein, the simplest α, β–unsaturated aldehyde, selective hydrogenation to α, β–unsaturated alcohol is particularly difficult (Figure 1). This is due to absence of substituents on olefinic bond that hinder the coordination to the surface and in turn promote adsorption via carbonyl bond. As such, it is desirable to find the catalyst, which may control the intermolecular selectivity by preferential hydrogenation of the C=O bond.

Commonly used hydrogenation catalysts (Pt, Pd, Ir, etc.) are very active but not selective to allyl alcohol (the desired product). Pt is not intrinsically selective to produce unsaturated alcohols, although high selectivities to unsaturated alcohols have been exhibited, but are very dependent of the structure of the reactants. Monometallic Ir catalysts are selective to unsaturated alcohols, but very inactive [6-9]. Instead, the primary metal of choice is Ag (or Au), which has been shown to exhibit higher selectivity but low activity [10-12]. The low activity has been

associated with the electronic structure of the Ag atom (filled *d* band). However, it has been confirmed by isotope jumping technique that hydrogen can dissociatively adsorb on Ag [13], and that silver is able to adsorb conjugated double bond via bifunctional bonding to both C=C and C=O bond [14]. Fujii et al. used Infrared Reflection Absorption (IRA) spectra and *Ab initio* MO calculations to show that acrolein adsorbs on the silver substrate in *trans* configurations. C=O bond was shown to be coordinated to the positively charged sites of ad-atom and/or kink sites, while both the C=C and C=O bonds were shown to interact with positively charged sites of the silver substrate [15].

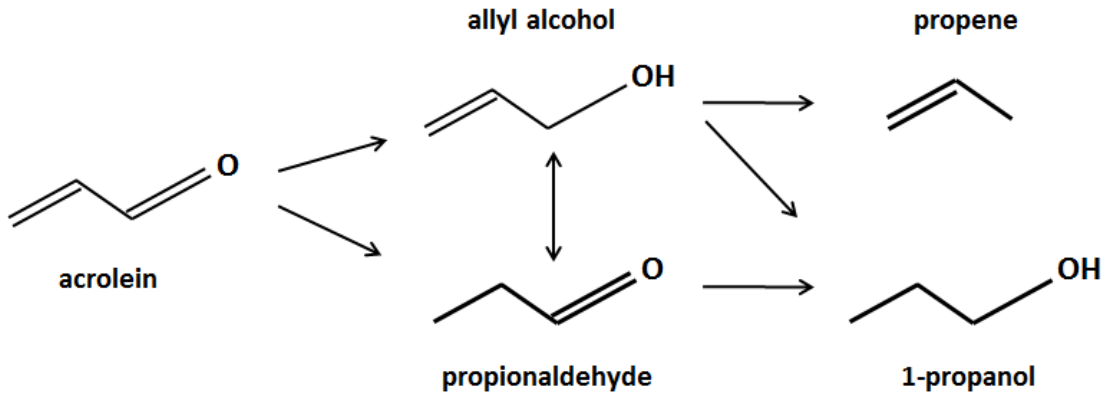

Figure 1. Reaction scheme for the hydrogenation of acrolein.

Wei et al. performed a detail investigation of the pressure and particle size effect of the Ag/SiO_2 catalyst for the selective hydrogenation of acrolein [12]. The reaction was shown to be surface sensitive, as the selectivity to allyl alcohol increased (from 15 to 37%) with an increase in particle size (from 1 to 9 nm), at 5 atm pressure. Higher selectivity was ascribed to the adsorption geometry of acrolein on larger particles, suggesting that low Miller index surfaces are important for selective hydrogenation of acrolein [12]. In addition, selectivity increased with an

increase in pressure (from 1 to 5 atm). It was proposed that at low pressure, the acrolein molecule will adsorb parallel to the surface whereas at high pressure the adsorption geometry would shift such that C=O bond would be accessible to the surface [12].

Similarly, Boron et al. [16] analyzed the effects of pressure (7.5 mbar to 20 bar) on the gas phase hydrogenation of acrolein over 7.5% Ag/SiO_2, determining that at low pressures high propionaldehyde selectivity is dominant, while at higher pressures increase in the selectivity to allyl alcohol was observed (42%). *In situ* XAS at 7.5 mbar showed a hydrogenated propionaldehyde-like surface species, orientated parallel to the surface. It was suggested, that the preferential adsorption of acrolein through the carbonyl group could be accomplished by further increases in the partial pressures of the reactants, i.e. higher surface coverage, or with the use of defect rich Ag surface [16].

The activity of the catalyst can exhibit large dependence on the surface crystalline anisotropy, due to different facets in clusters with varying size. This effect is substantially exacerbated for particles < 10 nm [17]. For silver nanoparticles supported on silica catalyst, larger particle size, i.e. higher fraction of the (111) plane, favors the selective adsorption and activation of the C=O bond. On the other hand, saturated aldehyde is produced on the (100) plane because both the C=C and the C=O bonds could be simultaneously adsorbed and activated. The shape of these small particles is thermodynamically determined by the surface energy. For fcc metals, such as Ag, Pd and Pt the stability of the surface plane decreases in the order (111) > (100) > (110) [2]. For supported metal particles, a compromise between exposing only the lowest energy surface planes and minimizing the surface area, results in a cubooctohedral particle (eight (111) and six (100) surface planes) [2]. The atoms in the middle of the (111) face have a coordination number (CN) of 9 and the atoms in the center of the (100) surface have a CN

of 8. In systems where the interaction between the metal particle and the support is relatively weak, so that the wetting of the particle due to strong metal-support interaction can be prevented, some atoms can have even the lowest CN of 6 (atoms at the intersection of a (100) plane with two (111) [18].

Very small particles can expose sites not present on the large ones and vice versa. They can suppress the population of certain adsorption species [19]. As can be seen, a decrease in particle size decreases the coordination of surface atoms, which will increase the surface free energy resulting in a more active surface. The strength of the interaction of acrolein with the surface and the adsorption mode may affect the selectivity of the hydrogenation. For instance, a strong interaction of the C=C bond with the surface may impede desorption of unsaturated alcohols leading to fully saturated alcohols. In contrast, when too weak (as on Ag) surface C=C bond predominantly undergoes hydrogenation to a saturated aldehydes. As the selectivity on Ag decreases at smaller particles, it follows that more active sites of Ag do not dominate the hydrogenation process [20].

Therefore, for selective hydrogenation to allyl alcohol, promotion is necessary in order to change the local surface structure (i.e. new active sites) of the monometallic Ag particle. Alloy formation in bimetallic catalysts was shown to be beneficial for high chemoselectivity [21, 22]. Addition of small amounts of atomically and uniformly dispersed elements, which independently are not catalytic, can have a profound effect on the selectivity and activity of the catalyst. The loading of the promoter metal is generally low to avoid conjugate particles and/or creation of metal islands and nanoparticles. By doping individual atoms of a second metal, monometallic catalysts will obtain new properties, while the electronic and/or structural characters of the host metal should remain the same, retaining the preexisting active sites and their properties. This is

an example of an ensemble effect, present in bimetallic surfaces, which states that only the structure and composition nearest to the adsorption sites are crucial for interaction with these sites [23, 24]. For single atom catalysts, this effect is exacerbated (i.e. highly active valence electrons) as the surface free energy of metal species reaches a maximum, which then leads to promoted chemical interactions with the support and unique chemical properties of single atom catalysts with different adsorption characteristics [17]. For example, Bemasek et al. [25] reported that H_2 adsorption and dissociation occur more efficiently at low coordination sites on platinum.

The superior performance of an isolated single atoms of Pd on graphene, prepared by atomic layer deposition technique was shown in a recent study by Yan et al. [26]. The catalyst exhibited 100% selectivity to 1,3-butadiene at 95% conversion [26]. It was suggested, that the change in the adsorption mode of 1,3-butadiene (mono-π-adsorption) promoted 1,2-hydrogen addition to form 1-butene, in addition enhancing steric effects due to higher density of adsorbed 1,3-butadiene on the isolated Pd atoms [26].

Dispersion of the active sites has been shown to be imperative to the reactivity of the catalyst [27]. Shannon et al. grafted isolated Mo (VI) active sites onto the inner surface of MCM-41 and tested the catalysts for oxidative dehydrogenation of methanol to formaldehyde (0.03 - 4 mol% Mo). The sample with the most diluted Mo (0.03 mol%) was the most active and the most selective catalyst. The authors believed that higher dispersion of active sites benefited the reaction rate [27].

Sykes et al. have shown a method for formation of a highly dispersed and uniform catalyst, by evaporation of small amounts of Pd, which released single Pd atoms that embedded themselves onto a Cu metal surface [28-31]. They reported a more effective hydrogenation catalyst, termed Single atom alloy, which when compared to denser mixtures of Pd and Cu

showed less susceptibility to poisoning. In their collaboration with Kyriakou et al., they tested a 0.01 and 0.1 ML of individual Pd atoms deposited on Cu(111) surface using hydrogenation of acetylene and styrene as their test reactions [28]. Using STM they were able to identify the presence of H atoms on 0.01 ML Pd/Cu(111), indicating that isolated Pd atoms were able to dissociate hydrogen molecules to H atoms which then spilled over to the Cu surface [28]. TPR results showed improvement in selectivity of acetylene hydrogenation to ethene (as opposed to overhydrogenation to ethane) on Pd/Cu(111) surface [28]. The selectivity to ethene for acetylene hydrogenation was greater than 95% on 0.01 ML Pd/Cu(111) with a substantial decrease to 33% on 1 ML Pd/Cu(111) [28].

In a different study by Aich et al., isolated atoms of Pd dispersed on Ag/SiO_2 catalyst were used in the selective hydrogenation of acrolein [32]. A significant change in selectivity of Ag/SiO_2 catalyst was observed by modulating the dopant concentration at very low levels [32]. EXAFS results demonstrated that when the concentration of Pd was as low as 0.01 weight percent, Pd was completely dispersed as isolated single atoms in Ag nanoparticles. The activity for the hydrogenation of acrolein was improved due to the creation of sites with lower activation energy for H_2 dissociation [32]. In addition, for the same particle size, 0.01%Pd alloyed $8\%Ag/SiO_2$ catalyst exhibited higher selectivity than their monometallic counterparts, suggesting that the Pd atom may act as a site for the favorable bonding of the acrolein molecule for facile hydrogenation of the aldehyde functionality [32]. However, even a loading of 0.05 wt% Pd resulted in a substantial loss of selectivity which was proposed to be due to the presence of contiguous Pd atoms resulting in unfavorable bonding configuration for acrolein [32].

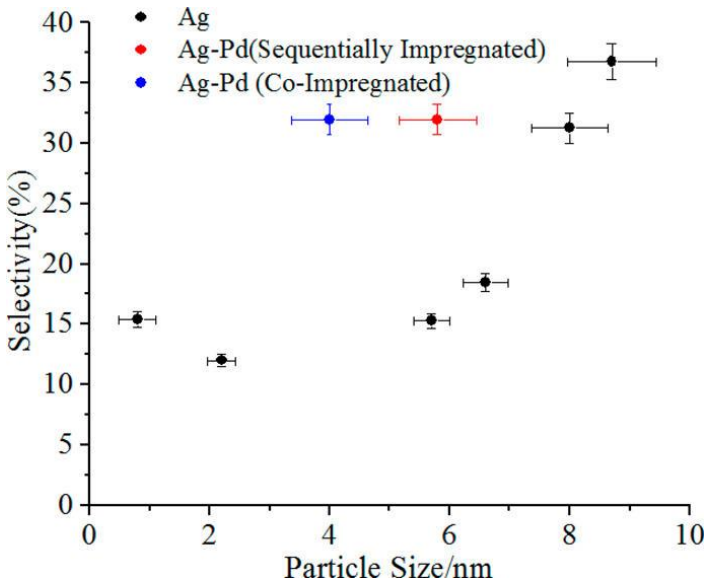

Figure 2. Comparison of selectivities toward allyl alcohol of Pd−Ag alloys and pure Ag catalysts with various particle sizes [12, 32].

Due to the atomic-scale heterogeneity, further fundamental understanding of the nature of promotion via Pd-Ag alloys is required. Conversely, a non-reducible support such as SiO_2, which is shown to be an inert in hydrogenation of acrolein, will provide means of extrapolating only the promotion effects (alloying and/or particle size), without consideration of the active sites present due to strong metal-support interactions. It should be noted, that Ag on reducible supports, such as TiO_2, has been shown to improve the selectivity to allyl alcohol [33-35], and that H_2 dissociation was suggested to occur over the SiO_2 support and migrate to the Ag nanoparticles via reverse spillover (activation over SiO_2 was much slower than that over Ag) [10].

As such, alloying with isolated Pd atoms can provide an active site for efficient dissociation of molecular hydrogen and subsequent spillover [28-31] onto the Ag surface, and possibly an active site that preferentially adsorbs the carbonyl bond of acrolein to the surface. This study provides details of the synthesis, characterization, reactivity, and the reaction mechanism of Pd-Ag alloys on SiO_2 support. Evidence for formation of single site Pd-Ag alloys

is presented, along with elucidations of catalysts performance with respect to particle size, metal loading and dispersion of the alloying metal.

1.2 Experimental Methods

1.2.1 Catalyst Synthesis

Catalysts of varying particles sizes containing different concentration of Pd, Pt and Ir (0.01 to 0.05 wt%), and Ag (8 to 12 wt%) metals on the SiO_2 support (silica gel, Sigma-Aldrich, 35-60 mesh, 285 m^2/g, 1.1 pore volume) were synthesized. Catalysts were synthesized via incipient wetness impregnation (IWI) and strong electrostatic adsorption (SEA) methods using $Ag(NO_3)$, $[Pd(NH_3)_4](NO_3)_2$, $[Pt(NH_3)_4](NO_3)_2$ and $[Ir(NH_3)_5Cl]Cl_2$ as precursors (metal salts). In IWI (or dry impregnation), the volume of the aqueous solution containing metal-precursor(s) is equal to the pore volume of the support. Capillary action draws the solution into the pores; all the metal in solution will go onto the surface due to lack of excess liquid. In SEA (or wet impregnation), excess solution is used to target the final pH to the pH range in which the electrostatic interaction is the strongest, in turn enhancing the uptake of the metal precursor. The SEA method requires an appropriately charged metal precursor based on the point of zero charge (PZC) of an oxide support and the pH of the solution [36]. The hydroxyl groups on the surface of the oxide support will protonate or deprotonate depending on the pH of the solution relative to the PZC of the support. Precursors can then be selected that will have the opposite charge as the support at a certain pH value and so the electrostatic interaction between the support and the precursor leads to strong binding of the metal precursor to the surface [36].

With respect to these methods, the procedures used to synthesize the bimetallic catalysts in this study are referred to as follows: co-incipient wetness impregnation (CoIWI), modified

incipient wetness impregnation (mIWI) and modified strong electrostatic adsorption (mSEA). CoIWI is a dry impregnation method in which an aqueous solution containing Ag and alloying metal precursors are mixed together prior to impregnation and then adsorbed on the surface at the same time. This limits the nucleation of Ag as it increases the interaction with the support as oppose to alloying metal (Pd, Pt or Ir).

In mIWI, all the steps are the same as in CoIWI with the exception that the pH of the solution needs to be adjusted (pH > 11) before the impregnation. This method enhances the interaction of the precursor with the support as the alkalinity of the solution could deprotonate the hydroxyl groups on the support surface and help disperse the precursor. The procedure for Pd alloyed Ag catalysts consists of dissolving the $Ag(NO_3)$ in water (amount varies depending on metal loading) and adding 30% NH_4OH solution drop by drop to first precipitate and then re-dissolve the precursor ensuring that the final pH of the solution is around 11. A separately prepared $Pd(NH_3)_4(NO_3)_2$ solution is then combined with the Ag solution and additional water is added so that the total volume of the solution equals the amount required to fill up the support pores.

In mSEA, first Pd metal is deposited on the surface using the SEA procedure with subsequent deposition of Ag metal via mIWI. An excess amount of water is added to SiO_2 and enough NH_4OH for the final pH=12. The mixture is vigorously stirred for 5 min. Water and NH_4OH is added to $Pd(NH_3)_4(NO_3)_2$ solution and then added to the silica suspension liquid. Additional stirring for 10 min will allow the Pd precursor to adsorb on the silica surface upon which it is filtered and rinsed with water for 3 times. The solution is then dried in the hood for 2 hours and overnight in the drying oven (125 °C). An appropriate amount of $Ag(NO_3)$ is dissolved in water and 30% NH_4OH solution is added drop by drop to first precipitate and then

re-dissolve the precursor at pH > 11. Enough water is added so that the total volume of the solution equals the amount required to fill up the support pores, upon which a sequential impregnation of the catalyst is performed.

Upon deposition of the precursors, all samples were dried in the hood (2 hours) and in the oven (125 °C for 1 day). Further, a combination of post-treatments was carried out on each sample. Treatments such as reduction and/or calcination are required to remove the salt ligands and produce metallic particles. Steaming was used to increase the particle size. During these temperature-controlled post-treatments, mobility of the surface particles can be affected causing sintering of particles or the change in the dispersion of the catalyst. As such, particles of different sizes at any given metal loading can be produced through thoughtful selection of the synthesis conditions.

The calcination was performed for 3 hours at 550 °C (on catalyst prepared via mIWI and mSEA) and 2 hours at 400 °C (on catalyst prepared via CoIWI) in a furnace open to the atmosphere but without flow. The reduction treatments were performed in a tube furnace with a 50 mL/min flow of 3.5% H_2 for 2 hours at 325°C. After calcination, catalysts prepared via mIWI and mSEA methods exhibit small particle sizes, which were increased by subsequent steaming at 350 °C or 500 °C for 2 hours. Steaming treatments were performed by flowing 50 mL/min of 3.5 %H_2 in He through the saturator preheated to 55 °C as such providing about 15% water vapor in total flow. The flow was brought to the reactor at the steaming temperature.

1.2.2 Catalyst Characterization

Characterization is performed by analyzing the EXAFS (Extended X-ray Adsorption Fine Structure) spectra, and TEM (Transmission Electron Microscopy) and STEM (Scanning

Transmission Electron Microscopy) images. TEM/STEM results are used to calibrate the relationship between the observed particle size and the average particle size (EXAFS). Selected catalysts were analyzed via both techniques and the established correlation between the two methods was used to support the reported particle sizes obtained only by EXAFS.

1.2.2.1 Extended X-ray Adsorption Spectroscopy

EXAFS (Extended X-ray Absorption Fine Structure) was adopted as a powerful and efficient tool to estimate particle size. EXAFS spectra were taken at the beamline of the Materials Research Collaborative Access Team (MRCAT, 10-ID) at the APS (Advanced Photon Source), Argonne National Laboratory. The experiments were performed in transmission mode at Ag edge. For Pd edge the experiment was performed in the fluorescence mode, which enhances the sensitivity by orders of magnitude over transmission EXAFS [37]. Fluorescence EXAFS measurements were made using a log-spiral-bent silicon Laue analyzer with scintillation detectors as described by Kropf et al. [38]. For energy calibration, a silver or palladium foil spectrum was acquired through a third ion chamber simultaneously with each measurement. The samples were ground and packed into the sample holder. The amount of sample was chosen based on the sample loading to ensure appropriate total absorbance (25.51 keV for Ag edge and 24.35 keV for Pd edge). Samples were reduced in 3.5% H_2/He at 200 ºC, cooled in He and scanned at room temperature. Selected samples containing Pd were scanned in flowing 3.5%H_2/He to determine that no Pd hydride formed under the conditions of these experiments.

Ag K edge EXAFS was employed to estimate the particle sizes since the loading of Pd is very low and therefore the particle size can be estimated directly from the Ag coordination number. Pd K edge EXAFS was used to investigate the environment of Pd. The WINXAS 3.1

program was used to fit the data to obtain coordination number and bond distance between neighboring Ag atoms, using a k^2-weighted Fourier transform. The Ag-Ag phase and amplitude functions were obtained from the first coordination shell of Ag foil (N_{Ag-Ag} = 12 at 2.889 Å). An empirical relationship between the coordination number and particle size previously extracted from a series of platinum samples was used since both silver and platinum are fcc (face centered cubic) metals [39]. The following is the equation used to estimate mean particle sizes in angstroms

$$d = 10^{\,0.1319 \times CN + 0.4237}$$

However, since there is no specific rule to choose Debye-Waller factor, some error is introduced in the size estimation. Therefore, STEM results are needed to calibrate the relationship of particle size vs. coordination number. Average particle size is determined with an uncertainty of ±10% and the bond distance with ±0.02 Å [39].

1.2.2.2 Transmission Electron Microscopy

High Resolution TEM images were obtained at UIC's Research Resources Center facility using the JEM-3010 (a 300 keV transmission electron microscope with a LaB6 electron source). The JEM-3010 is an ultrahigh resolution analytical electron microscope with a point resolution of 0.17 nm. It is fitted with a Thermo Noran Vantage XEDS system with a light element X-ray detector, which is used for EDX. Samples were dispersed in water and sonicated for 20 min. A drop of the suspension was added dropwise to a holey-carbon grid. Images were taken in a bright field mode with an objective aperture selected to permit lattice imaging. A minimum of 100 particles were counted to get an accurate representation of the particle size distribution for each catalyst using Gatan Digital Micrograph software.

1.2.2.3 Scanning Transmission Electron Microscopy

STEM images were obtained at UIC's Research Resources Center facility using the JEOL-ARM 200CF aberration corrected microscope (70 pm spatial resolution and 300 meV energy resolution). Samples preparation is identical to that for TEM imaging. Images were taken using the High Angle Angular Dark Field (HAADF) mode with image contrast approximately proportional to Z^2. Images were analyzed using the Gatan Digital Micrograph software to determine the particle size and to provide a histogram of particle size distribution used to determine the dispersion of the dilute alloy catalysts. About 100 to 400 particles were counted to get an accurate representation of the particle size distribution for each catalyst.

1.2.3 Catalysis

Catalytic testing for gas phase acrolein hydrogenation was performed in a 1/2 inch OD stainless steel fixed-bed continuous flow reactor. Control of the reaction feed gases (H_2 and Ar) was done with flow controllers (Brooks® Models 5964, 5850EM). Acrolein (90%) and its three hydrogenation products, allyl alcohol, propionaldehyde and 1-propanol (Sigma Aldrich) were injected into the system using a liquid pump (VICI M6). Acrolein (boiling point = 73 °C) is evaporated in a heat tape traced (> 100°C) four way cross packed with quartz wool, and is carried into the system by reaction feed gases. Unless otherwise stated, the testing was done using a 20:1 molar ratio of H_2 to acrolein at 200 °C and 5 atm reaction conditions. The mass of the catalyst used for each test varied from 7-100 mg, depending on the activity of the catalyst. Before each run, the concentration of acrolein was checked via a reactor bypass line that connects directly to the gas chromatograph (GC). Catalyst samples were reduced *in situ* in 20% H_2/Ar flow at 200 °C for 20 min prior to testing to ensure the catalysts are in a fully reduced

metallic state. The reactor effluent was analyzed by an on-line gas chromatograph (Agilent 6890) equipped with a dual column formed by a RT-Msieve 5A and a RT-QPLOT (Restek) for lighter gaseous species and a EC-Wax (Alltech) for less volatile species such as alcohols. TCD (thermal conductive detector) and FID (flame ionization detector) are utilized for detecting H_2 and other organic/flammable compounds, respectively. The whole system was built with high-pressure-tolerant stainless steel parts and heat-traced to avoid condensation of any product. The diagram of the reaction system is illustrated in Figure 3.

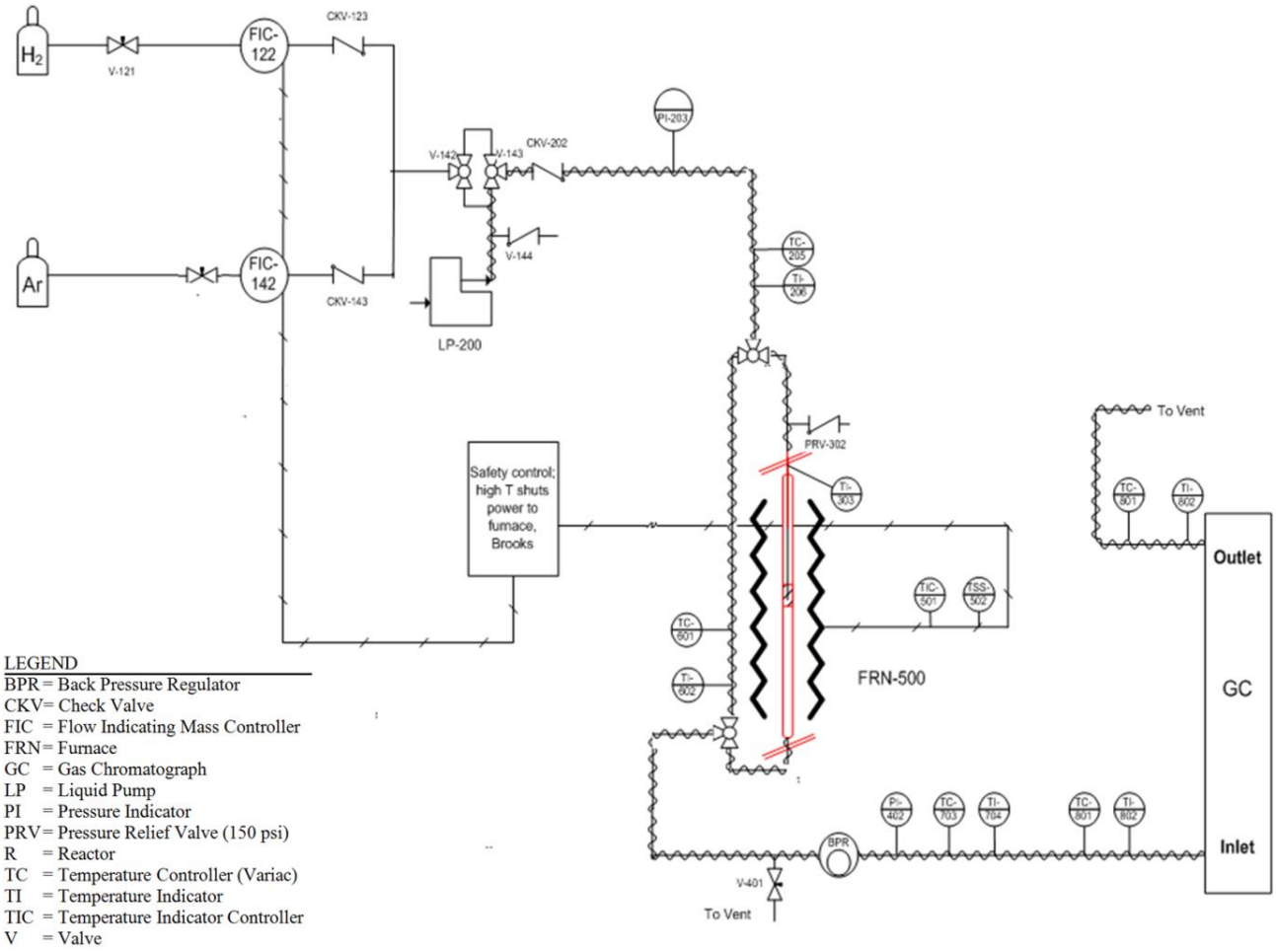

Figure 3. Schematic presentation of the plug flow reactor.

1.2.4 Kinetics Study

The kinetics study provides means of understanding the effect of different experimental conditions (physical state and concentration of the reactants, contact time, temperature and pressure) on the reaction mechanism. Reliability of the experimental data is imperative for accurate prediction of the kinetic equation. The plug flow reactor was operated isothermally with the reactants and diluent gas entering the reactor at temperature close to that of the catalyst bed. Thermocouples were placed in increments along the entire length of the reactor to look for the temperature gradients. The error associated with temperature measurements is considered to be within ± 0.1°C. Data was acquired while operating under steady state conditions; although the progression of the catalytic activity with time during the approach to steady state was recorded as well. To ensure that no mixing of fluid along the flow path is occurring, flow was checked in bypass mode and the GC product distribution was checked with theoretically predicted values (input values acquired from flow meters). The precision of GC is in the range of 0.05 to 0.1 %. Liquid pump (VICI M6) used to deliver acrolein into the feed operates with a volume precision and accuracy error of less than ± 0.5% at the desired flow rates.

For the experiments requiring low reactant flow rates or changes in ratio of the reactants, the contact time with catalyst bed was held constant by varying the concentration of the diluent gas in the stream. In addition, for any given type of experiment, the size of the catalyst bed was held constant for all the catalysts. Maintaining an appropriate size catalyst bed ensures good flow conditions hence preventing channeling. As the acrolein hydrogenation is highly exothermic process and as the catalysts tested vary in activities, different amounts of each catalyst were needed. The difference in mass was made up with a diluent (SiO_2). Test was performed to ensure that silica is an inert material for this reaction.

As the reaction is occurring on a solid-liquid interface, the heat and mass transfer (external and internal) to and from the interface needs to be faster than the catalytic reaction, so that the rate measured is the intrinsic rate of the reaction (kinetic controlled regime). The effect of the external heat and mass transfer is minimized by exposing the entire catalyst bed to the same concentration of the reactants by operating the reactor in the differential mode (low conversion) as oppose to integral mode (high conversion). This is necessary because in a plug flow reactor the rate is a function of position hence the rate may change as the concentration changes [40]. Therefore, if the conversion is high, then the reported rate is actually the result of the integrated rate as a function of reactor length, i.e. not single valued. Maintaining differential conversion allows us to assume a uniform concentration throughout the catalyst bed. Differential conversion is typically considered to be under 10%.

The effect of internal mass and heat transport of reactant molecules into the support pores or products to the surface of the particle can be characterized by the ratio of the effective reaction rate to the rate of the reaction in the kinetic region. If the isothermal operation is assumed, the effect can be approximated by the Thiele modulus. It is a theoretical measure of the mass transfer effect, a dimensionless variable $\Phi = \sqrt{kR^2/D}$ where k is the intrinsic rate constant, R is the characteristic diffusion length (i.e. the catalyst pellet radius) and D is the diffusion coefficient. If the value of the Thiele modulus $\Phi >> 1$ the reaction is in a mass transfer limited regime, while the kinetics-controlled regime is found in the limit of a low Thiele modulus ($\Phi << 1$). When the catalyst grain is reduced, the Thiele modulus decreases, as it is easier for the reactant molecules to travel in or out the pores. Reproducing the activity measurements in turn intrinsic reaction rate when testing the catalyst at varying grain sizes would indicate a kinetically control regime. This

test was performed by Wei et.al for 8%Ag.SiO_2 catalyst and it was shown that for these catalysts no internal mass transfer limit exists [12].

The catalyst's selectivity is the primary way of evaluating the catalyst's performance. Herein, the selectivity (%) defines the fraction of desired product in product stream and conversion (%) is the fraction of the reactant converted. Selectivity at a fixed conversion (10%) is chosen, to compare between the catalysts and establish correlations between the particle size/metal loading and the observed selectivities. In this way, a fair performance comparison of different catalysts can be conducted. Therefore, it is vital that the kinetics analysis is reproducible and accurate. The selectivities and activities measured must be shown to be consistent across multiple trials confirming that the data represents the steady state conditions. Significant amount of time was spent optimizing the reactor to ensure accurate and reproducible selectivity and activity measurements (< 4% error).

For the hydrogenation reactions performed in the flow reactors, the distribution of the unreacted product and reaction products will go through the initial transient state, the length of which depends on the space velocity of the reactant, the adsorption properties of the support and the catalyst stability [41, 42]. Evolution of the catalytic activity with time on stream, at a single flow rate, during the approach to steady state was recorded to understand the extent of deactivation that the catalyst undergoes and to ensure the steady state conversion required for the kinetics study. Figure 4 shows a dependence of product selectivities with time on stream for one of the Pd-Ag/SiO_2 catalysts examined. Almost identical transient behavior is observed for all samples tested, indicating a rapid deactivation process before the steady state is reached. Minimal changes in the selectivity of the catalyst are observed during the initial adjustment to catalytic operation. Once the steady state operation is reached, no deactivation is observed as a

response to changing operating conditions (10 hours is the maximum time on steam examined), implying that the reaction kinetics can be treated independently from the deactivation process.

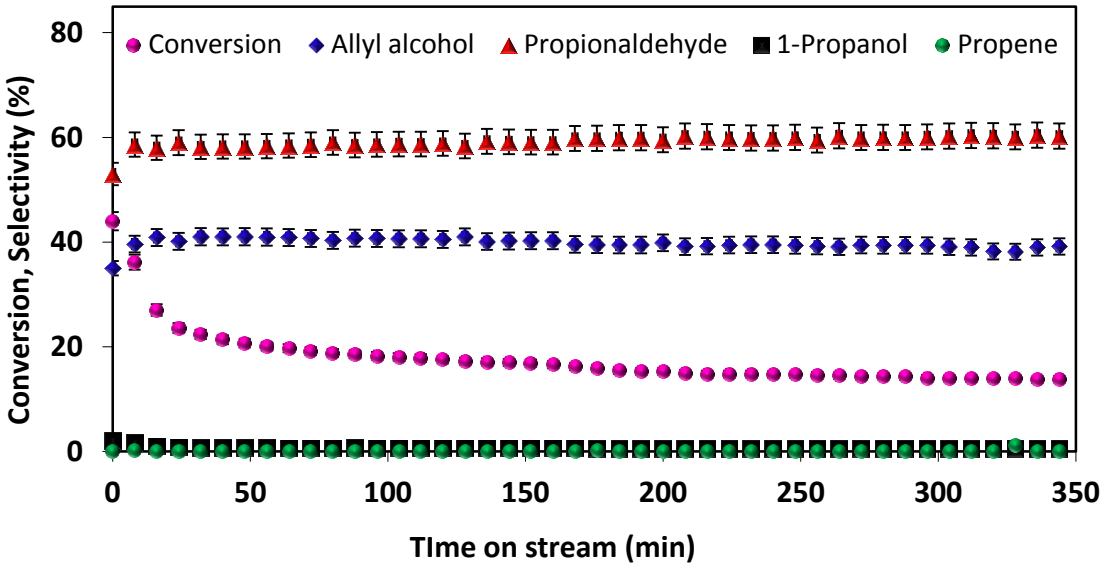

Figure 4. Dependence of product selectivities on the initial deactivation process over Pd-Ag/SiO_2 catalyst.

1.2.5 Rate Equation

Reaction kinetics is the study of rates of chemical process that provides means for construing the reaction mechanism. The ability to measure the intrinsic reaction rates is imperative for the determination of the kinetic equation and the values of its constants. Kinetic parameters, i.e. reaction rate (r), activation energy (Ea), reaction orders for acrolein (m) and hydrogen (n), rate constant (k) and pre-exponential factor (A) of the Arrhenius equation are acquired given the rate law equation

$$r = k\ [Acrolein]^m\ [H_2]^n$$

By varying the concentration of each reactant, m and n can be calculated. A linear relationship between ln(r) and ln[Acrolein] will evolve by taking the natural logarithm of the rate equation as following equation

$$ln(r) = ln(k) + m\ln[Acrolein] + n\ ln[H_2]$$

Since k is only a function of temperature here, at fixed T the slope from plotting ln(r) against ln[Acrolein] is m when keeping the concentration of H_2 constant. n can be determined in an analogous manner. At the same time, we can also calculate the reaction constant k. As a result, the pre-exponential factor A is determined by assuming an Arrhenius expression for the rate law

$$k = A\ e^{-E_a/(RT)}$$

Taking the natural logarithm yields

$$ln(k) = -\frac{E_a}{RT} + ln(A)$$

Plotting ln (k) against 1/T generates a straight line, with a slope of –Ea/R. Thus, the activation energy can be calculated.

1.2.6 Pathway Analysis

In a complex reaction network, determination of the reaction pathway is a challenging task. Pathway analysis will be performed by using the method developed by Bhore et al. [43] for discernment of the rank (*i.e.*, primary, secondary, etc.) of a reaction product. The first-rank delplot method, allows for separation of the primary products from nonprimary products by plotting the selectivities to various products as a function of conversion [43]. Extrapolating to 0% conversion we consider any product with non-zero selectivity at 0% conversion to be a primary product. A primary product is one that forms through one adsorption event. Secondary

rank products will have zero selectivity at 0% conversion, which means these products typically form when a primary product re-adsorbs to the surface. Performing a secondary pathway analysis is done by using the primary product(s) as reactants in the feed instead of acrolein. By repeating the delplot analysis, higher product ranks can be confirmed.

1.2.7 Reaction Mechanism

Every heterogeneous catalytic reaction proceeds via certain number of elementary reactions (only one energy barrier is overcome) [44]. The reaction mechanism is the set of elementary reactions that describes major characteristics of the process studied. As the reaction takes place at the surface of the catalyst, the rate expression should describe accurately the dependence of the surface concentrations on the bulk ones and the total effect of the adsorbed surface species. (i.e. Law of Surface Action). The Arrhenius equation is strictly valid only for elementary reactions. The equations are proposed on empirical basis or they may be derived based on some reaction mechanism.

Discriminating between possible mechanisms can be done by the reaction orders of hydrogen and acrolein. By writing rate laws assuming different rate limiting steps (adsorption of acrolein and/or hydrogen or the initial hydrogenation step) the possible reaction orders will be different. If the functional dependence of the acquired data is similar to the proposed rate expression, then the sequence of elementary steps is considered plausible, based on which it will be possible to further support the actual role of Pd.

1.2.8 Computational Methodology

Results are obtained with density functional theory (DFT) calculations implemented in Vienna *Ab initio* Simulation Package (VASP) [45, 46]. The kinetic energy cutoff for the plane wave basis set of 500 eV is employed. A Projector-augmented wave (PAW) based pseudopotential is utilized to calculate exchange and correlation energies [46, 47]. A five-layer slab model with 3 × 3 surface unit cell is adopted to represent the Ag(111) surface. The Brillouin zone is sampled using a 3 x 3 x 1 Monkhorst-Pack k-point grid with Methfessel-Paxton smearing of 0.2 eV [48]. The geometries of all structures were located with the conjugate gradient method and were considered to be converged with energy within 0.001 eV and forces of less than 0.025 eV/Å. The top three layers are allowed to relax. These nonspin-polarized calculations were run with 16 Å of vacuum space above all unit cells to ensure negligible interaction.

1.3 Results and Discussion

1.3.1 Catalyst Reactivity

A series of PdAg, PtAg, and IrAg alloy nanoparticle catalysts in varying Ag to alloying metal ratios (1000:1, 800:1, 500:1 and 200:1) as well as their monometallic counterparts were prepared on SiO_2 support. Notation for each sample includes weight percent of metal loading and particle size while the details of synthesis method, precursors and treatment steps for each sample are found in TABLE I. For example, 0.05%Pd + 10%Ag_7.9 nm is a sample with 0.05 weight percent of Pd and 10 weight percent of Ag supported on silica prepared by modified Strong Electrostatic Adsorption method, calcined at 550 °C for 3 hours, reduced at 325 °C for 2 hours and steamed at 500 °C for 2 hours.

Synthesis of catalysts of varying particles sizes and narrow particle size distribution within a sample, containing a well dispersed Pd (or Pt or Ir) in the Ag nanoparticle was desired. Thirty catalysts were made with different loading of the alloying metals (0.01%, 0.015%, 0.02% and 0.05%) doped in the silver (8%, 10%, 12% and 16%) on a SiO_2 support. Modified IWI was shown to provide the best Pd dispersion. In comparison, mSEA and CoIWI proved to be less predictable with respect to Pd dispersion. Particle sizes of approximately 2 nm were obtained for most catalysts by mIWI and mSEA. Subsequent steaming treatments were carried out at 350 or 550 °C for 2 hours to sinter the small particles, whereby particles of approximately 4 to 8 nm were formed by steaming at respective temperatures. Using CoIWI it was possible to dictate the desired particle size by increasing the metal loading. Subsequent calcination treatments made small particles (~2 nm) irrespective of metal loading. Calcination improved Pd dispersion, making it possible to increase the Pd loading without causing a rapid nucleation of Ag around Pd.

Particle sizes were determined via EXAFS spectrum and TEM/STEM imaging (selected samples), and the results are provided in TABLE II. The particle size obtained by fitting EXAFS coordination number is the mass averaged number, whereas TEM/STEM provides the mean particle size along with distribution range. Ag and Pd coordination numbers and bond distances to the nearest neighbors determined at the Pd K edge and Ag K edge are listed in TABLE II. The numbers for bulk metals were also given for comparison. The coordination numbers at the Ag K edge were used to estimate particle size. Correlating the Pd CN to the Ag CN will give additional insight into the structure of the Pd-Ag alloy, as a good approximation of the Pd dispersion can be determined (i.e. position of Pd in Ag nanoparticle). STEM images and corresponding particle

size distribution for few representative samples (10%Ag_1.2 nm, 0.01%Pd+10%Ag_2 nm, 0.05%Pd+10%Ag_2.5 nm and 0.05%Pd+10%Ag_5.1 nm catalysts) are shown in Figure 5.

TABLE I
CATALYST SYNTHESIS METHODS, PRECURSORS AND TREATMENT STEPS

Samples (SiO_2 support)	Synthesis Method	Precursors	Post Treatment Temperature (°C)		
			Calcination	Reduction	Steaming
0.01 %Pd	IWI	$Pd(NO_3)_2$	---	325	---
8 %Ag_8.0nm	IWI	$Ag(NO)_3$	---	325	---
8 %Ag_10.0nm	IWI	$Ag(NO)_3$	---	325	---
10 %Ag_1.2nm	IWI	$Ag(NO)_3$	---	325	---
0.01 %Pd + 8 %Ag_4.3 nm	CoIWI	$Ag(NO)_3$, $Pd(NO_3)_2$	---	325	---
0.015 %Pd + 12 %Ag_9.3 nm	CoIWI	$Ag(NO)_3$, $Pd(NO_3)_2$	---	325	---
0.015 %Pd + 12 %Ag_4.9 nm	CoIWI	$Ag(NO)_3$, $Pd(NO_3)_2$	400	325	---
0.02 %Pd + 16 %Ag_ 7.5 nm	CoIWI	$Ag(NO)_3$, $Pd(NO_3)_2$	---	325	---
0.02 %Pd + 16 %Ag_4.9 nm	CoIWI	$Ag(NO)_3$, $Pd(NO_3)_2$	400	325	---
0.01 %Pd + 10 %Ag_2.0 nm	mIWI	$Ag(NO)_3$, $Pd(NO_3)_2$	550	325	---
0.01 %Pd + 10 %Ag_4.1 nm	mIWI	$Ag(NO)_3$, $Pd(NO_3)_2$	550	325	350
0.01 %Pd + 10 %Ag_8.5 nm	mIWI	$Ag(NO)_3$, $Pd(NO_3)_2$	550	325	500
0.01 %Pd + 10 %Ag_4.8 nm	mSEA	$Ag(NO)_3$, $Pd(NO_3)_2$	550	325	350
0.01 %Pd + 10 %Ag_10.2 nm	mSEA	$Ag(NO)_3$, $Pd(NO_3)_2$	550	325	500
0.05 %Pd + 10 %Ag_2.5 nm	mIWI	$Ag(NO)_3$, $Pd(NO_3)_2$	550	325	---
0.05 %Pd + 10 %Ag_5.1 nm	mIWI	$Ag(NO)_3$, $Pd(NO_3)_2$	550	325	500
0.05 %Pd + 10 %Ag_3.8 nm	mSEA	$Ag(NO)_3$, $Pd(NO_3)_2$	550	325	---
0.05 %Pd + 10 %Ag_4.1 nm	mSEA	$Ag(NO)_3$, $Pd(NO_3)_2$	550	325	350
0.05 %Pd + 10 %Ag_7.9 nm	mSEA	$Ag(NO)_3$, $Pd(NO_3)_2$	550	325	500
0.01 %Pt + 10 %Ag_2.5 nm	mIWI	$Ag(NO)_3$, $[Pt(NH_3)_4](NO_3)_2$	550	340	---
0.01 %Pt + 8 %Ag_6.8 nm	CoIWI	$Ag(NO)_3$, $[Pt(NH_3)_4](NO_3)_2$	---	340	---
0.015 %Pt + 12 %Ag_5.7 nm	CoIWI	$Ag(NO)_3$, $[Pt(NH_3)_4](NO_3)_2$	---	340	---
0.02 %Pt + 16 %Ag_5.2 nm	CoIWI	$Ag(NO)_3$, $[Pt(NH_3)_4](NO_3)_2$	---	340	---
0.01 %Ir + 10 %Ag_6.6 nm	mIWI	$Ag(NO)_3$, $[Ir(NH_3)_5Cl]Cl_2$	550	340	---
0.01 %Ir + 8 %Ag_5.2 nm	CoIWI	$Ag(NO)_3$, $[Ir(NH_3)_5Cl]Cl_2$	---	340	---
0.015 %Ir + 12 %Ag_6.8 nm	CoIWI	$Ag(NO)_3$, $[Ir(NH_3)_5Cl]Cl_2$	---	340	---
0.02 %Ir + 16 %Ag_9.6 nm	CoIWI	$Ag(NO)_3$, $[Ir(NH_3)_5Cl]Cl_2$	---	340	---

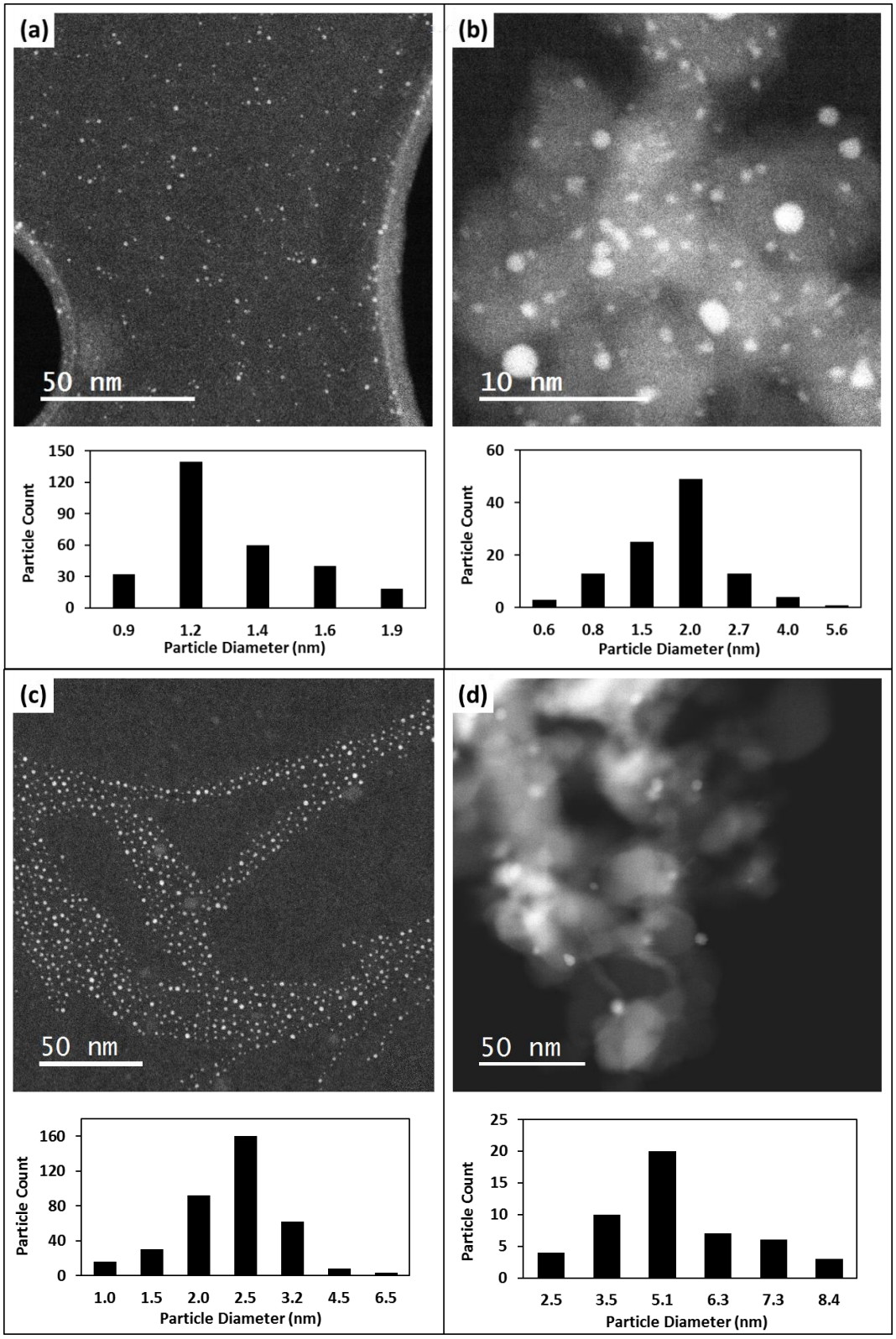

Figure 5. Representative aberration corrected HAADF-STEM images and particle size distribution histograms of the as-prepared (a) 10%Ag_1.2 nm, (b) 0.01%Pd + 10%Ag_2.0 nm, (c) 0.05%Pd + 10%Ag_2.5 nm samples and (d) 0.05%Pd + 10%Ag_5.1 nm.

The normalized EXAFS spectra and the Fourier transformation in R space of the data taken on 0.01%Pd+10%Ag_3.1 nm, 0.01%Pd+10%Ag_8.5 nm and 0.05%Pd+10%Ag_7.9 nm samples along with Ag Foil are shown in Figure 6. For the 0.01%Pd+10%Ag_8.5 nm sample, two peaks at 2.7 Å and 2.1 Å appear in the spectra with a shoulder at 1.9 Å. For the 0.01%Pd+10%Ag_3.1 nm sample, these peaks are shifted to slightly smaller scattering distances due to lattice contraction with decreasing particle size, i.e. changes in the hybridization of the Ag-Ag bonds as the coordination decreases [39]. It can also be seen that the bigger the particles are the sharper EXAFS oscillation is since Ag atoms have more neighboring atoms.

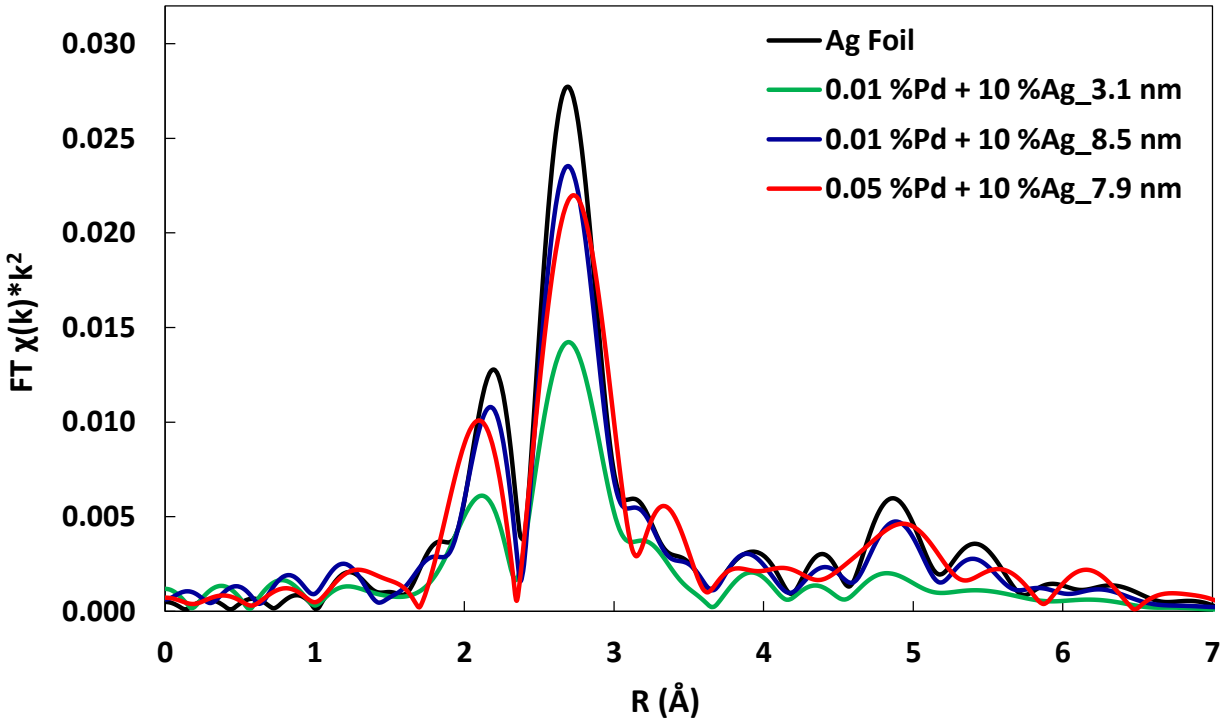

Figure 6. Fourier transform of the k^2-weighted Ag K edge data in R space ($\Delta k = 2.7 - 12.2$ Å−1) for Ag foil (black), 0.01% Pd + 10% Ag_3.1 nm (green), 0.01% Pd + 10 %Ag_8.5 nm (blue) and 0.05% Pd + 10% Ag_7.9 nm sample.

TABLE II
ESTIMATED PARTICLE SIZES AS DETERMINED FROM EXAFS AND TEM/STEM

Samples	Ag K Edge [a]		Pd K Edge [a]		Size [nm]	
	CN (±10%)	R [Å] (±0.02)	CN (±10%)	R [Å] (±0.02)	XAFS	STEM/ TEM
Ag bulk	12.0	2.89	-	-	10.2 ± 0.1	-
Pd bulk	-	-	12.0	2.74	-	-
8 %Ag_8.0 nm	10.8	2.89	-	-	7.1 ± 0.7	8.0 ± 1.2 [b]
8 %Ag_10.0 nm	-	-	-	-	-	10.0 ± 1.3 [b]
10 %Ag_1.2 nm	-	-	-	-	-	1.2 ± 0.3
0.01 %Pd + 8 %Ag_4.3 nm	9.9	2.87	10.6	2.82	5.4 ± 0.5	4.3 ± 1.4 [b]
0.015 %Pd + 12 %Ag_4.9 nm	9.6	2.87	9.2	2.84	4.9 ± 0.5	-
0.015 %Pd + 12 %Ag_9.3 nm	11.7	2.88	9.6	2.82	9.3 ± 0.9	3.5 ± 1.7 [b]
0.02 %Pd + 16 %Ag_4.9 nm	9.6	2.87	10.7	2.83	4.9 ± 0.5	2.4 ± 0.9 [b]
0.02 %Pd + 16 %Ag_7.5 nm	11.0	2.88	9.2	2.84	7.5 ± 0.8	-
0.01 %Pd + 10 %Ag_2.0 nm	8.1	2.87	9.7	2.79	3.1 ± 0.3	2.0 ± 0.9
0.01 %Pd + 10 %Ag_4.1 nm	9.0	2.87	8.3	2.84	4.1 ± 0.4	-
0.01 %Pd + 10 %Ag_8.5 nm	11.4	2.89	10.2	2.84	8.5 ± 0.9	-
0.01 %Pd + 10 %Ag_10.2 nm	12.0	2.89	9.8	2.84	10.2 ± 1.0	-
0.05 %Pd + 10 %Ag_2.5 nm	9.0	2.87	10.7	2.83	4.1 ± 0.4	2.5 ± 0.7
0.05 %Pd + 10 %Ag_5.1 nm	11.1	2.89	11.7	2.83	7.7 ± 0.8	5.1 ± 1.6
0.05 %Pd + 10 %Ag_4.1 nm	9.0	2.88	11.3	2.82	4.1 ± 0.4	-
0.05 %Pd + 10 %Ag_7.9 nm	10.8	2.89	11.1	2.84	7.1 ± 0.7	7.9 ± 1.4 [b]
0.01 %Pt + 8 %Ag_6.8 nm	10.7	2.87	-	-	6.8 ± 0.7	-
0.02 %Pt + 16 %Ag_5.2 nm	9.8	2.87	-	-	5.2 ± 0.5	-
0.01 %Ir + 8 %Ag_5.2 nm	9.8	2.88	-	-	5.2 ± 0.5	-
0.02 %Ir + 16 %Ag_9.6 nm	11.8	2.89	-	-	9.6 ± 1.0	-

[a] Ag and Pd coordination numbers (CN) and distances to neighbor atom (R) obtained from EXAFS.

[b] Particle size distribution histogram obtained from TEM images.

Figure 7 shows the X-ray adsorption near-edge structure (XANES) Ag K edge and Pd K edge spectra of the selected Pd-Ag samples and the reference spectra of corresponding foil (Ag and Pd) for the comparison. The shape characteristic peaks of Pd-Ag samples at 25.53 and 25.55 keV at Ag K-edge are identical to those of Ag foil (Figure 7a). Likewise, peaks at 24.37 and 24.39 keV at Pd K-edge of Pd-Ag samples are similar to those of Pd foil (Figure 7b), indicating that both Ag and Pd atoms are in the zero-valence state corresponding to metallic nanoparticles.

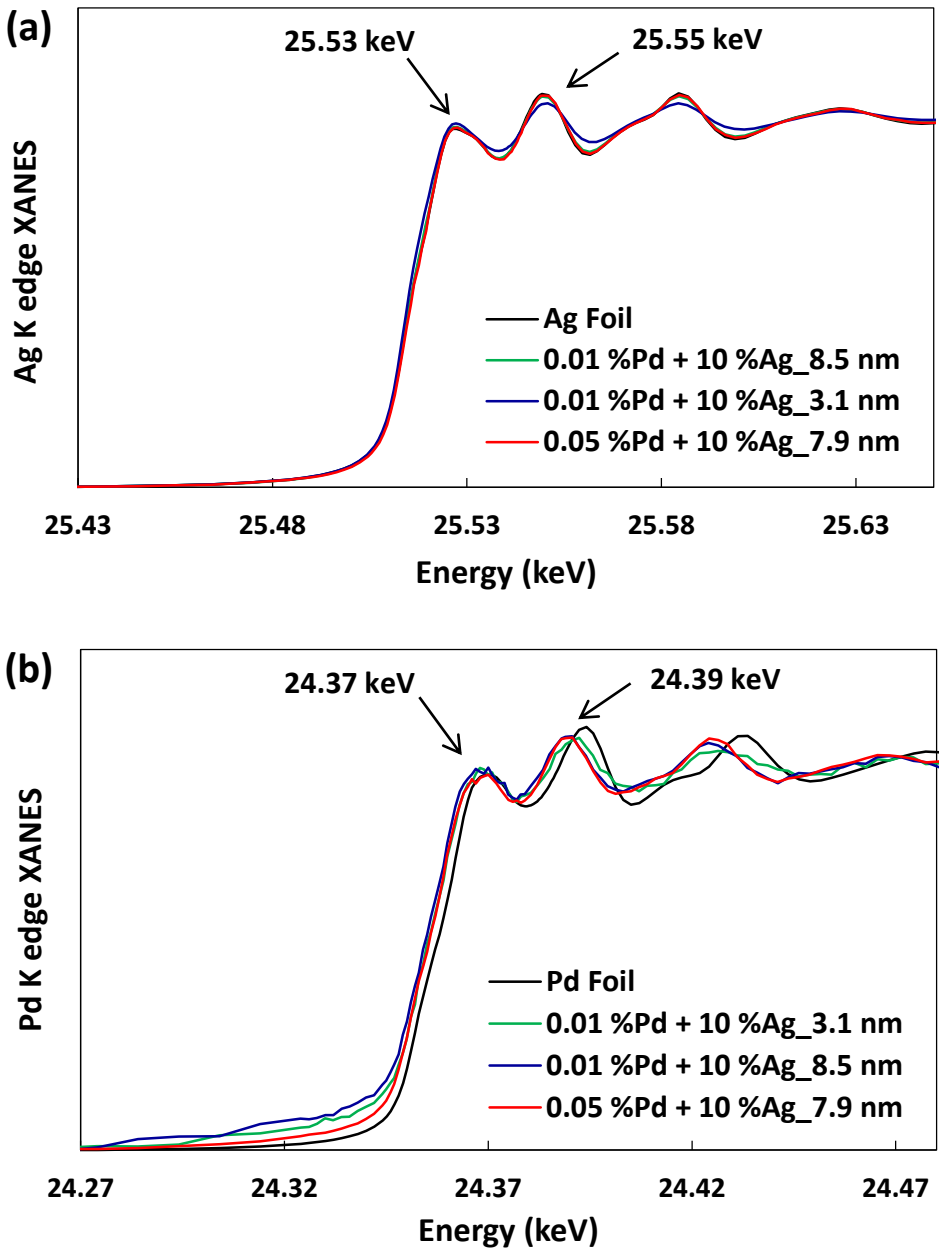

Figure 7. XANES spectra at (a) Ag K edge and (b) Pd K edge for Ag and Pd foil and representative Pd-Ag SAA samples.

TEM/STEM was used to help establish the relationship of coordination number and particle size, and to confirm the results from EXAFS. It can be seen in Figure 8 that EXAFS is an effective method for particle size determination as within the experimental error both

techniques provide consistent results. It should be pointed out that the estimated particle sizes predicted by EXAFS is the mass average (bulk technique) and higher values with respect to STEM (a local technique that examines the small area of the catalyst) implies the presence of some larger particles on the surface of the catalyst. This is especially prominent for samples with wider particle size distribution. For example, using STEM the 0.015 %Pd + 12 %Ag_9.3 nm was found to have an average particle size of 3.5 ± 1.7 nm while the size reported by EXAFS is 9.3 ± 0.9 nm. Therefore, for the samples characterized by EXAFS exclusively, the plot in Figure 8 could provide some additional information with respect to possible particle size distribution.

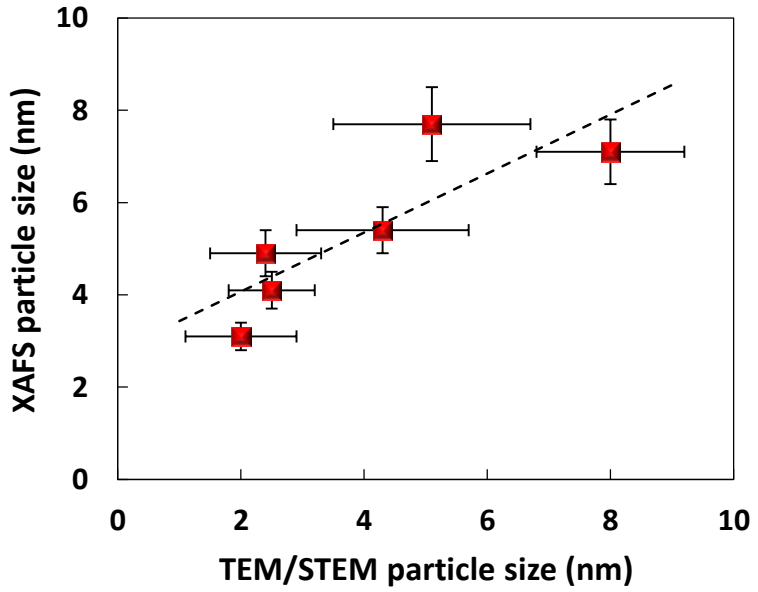

Figure 8. Correlation between the TEM/STEM and XAFS predicted particle sizes.

As will be seen, the selectivity and activity of Pd-Ag alloyed catalysts is strongly dependent on the size and dispersion of the Ag nanoparticle on the SiO_2 support, and on the weight percent and distribution of Pd metal within the Ag nanoparticle. A good approximation of the Pd dispersion can be achieved by analyzing the EXAFS K-edge as the samples with similar Pd and Ag CNs are assumed to have uniformly dispersed Pd atoms present both in the surface

and in the bulk. In addition, the bond distance of the Pd atoms to the nearest neighbors needs to be intermediate of the M-M bond distances in bulk silver (2.89 Å) and bulk palladium (2.74 Å) to imply that Pd is alloyed with silver atoms. For example, for 0.01%Pd+10%Ag_4.1 nm sample Ag and Pd CNs are similar (9.0 and 8.3) and the Pd-M bond distance (2.84 Å) is in the intermediate range. As such, catalysts exhibiting these characteristics are assumed to be Pd-Ag alloys formed in a way that silver serves as the host metal while isolated single Pd atoms are uniformly atomically dispersed, producing a nanoparticle analogs to the single crystal models of single atom alloy (SAA) catalysts described by Kyriakou et al. [28].

TABLE III
PRODUCT DISTRIBUTION ON Pd-Ag ALLOYS AND PURE Ag CATALYSTS[a]

Samples	Selectivity (± 4%)			
	Allyl Alcohol	Propionaldehyde	1-Propanol	Propene
8 %Ag_8.0 nm	35	64	0.8	0.1
8 %Ag_10.0 nm	39	60	0.6	0.4
10 %Ag_1.2 nm	38	61	0.6	0.4
0.01 %Pd + 8 %Ag_4.3 nm	34	65	0.6	0.1
0.015 %Pd + 12 %Ag_9.3 nm	4	96	0.2	0.1
0.015 %Pd + 12 %Ag_4.9 nm	29	71	0.5	0.1
0.02 %Pd + 16 %Ag_7.5 nm	4	96	0.3	0.3
0.02 %Pd + 16 %Ag_4.9 nm	28	71	0.6	0.2
0.01 %Pd + 10 %Ag_2.0 nm	38	61	0.5	0.1
0.01 %Pd + 10 %Ag_3.1 nm	30	68	1.5	0.3
0.01 %Pd + 10 %Ag_4.1 nm	30	69	0.5	0.2
0.01 %Pd + 10 %Ag_8.5 nm	38	62	0.4	0.1
0.01 %Pd + 10 %Ag_10.2 nm	10	88	1.1	0.4
0.05 %Pd + 10 %Ag_2.5 nm	14	86	0.3	0.1
0.05 %Pd + 10 %Ag_5.1 nm	13	86	0.5	0.2
0.05 %Pd + 10 %Ag_4.1 nm	5	94	0.3	0.1
0.05 %Pd + 10 %Ag_7.9 nm	21	78	0.6	0.2
0.01 %Pt + 8 %Ag_6.8 nm	33	66	0.6	0.1
0.02 %Pt + 16 %Ag_5.2 nm	28	71	0.6	0.2
0.01 %Ir + 8 %Ag_5.2 nm	36	63	0.6	0.1
0.02 %Ir + 16 %Ag_9.6 nm	27	71	1.2	0.3

[a] Data obtained at 200 °C, 5 atm and 10% conversion.

To determine and compare the catalysts performance for the selective hydrogenation of acrolein, the catalytic reactivity of the synthesized catalysts was tested at a constant reaction conditions (10% conversion, 200°C and 5 atm). Selectivity results to allyl alcohol (desired product) and side products (propionaldehyde, 1-propanol and propene) for all the catalysts are found in TABLE III. The selectivity to allyl alcohol on 8%Ag_8 nm and 0.1%Pd+8%Ag_4.3 nm samples (35 and 34%, respectively) are in accord with the previously reported data on the same catalysts [12, 32] which confirms the applicability of their trends to the results obtained in this study.

For Pd-Ag SAAs, the selectivity as a function of particle size is shown in Figure 9. The weight percent of Ag is kept constant (10 %) to extract information with respect to an increase in amount of Pd metal (0.01 and 0.05 wt%). 0.01%Pd-Ag SAA catalysts exhibit higher selectivity than 0.05%Pd-Ag SAAs. There appears to be a strong trend in selectivity, for all Pd loadings, with respect to particle size. For the samples with same Pd loading, selectivities remain consistent (< 10% variation) across the particle range examined, with a minimum in selectivity on the 4 nm particles. For 10 wt% Ag supported on SiO_2, 0.01 wt% of Pd provides the optimal selectivity, as an increase of only up to 0.05 wt%, even for a well dispersed particle, results in a significant loss of selectivity.

Of further note is the 38% selectivity for the 10%Ag_1.2 sample which is significantly higher, as shown in Figure 2, from the observations by Wei et al. [12]. An extensive examination of the catalyst surface was done via STEM, as EXAFS was not obtained. Figure 5a is a representation of the surfaces found by scanning multiple sections. The particle size was determined by counting more than 300 particles. It is however possible that the degree of uniformity of the particles may vary on the areas of the support not examined and as such could

be dominating the observed selectivity. Similarly high selectivities (28.7% at 1 bar and 39% at 10 bar at 250 °C) were found by Bron et al. [49] on the 7.5%Ag/SiO_2 catalyst with an average particle size of 2.5 nm. It was said that some uncertainty was associated with the particle size effect, as the TEM images also revealed the presence of a very small amount of larger particles on the surface [49]. As such, certain level of caution is given to particle size effect of this sample in the forthcoming discussion.

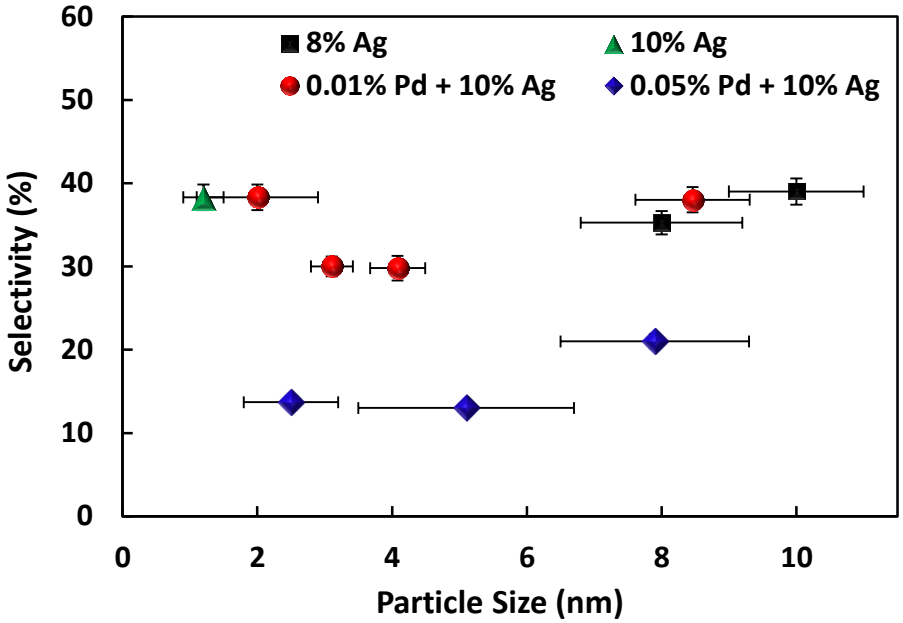

Figure 9. Comparison of selectivities toward allyl alcohol of Pd-Ag alloys and pure Ag catalysts with various particle sizes at 200 °C, 5 atm and 10% conversion.

The activity of the Pd-Ag SAA catalysts is of distinct interest, due to the inherently different reactiviaties of Pd and Ag monometallic catalysts for the hydrogenation of α, β - unsaturated aldehydes [10-12]. The reaction rates are expressed as the concentration of reactant (acrolein) consumed per mass of metal (Ag or Pd) in the catalyst, and is analyzed as a function of particle size (Figure 10a). For the samples with constant weight percent of Pd, an increase in particle size will decrease the reaction rate of the catalysts.

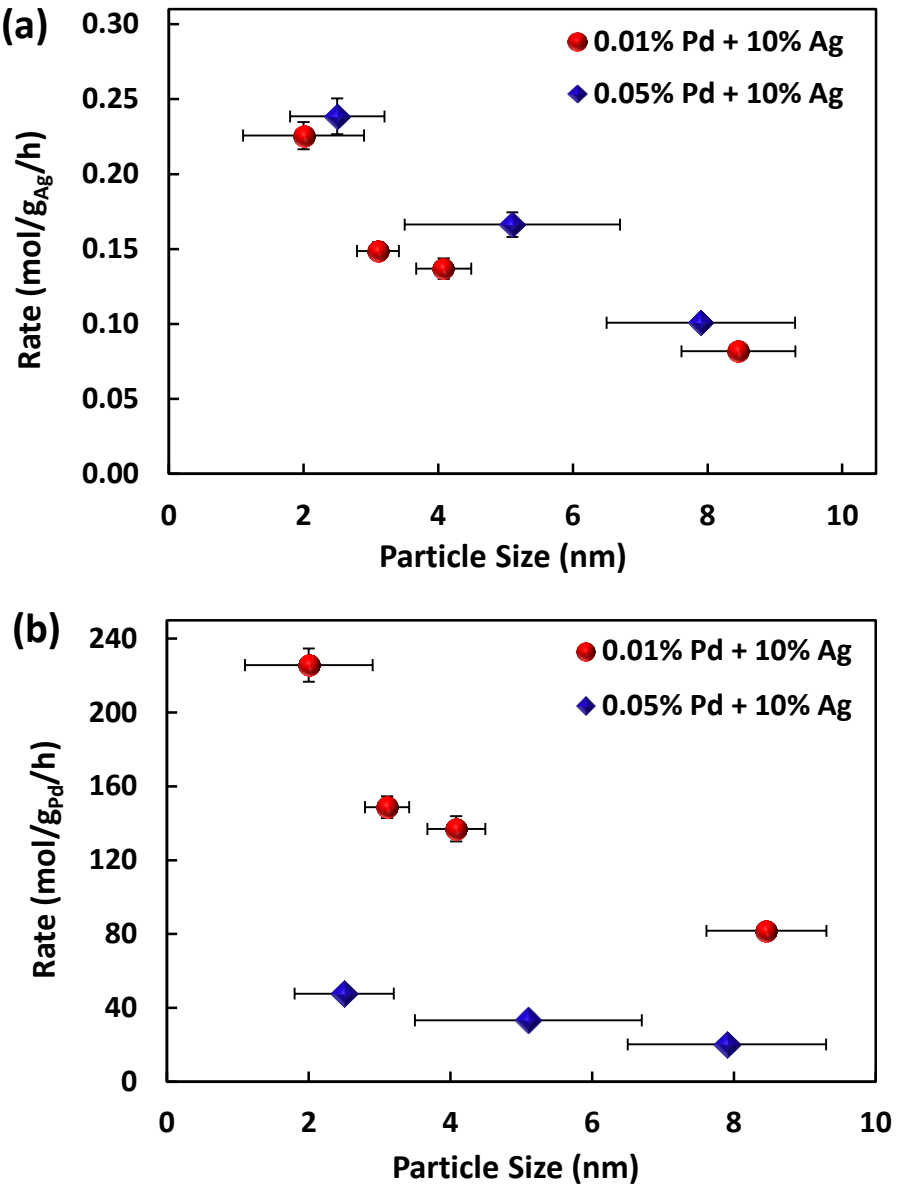

Figure 10. Rate calculated per mass of (a) Ag and (b)Pd in the catalyst vs. particle size for Pd-Ag alloys and pure Ag catalysts at 200 °C, 5 atm and 10% conversion.

However, at similar sizes the activities of 0.01% Pd-Ag SAAs and 0.05% Pd-Ag SAAs are almost identical. It appears that the rate of the well-dispersed Pd-Ag SAA is structure sensitive; i.e. reactivity is a function of particle size, with minimal dependence on the amount of Pd. This is very surprising, as monometallic Pd catalysts are too active for hydrogenation of acrolein [50]. If the rate calculated per mass of Pd in the catalyst is examined as a function of

size (Figure 10b) it can be seen that the dependence scales according, to the mass of Pd. That is, if the total effect of 0.01 and 0.05% Pd is the same, then the smaller amount of Pd in 0.01% Pd-Ag SAA samples would have a larger contribution to the rate of the reaction and correspondingly smaller effect per mass of Pd in 0.05% Pd-Ag SAA samples. The plot also shows, that with an increase in particle size the rates of both 0.01%Pd-Ag SAAs and 0.05%Pd-Ag SAAs decrease and approach the same value. This correlates to the decrease in the fraction of Pd atoms with respect to Ag, and in turn, a smaller contribution of Pd to the observed reaction rate.

If the reaction rate is normalized by the available surface sites, then the activity of the catalyst is expressed as the intrinsic rate at which a catalytic cycle turns over on an active site, i.e. turnover frequency (TOF). TOF based on surface sites is an average value of the catalytic activity or more specifically a lower bound to the true activity as only a fraction of the total number of surface atoms may be contributing to the reaction rate (Figure 11). Therefore, the TOF is estimated based on a hemispherical model for particle size whereby only surface atoms are considered. The number of surface atoms is given by the following equation, in which R is the radius of the silver particle and d represents the diameter of Ag atom (0.289 nm in bulk).

$$Number\ of\ active\ sites = \frac{4\pi R^2}{\sqrt{3}d^2}$$

Figure 11 reveals that the activity of Pd-Ag SAAs at constant Pd loading remains almost the same, within the particle size range examined. This is significantly different from TOFs on monometallic Ag/SiO_2 catalyst, where the activity tripled (from 0.006 to 0.026 s^{-1}) within same particle size range [12]. In addition, as with reaction rates, the activity of the catalysts exhibits much stronger dependence to particle size than the amount of Pd loading, as at any particle size only a small increase in TOF is observed for 0.05% Pd-Ag SAAs.

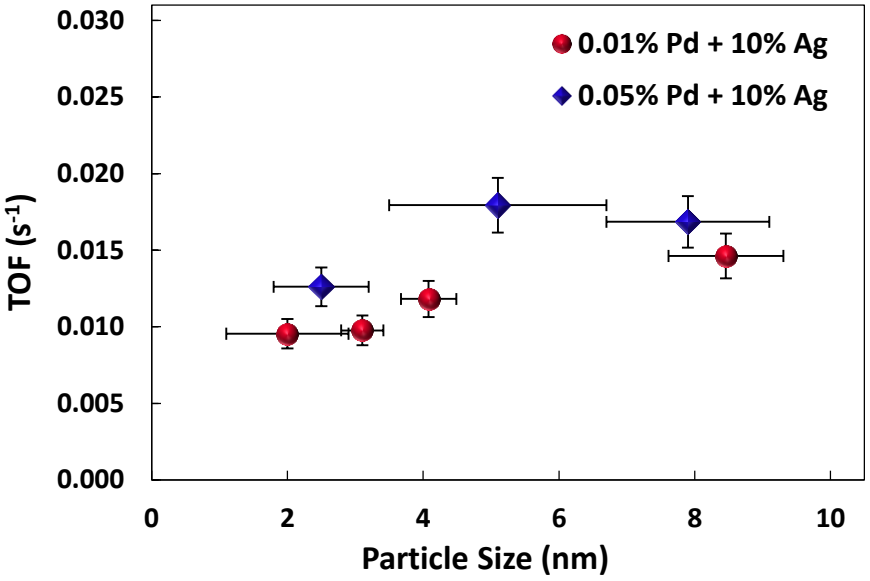

Figure 11. TOF vs. particle size for Pd-Ag alloys and pure Ag catalysts at 200 °C, 5 atm and 10% conversion.

By varying the synthesis method or post-treatments, metal loading can be increased while maintaining the catalyst dispersion. Three catalysts with different amounts of metal, at constant Ag to Pd ratio (800:1) were synthesized, obtaiing ~5 nm particles (Figure 12). Results show that an increase in the metal loading does not have a pronounced effect on the selectivity of the catalyst. A more evident change (from 34 to 29%) appears from 0.01%Pd+8%Ag_4.3 nm to 0.015%Pd+12%Ag_4.9 nm sample, with selectivity decreasing to 28% on 0.02%Pd+16%Ag_4.9 nm catalyst. The observed change could howerver be contributed to the preparation method of the catalysts, as 0.015%Pd+12%Ag_4.9 nm and 0.02%Pd+16%Ag_4.9 nm samples were calcined prior to reduction whereas for 0.01%Pd+8%Ag_4.3 nm the calcination step was omitted. TOF remains the same within experimental error (0.021 to 0.026 s^{-1}). However, the rate expressed per mass of Ag in the catalyst increases from 0.23 mol/g_{Ag}/h on 0.01%Pd+8%Ag_4.3 nm sample to 0.42 mol/g_{Ag}/h on 0.02%Pd+16%Ag_4.9 nm sample. It is evident, that doubling

the metal loading doubles the rate, indicing that the activity of the catalyst goes up, but the rate per site (TOF) does not change.

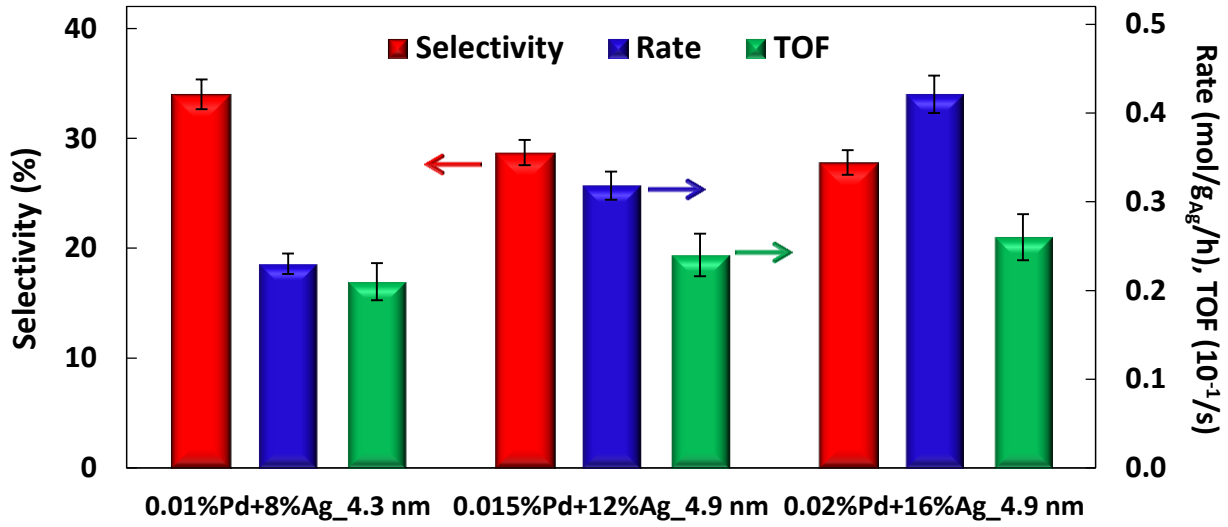

Figure 12. Comparison of the selectiviy, rate and TOF for samples with varying amounts of metal loading at constant particle size and Ag to Pd ratio (800:1) at 200 °C, 5 atm at 10% conversion.

Pd-Ag SAA catalysts were shown to combine the best attributes of both metals, exhibiting low H_2 dissociation barrier as Pd and low hydrogen adsorption enthalpy as Ag [32]. As such, a surface is created that can catalyze hydrogen dissociation and subsequent hydrogen atom spillover from Pd sites to the Ag surfaces [28, 32]. To determine that, in fact, the only role of the Pd is to dissociate hydrogen, further insight as to the active sites is required. Due to the highly dilute nature of these alloys with respect to the amount Pd, it has proved difficult to characterize the immediate surrounding of surface Pd, i.e. to determine Pd neighbors. As such, a different approach was applied to determine if the reaction is catalyzed by Pd, the minority active component, or if Ag is the only catalytically active species.

The catalytic performance of Pt and Ir alloyed Ag/SiO_2 catalyst (800:1 Ag to alloying metal ratio) was compared to the corresponding similar size Pd-Ag SAA (Figure 13) to observe

if alloys with other hydrogen active metals would behave in a similar fashion. Exchange of Pd in Pd-Ag SAA with Pt or Ir produces no change to the selectivity (~34%) and to the rate of the catalyst (~0.24 mol/g_{Ag}/h). The only observable change is to the TOF, which for 0.01%Pt+8%Ag_6.8 nm catalyst (~0.04 s^{-1}) is double that of 0.01%Pd+8%Ag_4.3 nm and 0.01%Ir+8%Ag_5.2 nm both of which exhibit similar activity (~0.02 s^{-1}). Activity of the Pd-Ag SAA is expected to be higher than that of Ir-Ag SAA, as the value observed herein is a consequence of the smaller particle size of the Pd-Ag SAA with respect to other samples.

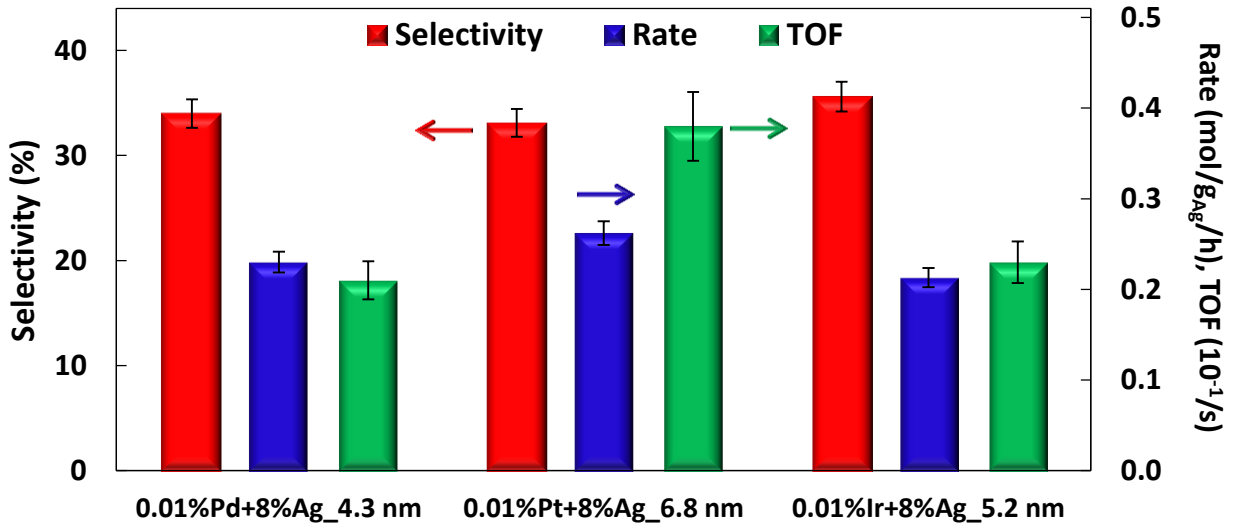

Figure 13. Comparison of the selectivity, rate and TOF for Pd, Pt and Ir alloyed Ag/SiO_2 catalysts at 200 °C, 5 atm at 10% conversion.

To understand why the change of alloying metal is not affecting the selectivity of the Ag alloyed nanoparticle we will address an assumption made with the respect to the formation of a SAA catalyst. Atomic radii of Pd, Pt and Ir are very similar, and the bulk M-M bond lengths (2.74, 2.77 and 2.72 Å for Pd, Pt and Ir, respectively) are similar to that of Ag. From the Ag K edge data (TABLE II) it can be seen that the Ag bond lengths are similar for all alloys (~2.88 Å) and close to that of Ag bulk (2.89 Å). As Pd, Pt or Ir are said to be atomically dispersed

throughout the Ag particle no strain effect should be produce due to alloying. However, identical selectivity of the catalysts does not necessarily mean that Pd is not a part of the active site, just that if it is catalytically active its role is such that both Ir and Pt would have the same effect.

Similar to Pd, hydrogen dissociation on Pt and Ir is facile with no activation barrier. On Pt/Ag(111) surface, hydrogen adsorption on Pt containing active sites is also decreased. In contrast, Ir sites on Ag(111) surface show a significantly higher hydrogen binding (TABLE IV). This would indicate that even though H_2 dissociation is barrierless, the spillover of hydrogen atoms from Ir containing site to Ag surface might be suppressed due to stronger adsorption, providing, in turn, less available hydrogen to be consumed in subsequent hydrogenation reaction. This correlates to the lower TOFs for Ir-Ag samples. For acrolein adsorption, all alloyed surfaces show almost identical, preferential acrolein adsorption via C=C bond with weaker acrolein binding energy on Pt containing Ag(111) active sites. This combined with the DFT predicts barrierless H_2 dissociation and decreased hydrogen binding energy on Pt/Ag(111) surface may account for the higher TOF for Pt-Ag catalysts.

TABLE IV

DFT CALCULATED ADSORPTION ENERGIES AND ACTIVATION BARRIERS

SAA Surfaces	E_{ads} [eV] of acrolein		H_2 dissociation	
	C=C bound	C=O bound	E_{ads} [eV]	E_{act} [eV]
Ag(111) [a]	-0.05	-0.03	0.63	1.15
Pd(111) [a]	-2.15	-0.85	-1.23	0
Pd/Ag(111) [a]	-1.36	-0.87	-0.33	0.31
Pt/Ag(111)	-0.59	-0.02	-0.54	0
Ir/Ag(111)	-1.39	-0.60	-1.03	0

[a] Values obtained from Aich et al. [32].

As a means of correlating the observed performance of the catalysts to the formation of Pd-Ag alloys, a control experiment was performed in which a physical mixture of two independently synthesized catalysts was tested (200°C and 5 atm at 10% conversion). Equal amounts of 0.01% Pd and 8% Ag_8 nm catalysts were mixed together and tested for allyl alcohol selectivity. In addition, 0.01%Pd sample was tested independently. As expected, Pd is extremely active, but not at all selective to allyl alcohol resulting in 97% selectivity to propionaldehyde, 3% to 1-propanol and with traces of propene (> 0.1%). Similarly, the physical mixture exhibited no selectivity to allyl alcohol. By comparing the reaction rates (calculated per mass of catalyst), the rate of the physical mixture (2.52 mol/g_{metal}/h) increases by an order of magnitude from monometallic Ag (0.17 mol/g_{metal}/h for 8%Ag_8 nm), decreases by three orders of the magnitude from the monometallic Pd sample (3.63 x 10^3 mol/g_{metal}/h for 0.01%Pd). It is evident that the presence of monometallic Pd is dominating the performance of the physical mixture, as such the herein observed results can be attributed to the formation of the Pd-Ag alloy.

In addition, we propose that the selectivity and activity of the Pd-Ag catalysts (TABLE III) is highly sensitive to dispersion [51]. Four samples (0.015%Pd + 12%Ag_9.3 nm, 0.02%Pd + 16%Ag_7.5 nm, 0.01%Pd + 10%Ag_10.2 nm and 0.05%Pd + 10%Ag_4.1 nm) exhibited poor catalytic performance with selectivities below 10%. If the Ag and Pd CNs of each sample are compared, difference in CN magnitudes varying in the range of 1.8 to 2.3 (TABLE II) are found. This indicates poor Pd dispersion within the Ag nanoparticle. For 0.015%Pd + 12%Ag_9.3 nm, 0.02%Pd + 16%Ag_7.5 nm and 0.01%Pd + 10%Ag_10.2 nm samples the Ag CN is higher than Pd CN. For example, in the case of 0.015%Pd + 12%Ag_9.3 nm sample, Pd CN is 11.7 and Ag CN is 9.0. Pd CN close to 12 indicates that Pd atoms are mostly in the bulk, i.e. completely coordinated in fcc environment. In contrast, for 0.05%Pd + 10%Ag_4.1 nm sample, Pd CN is

smaller (9.0) than Ag CN (11.3) showing that the Pd is under-coordinated relative to Ag. In this case, poor catalyst performance is due to segregation of Pd atoms to the surface of Ag nanoparticle.

The drop in selectivity for Pd alloyed Ag/SiO_2 catalysts with higher Pd loading (0.05%) was hypothesized to be caused by the presence of contiguous Pd atoms resulting in an unfavorable bonding configuration for acrolein [32]. This could account for the drop in the selectivity of our 0.05%Pd-Ag SAAs with the exception that the extent of loss is significantly smaller than predicted by Aich et al. [32]. Conversely, irrespective of the Pd loading, the dispersion seems to be critical to the catalyst performance affecting not only selectivity, but also significantly increasing the activity. Reaction rates that are 2 to 3 times higher than expected are observed (for example, 0.633 mol/g_{Ag}/h reaction rate on 0.02%Pd + 16%Ag_7.5 nm catalyst). Therefore, the presence of contiguous Pd atoms produces a catalyst exhibiting the properties of the typical hydrogenation catalysts that are very active but not selective to allyl alcohol.

1.3.2 Reaction Pathway

We have further extended our study of gas phase acrolein hydrogenation over Pd-Ag SAA by performing a pathway analysis for 0.01%Pd+10%Ag_2.0 nm sample. Results are correlated to the reaction pathway on $8\%Ag/SiO_2$ catalyst previously determined by Wei et al. [32]. Discrimination of the product rank (i.e. primary, secondary and higher rank products) was done by the delplot technique [43]. The reaction pathway is expected to remain the same for all 0.01%Pd-Ag alloys, whereas at high Pd content, one must recognize that this might not be the case (the primary pathways on monometallic Pd are certainly different from monometallic Ag). It should be noted, additional tests of the support material (SiO_2) in the absence of the catalyst

showed no activity and that water, the other likely product from the hydrodeoxygenation reaction, was not analyzed.

Figure 14 is the delplot for the primary and secondary product determination. The first rank delplot (Figure 14a) shows the selectivity dependence of all four products on conversion. Selectivity to allyl alcohol (~ 38%) and propionaldehyde (~ 60%) is steady from 10 to ~80% conversion. Selectivity to propene is very low (<1% at 100% conversion) and for 1-propanol it is only about 2% at 40% conversion. At very high conversion (~ 98%), an increase in 1-propanol selectivity (11%) is substantial enough to be correlated to the observed decrease to allyl alcohol (33%) and propionaldehyde (55%) selectivity. In Figure 14b, the fitting curves for propionaldehyde and allyl alcohol diverge at zero conversion, which confirms that these species are primary products. The intercept of 1-propanol is zero, implying it is a secondary product, while propene may be a second rank product due to its zero intercept or possibly even a higher rank product as its selectivity is too low to make an accurate evaluation (smaller than the experimental error).

Secondary pathway analysis was performed to confirm the product rank of propene and to determine if the observed selectivity of any of the first ranked products is partially due to two adsorption events, such as isomerization of allyl alcohol to propionaldehyde, or vice versa. Figure 15 shows the secondary pathway analysis using the primary products allyl alcohol and propionaldehyde as reactants in the feed instead of acrolein. When allyl alcohol is used as the feed, three products are observed (propionaldehyde, 1-propanol and propene). The fitting curve in Figure 15b diverges at zero conversion for all three products. This shows that all products are formed through one adsorption event directly from allyl alcohol. Using propionaldehyde as the

feed produces only 1-propanol, implying that once propionaldehyde is formed isomerization to allyl alcohol does not occur (Figure 15c).

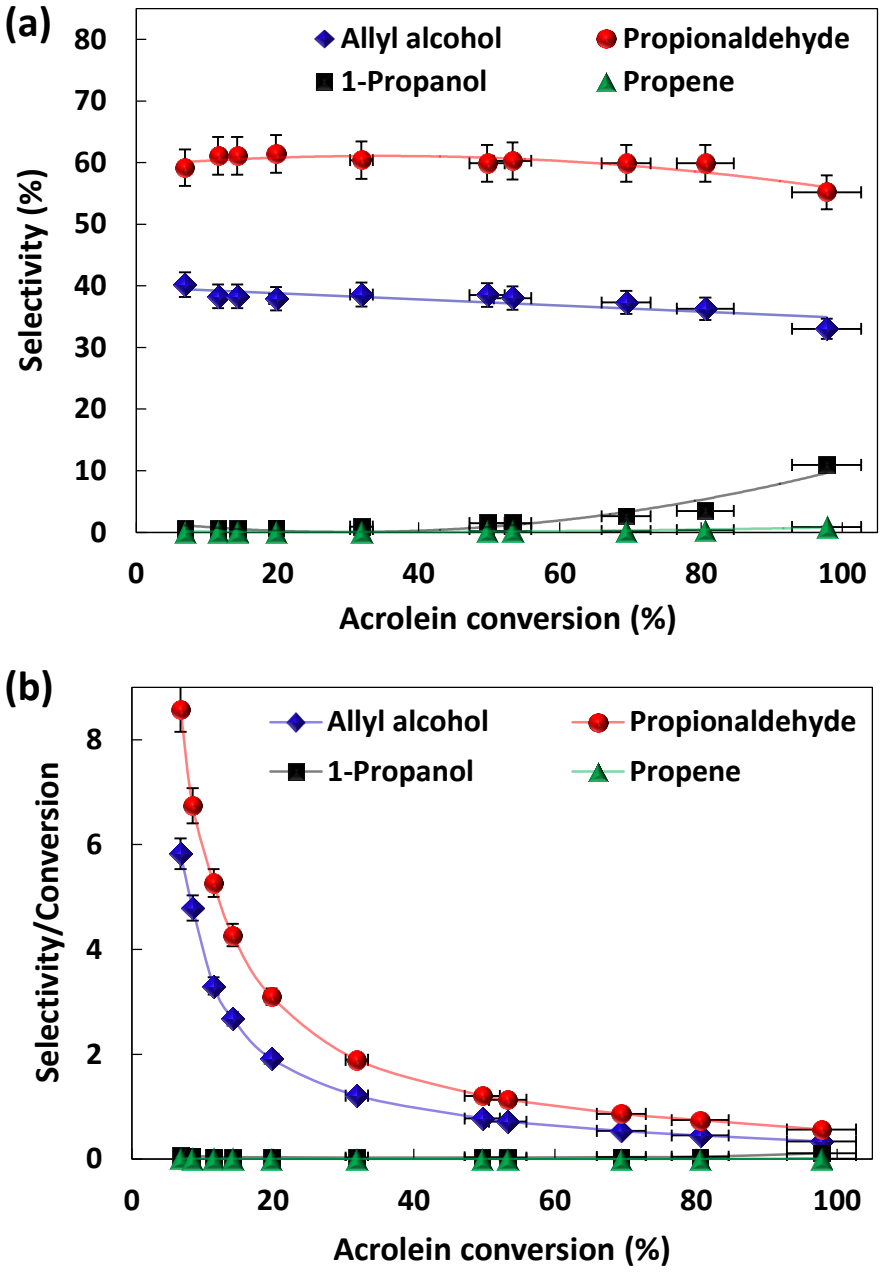

Figure 14. Primary pathway analysis (a) First-rank and (b) Second-rank delplot of 0.01%Pd+10%Ag_2.0 nm catalyst.

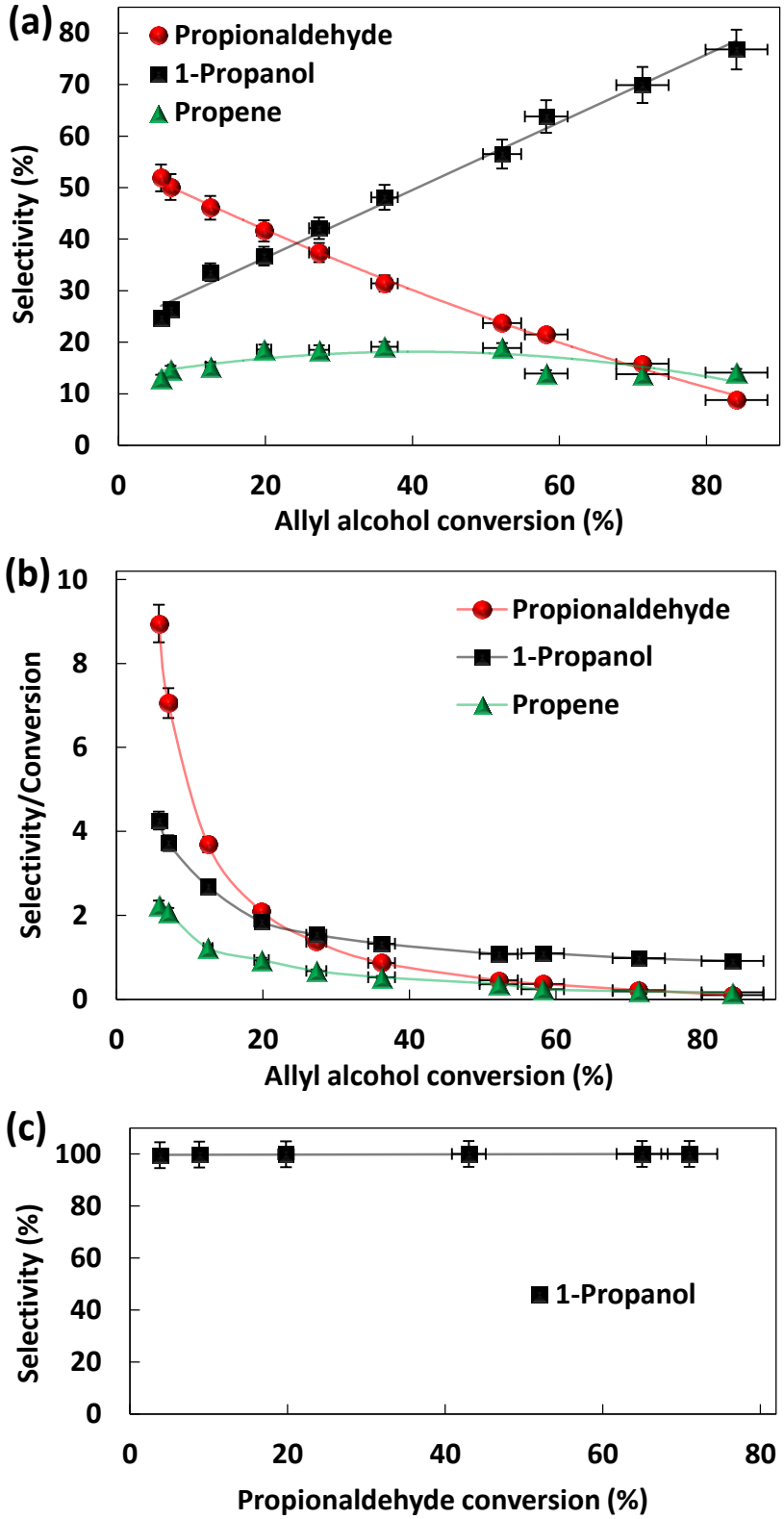

Figure 15. Secondary pathway analysis for 0.01%Pd+10%Ag_2.0 nm catalyst from allyl alcohol (a) First-ranked delplot and (b) Second-ranked delplot, and from propionaldehyde (c) First-ranked delplot

Unlike propionaldehyde, when allyl alcohol is used as a feed, the product distribution varies with conversion. At low conversion, allyl alcohol is isomerized to propionaldehyde. With an increase in conversion, selectivity to propionaldehyde decreases, and at 100% conversion, isomerization of allyl alcohol to propionaldehyde is eliminated with allyl alcohol preferentially hydrogenating to fully saturated alcohol (1-propanol). Therefore, secondary pathway analysis suggests that propene is a second-rank product produced from hydrodeoxygenation of allyl alcohol, 1-propanol is a secondary product produced from hydrogenation of both allyl alcohol and propionaldehyde, and at lower conversions propionaldehyde may be produced not only from hydrogenation of acrolein but also from the isomerization of allyl alcohol.

From the pathway analysis on Ag/SiO_2 it was shown that the reaction needs to be run at low conversion to achieve high selectivity to allyl alcohol, with the isomerization of allyl alcohol to propionaldehyde present for all conversions [12]. In contrast, on Pd-Ag SAA catalyst under high conversion conditions, isomerization reaction is inhibited. However, it is shown that even under high conversion it is not possible to improve upon the selectivity of the best Ag/SiO_2 catalyst as allyl alcohol still subsequently converts; only in this case it is fully hydrogenated to 1-propanol.

1.3.3 Reaction Kinetics

The study is further extended by performing a more in-depth analysis of the kinetics on the catalysts shown to have a very narrow particle size distribution and well dispersed Pd (10%Ag_2.0 nm, 0.01%Pd+10%Ag_2.0 nm, 0.01%Pd+10%Ag_8.0 nm, 0.05%Pd+10%Ag_2.0 nm and 0.05%Pd + 10%Ag_8.0 nm). As such, further elucidation of alloying and geometric effects should be achieved. A simple power rate law $r = k\,[\text{Acrolein}]^m\,[H_2]^n$ was assumed and the rate as a function of temperature and concentrations of reactants was analyzed. Conversion was

not a constant parameter while obtaining kinetics data (10-35%). Figure 16 shows the dependence of reaction rate on conversion for 0.01%Pd+10%Ag_2.0 nm catalyst, obtained from pathway analysis. Data obtained from ~10 to ~50% conversion represent true kinetics as the reaction rates are constant, i. e. not a function of conversion.

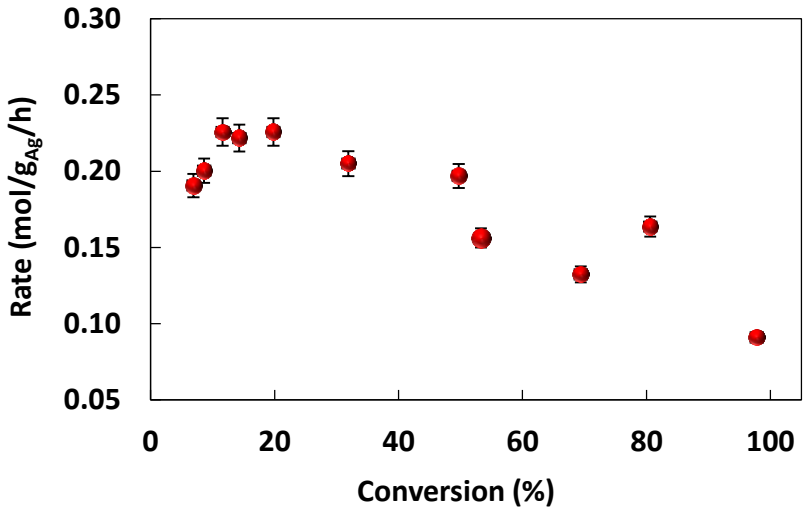

Figure 16. Reaction rate as a function of conversion for 0.01%Pd+10%Ag_2.0 nm sample.

The reaction orders for acrolein and H_2 were determined by measuring the reaction rates as the concentration of one reactant while holding the concentration of other constant. The dependence of reaction rate on the concentration of acrolein was determined at 200 °C in excess of H_2. The flow rate of acrolein was varied, and the ratio of H_2 to inert gas (Ar) was kept constant. The H_2 reaction order was determined at 220 °C keeping acrolein and total flow rates constant. The effect on H_2 reaction orders due to the temperature increase is expected to be minimal, if any, as the dependence of rate orders on temperature is small. The tests were not done in excess of acrolein. However, the examined range was such that for larger acrolein concentrations kinetics approaching those with excess acrolein were obtained. The reaction order of H_2 obtained at higher acrolein concertation was used to determine the apparent activation

energy, rate constant and the pre-exponential factor in Arrhenius equation. The total flow rate was kept constant by compensating the difference with Ar gas to keep the contact time with catalyst bed consistent as well as to provide the even flow distribution through the catalyst bed.

By performing the experiments at different temperatures at constant flow rates, the temperature dependence of the reaction constants as given by Arrhenius equation ($k = A\, e^{-E_a/(RT)}$) was obtained. The apparent activation energy of the reaction was calculated from the slope of the Arrhenius plot in Figure 17. A linear correlation of the reaction rates to temperature was found for all catalyst samples, indicating that the chosen rate expression probably correctly describes the reaction occurring, and as such, the apparent activation energy of the catalysts (TABLE V) is assumed to represents the rate-determining step in the reaction.

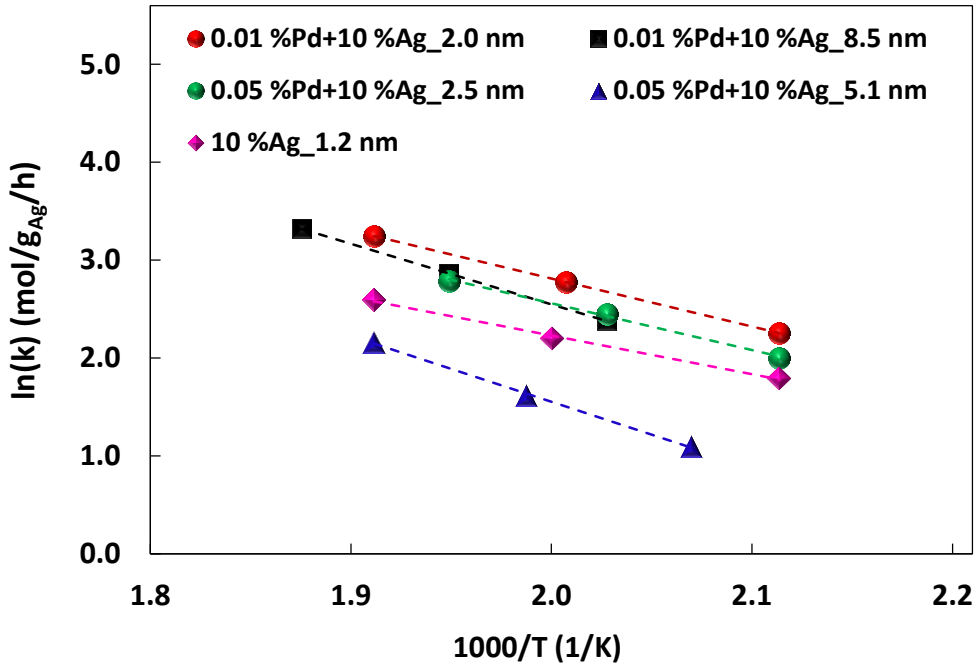

Figure 17. Arrhenius plot of hydrogenation of acrolein for Pd-Ag SAA and pure Ag catalysts.

TABLE V
KINETICS DATA FOR Pd-Ag SAA AND Ag CATALYSTS

Samples	r ($mol/g_{Ag}/h$)	Ea (kJ/mol)	m [Acrolein]	n [a] [H_2]	Reaction order [b]	A ($mol/g_{Ag}/h$)
10%Ag_1.2 nm	0.153	32.6	0.6	0.8	1.5	2.6×10^4
0.01%Pd + 10%Ag_2.0 nm	0.226	40.6	0.7	0.9	1.6	2.7×10^5
0.01%Pd + 10%Ag_8.5 nm	0.082	52.3	0.8	1.0	1.8	3.7×10^6
0.05%Pd + 10%Ag_2.5 nm	0.238	39.9	0.6	0.4	1.0	1.9×10^5
0.05%Pd + 10%Ag_5.1 nm	0.166	55.7	0.6	0.3	0.9	3.2×10^6
8%Ag/SiO_2 8.7 nm [c]	0.139	42.0	0.8	0.6	1.4	1.0×10^4

[a] Data obtained at 220 °C with excess concentration of acrolein in feed.

[b] Overall reaction order, determined from the sum of m and n.

[c] Wei et al. [32].

TABLE V shows the kinetics parameters of Pd-Ag SAAs and the monoatomic silver catalysts. First we will establish the correlation between 10%Ag_1.2 nm catalyst obtained in this study and 8.7 nm Ag/SiO_2 sample [32]. Increase in H_2 order for 10%Ag_1.2 nm catalyst implies lower surface concentration of hydrogen on small particles, while the opposite is true for acrolein. The magnitude of change (0.2) shows that the surface concentrations of acrolein and H_2 are inversely proportional, indicating a possible competition for the same adsorption sites. As the overall order of the reaction stays the same (~1.5), the mechanism of promotion is expected to remain unchanged.

Interestingly, small change in reaction order of acrolein is observed. It appears that 0.05%Pd-Ag SAAs of any size affect the surface concentration of acrolein in similar manner to the small Ag particle, whereas 0.01%Pd-Ag SAAs have a similar affect as a large Ag particle. In contrast to acrolein, reaction order of H_2 is changed from first order on 0.01%Pd-Ag SAAs to less than ½ order on 0.05%Pd-Ag SAAs. This implies that the significantly larger concentration of surface hydrogen on 0.05%Pd-Ag SAAs is probably correlated to presence of conjugate Pd atoms. Values for the overall reaction order indicate that on 0.05Pd%-Ag SAAs the reaction is

first order, and that the reaction is second order on 0.01Pd%-Ag SAAs. Even more interesting is that for monometallic Ag, the reaction order is in the middle (1.5).

Furthermore, at constant particle size, activation energies show no dependence on the amount of Pd. However, with an increase in particle size the activation energy on monometallic Ag increases by 10 kJ/mol, on 0.01%Pd_Ag SAA by 12 kJ/mol, and on 0.05%Pd-Ag SAA by 15 kJ/mol. These observations indicate that the performance of these catalysts is a delicate balance between the surface morphology and alloying effect. The origin of this morphology-dependence might be related to the activation energy for the formation of the reaction intermediates on silver surface planes [52, 53], whereas the change in the reaction order implies the change in the rate determining step from 0.01%Pd-Ag SAA to 0.05%Pd_Ag SAA catalysts.

1.3.4 Reaction Mechanism

For the kinetic modeling of the hydrogenation of acrolein over a Pd-Ag SAA catalyst, the reaction network in Figure 18 is used, excluding possible deactivation. It should be noted that during the initial transient phase the overall conversion of acrolein decreases and the product distribution changes with time on stream (Figure 4). The duration after which the quasi-steady state is observed is found to be inversely proportional to the gas flow rate, but independent of acrolein partial pressure. Therefore, it is assumed that the initial catalyst deactivation could be due to the formation of coke deposits from the starting products parallel to the hydrogenation reaction. As all catalysts reach steady state (~2 to 4 hours), implies that the deactivation and self-regeneration proceed simultaneously. Therefore, these steps are not the rate limiting, as they are essentially faster.

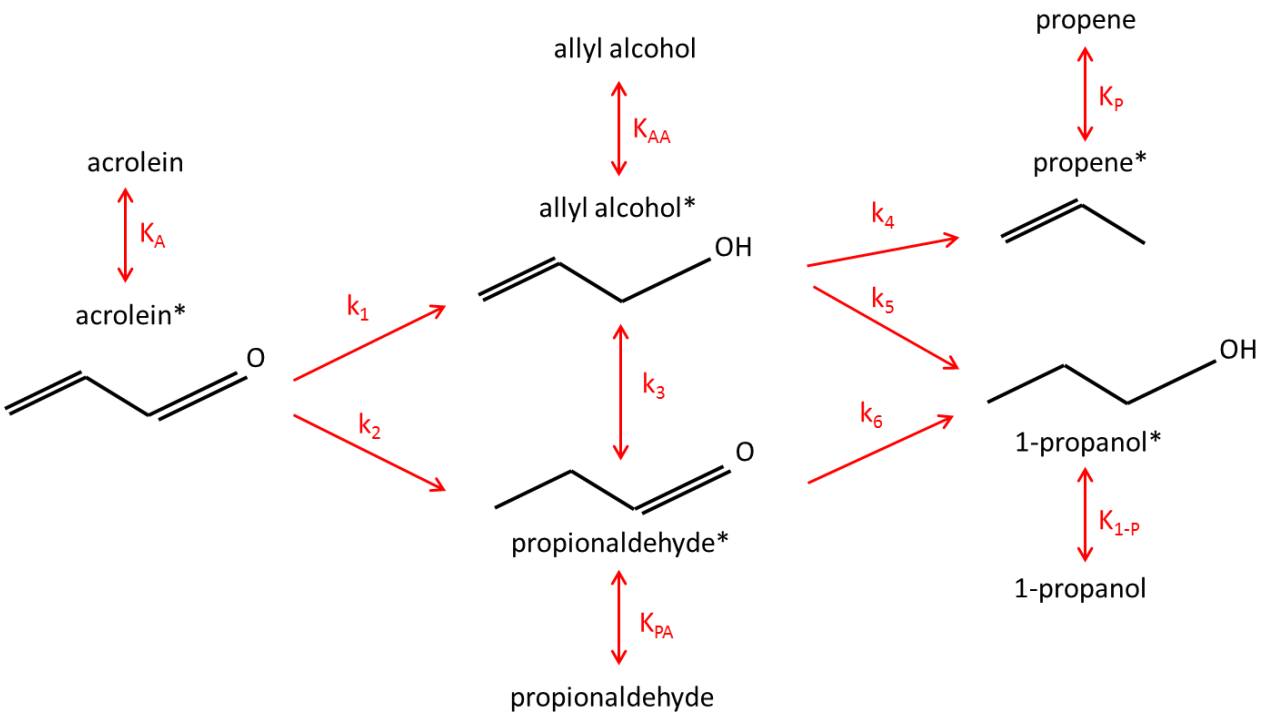

Figure 18. Reaction network for hydrogenation of acrolein (* indicates surface bound species).

The kinetic model is based on the Langmuir–Hinshelwood formalism using a quasi-steady state rate approximation. Possible elementary steps involved in a catalytic transformation, such as adsorption of the reactants (hydrogen and acrolein), surface hydrogenation and isomerization reactions, and desorption of the products are listed in TABLE XI, Appendix. The insight gained from the experimental data significantly reduces number of kinetically relevant reactions. Hydrogenation and isomerization are the only surface reactions considered, even though reactions such as decarbonylation and oligomerization are possible. However, in the time interval of reaction testing the product formation was not significant enough to obtain any measurable data. As determined by the pathway analysis, data obtained in 10 to 40% conversion range is applicable for the analysis of the reaction kinetics. The isomerization of allyl alcohol to propionaldehyde is not considered as a possible rate-determining step, as irrespective of the

change in selectivity to isomerization with change in conversion, the overall product distribution remains the same (especially from ~10 to ~80% conversion). This indicates that elementary reactions occurring prior to the isomerization of allyl alcohol are the only possible rate-determining steps. As the overall reaction is highly exothermic, surface reactions are assumed irreversible.

Adsorption/desorption steps are modeled using a quasi-equilibrium approximation. The surface concentration of various reaction intermediates and products is assumed small relative to the reactants. As such, it is not considered to be competing for the adsorption sites. Total surface coverage is based on the concentrations of the reactants (acrolein and H_2), and of the most likely reaction intermediates [20] and products in the initial hydrogenation of acrolein to allyl alcohol (hydroxyallyl) or propionaldehyde (n-formylethyl). Proposing a rate expression that accurately describes the promotion mechanism on Pd-Ag SAA catalysts is further complicated by different types of adsorption sites (Ag only, Pd and Ag), and multiple adsorption geometries of acrolein (C = C or C = O bonded). As such, adsorption is model as competitive (one type of active site) and as noncompetitive (two different active sites).

To develop the rate expressions, following notation for reaction species is used: acrolein (*AC*), allyl alcohol (*AA*), propionaldehyde (*PA*), hydroxyallyl (*HA*) and n-formylethyl (*F*). A simplified reaction sequence is proposed for hydrogenation of acrolein to form allyl alcohol via hydroxyallyl intermediate (Hydrogenation to propionaldehyde via n-formylethyl intermediate is shown in Appendix). Surface site is expressed as *, partial pressure of species i as P_i, equilibrium rate constants as $K_i = k_i / k_{-i}$, and adsorption and desorption rate constants for species *i* as k_i and k_{-i}, respectively.

$$H_2 + 2* \overset{K_{H_2}}{\longleftrightarrow} 2H^*$$

$$AC + * \overset{K_{AC}}{\longleftrightarrow} AC^*$$

$$AC^* + H^* \overset{K_1}{\longleftrightarrow} HA^* + *$$

$$HA^* + H^* \overset{K_2}{\longleftrightarrow} AA^* + *$$

$$AA^* \overset{K_{AA}}{\longleftrightarrow} AA + *$$

For the competitive adsorption, the mechanism is further simplified with an assumption that there exists only one equilibrium adsorption constant for acrolein and hydrogen. Total site balance in terms of fractional coverage of each species (θ_i = surface concentration of species i with respect to total surface site concentration) is expressed as

$$1 = \theta^* + \theta_{AC} + \theta_H + \theta_{AA} + \theta_{HA}$$

Rate expressions are obtain by assuming one of the reactions is rate limiting, while all others are equilibrated. Result providing the "best fit" to experimental data is chosen to express the rate law in terms of equilibrium constants and partial pressures of the reactants (details provided in Appendix). Following is a list of rate expressions obtained by competitive adsorption model:

- Dissociative H_2 adsorption as the rate-limiting step

$$r_{H_2} = \frac{k_{H_2} P_{H_2}}{\left[1 + K_{AC}P_{AC} + K_{AA}P_{AA} + \left(\frac{K_{AA}P_{AA}}{K_1 K_2 K_{AC} P_{AC}}\right)^{1/2} + \left(\frac{K_1 K_{AC} P_{AC} K_{AA} P_{AA}}{K_2}\right)^{1/2}\right]^2}$$

- Molecular (non-dissociative) adsorption of acrolein as the rate-limiting step

$$r_{AC} = \frac{k_{AC} P_{AC}}{1 + \left(K_{H_2} P_{H_2}\right)^{1/2} + K_{AA}P_{AA}\left[1 + \frac{1}{K_1 K_2 K_{H_2} P_{H_2}} + \frac{1}{K_2\left(K_{H_2} P_{H_2}\right)^{1/2}}\right]}$$

- Irreversible surface hydrogenation of acrolein to hydroxyallyl as the rate-limiting step

$$r_1 = \frac{k_1 K_{AC} P_{AC} \left(K_{H_2} P_{H_2}\right)^{1/2}}{\left[1 + K_{AC} P_{AC} + \left(K_{H_2} P_{H_2}\right)^{1/2} + K_{AA} P_{AA} \left(1 + \frac{1}{K_2 \left(K_{H_2} P_{H_2}\right)^{1/2}}\right)\right]^2}$$

- Irreversible surface hydrogenation of hydroxyallyl to allyl alcohol as the rate-limiting step

$$r_2 = \frac{k_2 K_1 \, K_{AC} P_{AC} K_{H_2} P_{H_2}}{\left[1 + K_{AA} P_{AA} + \left(K_{H_2} P_{H_2}\right)^{1/2} \, + K_{AC} P_{AC} \left(1 + K_1 \left(K_{H_2} P_{H_2}\right)^{1/2}\right)\right]^2}$$

First expression (H_2 dissociation as the rate-limiting step) is discarded based on a fixed value for H_2 reaction order, which implies that the surface coverage of hydrogen is independent of reaction condition (H_2 order changes from 0.3 to 1). The partial pressure of allyl alcohol is expected to be lower than of acrolein and hydrogen, so that $P_{AA} << P_{H2}$ and P_{AC}, which reduces the rate expressions to

$$r_{AC} = \frac{k_{AC} P_{AC}}{1 + \left(K_{H_2} P_{H_2}\right)^{1/2}}$$

$$r_1 = \frac{k_1 \; K_{AC} P_{AC} \left(K_{H_2} P_{H_2}\right)^{1/2}}{\left[1 + K_{AC} P_{AC} + \left(K_{H_2} P_{H_2}\right)^{1/2}\right]^2}$$

$$r_2 = \frac{k_2 \; K_1 \, K_{AC} P_{AC} K_{H_2} P_{H_2}}{\left[1 + \left(K_{H_2} P_{H_2}\right)^{1/2} \, + K_{AC} P_{AC} \left(1 + K_1 \left(K_{H_2} P_{H_2}\right)^{1/2}\right)\right]^2}$$

It can be assumed, that relative to hydrogen, acrolein is weakly adsorbed on the surface, so that at similar partial pressures $K_{AC} << K_{H2}$, reducing the expressions to

$$r_{AC} = \frac{k_{AC} P_{AC}}{1 + \left(K_{H_2} P_{H_2}\right)^{1/2}}$$

$$r_1 = \frac{k_1 \ K_{AC} P_{AC}}{\left(K_{H_2} P_{H_2}\right)^{1/2}}$$

$$r_2 = \frac{k_2 \ K_1 \ K_{AC} P_{AC} K_{H_2} P_{H_2}}{\left[1 + \left(K_{H_2} P_{H_2}\right)^{1/2} \ \right]^2}$$

Weak dependence to reaction conditions was exhibited by acrolein, while the effect was substantially enhanced for H_2 (first order kinetics on 0.01%Pd-Ag SAAs and less than 0.5 on 0.05%Pd-Ag SAAs). At high pressures, the reaction can be inhibiting due to saturation of the surface (conditions closely resembling the observed performance of 0.05%Pd-Ag SAAs while opposite is observed on 0.01%Pd-Ag SAAs). As such, at high pressures the rate expressions become

$$r_{AC} = \frac{k_{AC} P_{AC}}{\left(K_{H_2} P_{H_2}\right)^{1/2}}$$

$$r_1 = \frac{k_1 K_{AC} P_{AC}}{\left(K_{H_2} P_{H_2}\right)^{1/2}}$$

$$r_2 = k_2 K_1 K_{AC} P_{AC}$$

For low pressure (corresponding to decreased in H_2 surface coverage on 0.01%Pd-Ag SAA) $K_{H2}P_{H2} << 1$, and the rate expressions become

$$r_{AC} = k_{AC} P_{AC}$$

$$r_1 = k_1 K_{AC} P_{AC}$$

$$r_2 = k_2 K_1 K_{AC} P_{AC} K_{H_2} P_{H_2}$$

Based on the competitive adsorption model, in all expressions acrolein is a first order reactant. This could be due to weak binding to the surface, or it could imply that acrolein surface concertation does not have a strong effect on the rate-determining step. Model correctly described data for 0.01%Pd-Ag SAA catalysts, when hydrogenation of hydroxyallyl to allyl alcohol is assumed as the rate-limiting step (first order for H_2 and acrolein). It should be noted that the all of the proposed rate expressions were analyzed at limit of high T as well. This model does not adequately describe the observations on 0.05%Pd-Ag SAAs, as both the adsorption of acrolein and the first hydrogenation step (acrolein to hydroxyallyl) are possible candidates, but not accurate enough (first order for acrolein and -0.5 order for H_2).

For the noncompetitive adsorption model, reaction occurs between two species adsorbed on different types of surface sites (only Ag atoms, or Ag and one Pd atom in the active site). Detailed analysis of all possible paths with respect to different combinations of adsorption sites can be done, however for our purposes a simple noncompetitive model in which the surface species will not displace each other will be sufficient. As such, expressions are derived using the same series of reaction steps as in competitive model. Total site balance in terms of fractional coverage of each species θ_i is

$$1 = \theta^* + \theta_i$$

The concentration of each species at equilibrium is expressed as

$$\frac{\theta_i}{1-\theta_i} = K_i P_i$$

Following is a list of rate expressions obtained by noncompetitive adsorption model:

- Dissociative H_2 adsorption as the rate-limiting step

$$r_{H_2} = \frac{k_{H_2} P_{H_2} K_{AC} P_{AC}}{\left[(K_1 K_2 K_{AC} P_{AC})^{1/2} + (K_{AA} P_{AA})^{1/2} \right]^2}$$

- Molecular adsorption of acrolein as the rate-limiting step

$$r_{AC} = \frac{k_{AC} P_{AC} K_{H_2} P_{H_2}}{K_{H_2} P_{H_2} + \frac{K_{AA} P_{AA}}{K_1 K_2}}$$

- Irreversible surface hydrogenation of acrolein to hydroxyallyl as the rate-limiting step

$$r_1 = \frac{k_1 \, K_{AC} P_{AC} \left(K_{H_2} P_{H_2}\right)^{1/2}}{(1 + K_{AC} P_{AC}) \left(1 + \left(K_{H_2} P_{H_2}\right)^{1/2}\right)}$$

- Irreversible surface hydrogenation of hydroxyallyl to allyl alcohol as the rate-limiting step

$$r_2 = \frac{k_2 \, K_1 \, K_{AC} P_{AC} K_{H_2} P_{H_2}}{1 + \left(K_{H_2} P_{H_2}\right)^{1/2}}$$

By applying the same procedure as in competitive model, the expressions for the limiting cases can be obtained. As such, at high pressure rate expressions become

$$r_{AC} = k_{AC} P_{AC}$$

$$r_1 = k_1 K_{AC} P_{AC}$$

$$r_2 = k_2 \, K_1 \, K_{AC} P_{AC} \left(K_{H_2} P_{H_2}\right)^{1/2}$$

At low pressure the rate expressions become

$$r_{AC} = k_{AC} P_{AC}$$

$$r_1 = k_1 \, K_{AC} P_{AC} \left(K_{H_2} P_{H_2}\right)^{1/2}$$

$$r_2 = k_2 \, K_1 \, K_{AC} P_{AC} K_{H_2} P_{H_2}$$

As with the competitive adsorption model, the behavior of the 0.01%Pd-Ag SAA catalysts is correctly predicted by assuming hydrogenation of hydroxyallyl to allyl alcohol as rate limiting. In addition, this model is able to provide a better fit for 0.05%Pd-Ag SAA catalyst, such

that first order is obtained for acrolein and half order for H_2. In the limit of high T, same rate-limiting step is concluded (first order in acrolein and zero order for H_2).

1.4 Conclusion

From all of the Pd-Ag catalysts tested, none exhibit higher selectivity than the most selective monometallic silver (39% selectivity for 8%Ag_10 nm sample). This implies that we cannot improve on the selectivity as it appears to be limited by the intrinsic property of the silver on a silica support. Although alloying may enhance reactivity by increasing the coverage of reactants on the surface, the preferential bonding of acrolein to the surface is through the C=C bond for any of the alloying elements we examined. In Aich et al. examination of a wider group of transition metal elements (including Cu and Au), the bonding of C=O to the surface is never favored (and is only isoenergetic at best).

The reaction rate of a well-dispersed Pd-Ag SAA is structure sensitive; i.e. reactivity is a function of particle size, with minimal dependence on the amount of Pd. The activity of Pd-Ag SAAs at constant Pd loading remains almost the same, within the particle size range examined, whereas the activity of monometallic Ag/SiO_2 catalyst triples. In addition, the activity of the catalysts exhibits much stronger dependence to particle size than the amount of Pd loading, as at any particle size only a small increase in TOF is observed with an increase in Pd loading from 0.01 to 0.05%.

Reaction pathway shows that at conversions above ~50%, Pd-Ag SAA catalysts will inhibit the isomerization of acrolein to allyl alcohol. Kinetics results indicate that the acrolein reaction order is not significantly affected, whereas reaction order of H_2 changes from first order on 0.01%Pd-Ag SAAs to less than half order on 0.05%Pd-Ag SAAs. This implies that the

significantly larger concentration of surface hydrogen on 0.05%Pd-Ag SAAs is probably correlated to presence of conjugate Pd atoms. The overall reaction order changes from first order on 0.05Pd%-Ag SAAs to second order on 0.01Pd%-Ag SAAs. Even more interesting is that for monometallic Ag, the reaction order is in the middle (1.5).

The performance of Pd-Ag SAA catalysts is a delicate balance between the surface morphology and alloying effect. The origin of this morphology-dependence might be related to the activation energy for the formation of the reaction intermediates on silver surface planes [52, 53], whereas the change in the reaction order implies the change in the rate determining step from 0.01%Pd-Ag SAA to 0.05%Pd_Ag SAA catalysts. Based on the noncompetitive adsorption model, it was shown that the rate-limiting step does indeed change from initial hydrogenation step (acrolein to allyl alcohol or propionaldehyde) on 0.05%Pd+10Ag SAAs to second hydrogenation step (hydroxyallyl to allyl or n-formylethyl to propionaldehyde) on 0.01%Pd-Ag SAA catalysts.

2. DFT STUDY OF THE ROLE OF PROMOTER IN VANADIUM PROMOTED RHODIUM CATALYSTS FOR CO HYDROGENATION

2.1 Introduction

A thermochemical pathway for the catalytic synthesis of C_{2+} oxygenates (e.g. ethanol, acetaldehyde, and acetic acid) from syngas (a mixture of CO and H_2) can potentially allow for the production of higher octane fuels and alcohols which can subsequently be used as chemical intermediates for further synthesis of products such as plasticizers and detergents [3, 54-59]. However, a key issue of catalyst development has been control of the product selectivity as the best catalysts found to date produce a considerable amount of unwanted products resulting in wide distribution ranges of hydrocarbons with regard to length and oxygen content [60, 61]. For the catalyst to exhibit high selectivity for C_{2+} oxygenates, the interaction between the active sites and the adsorbates needs to be precisely balanced for the reaction to proceed in a favorable direction, as stated by the Sabattier principle [62]. In this case, successful selective alcohol synthesis must exhibit a compromise between strong CO adsorption, which leads to a low activation barrier and weak CO adsorption, which enables CO hydrogenation and CO insertion.

Transition metal-based catalysts have been widely explored as potential catalysts for the production of C_{2+} oxygenates via CO hydrogenation [54-58]. For example, cobalt is known to have high selectivity and activity for hydrocarbon production [54, 55], whereas nickel favors methanation (C-O scission and hydrogenation) [56-58]. Today, catalytic conversion of syngas to C_{2+} oxygenates is often performed using promoted Rh catalysts due to rhodium's ability to catalyze both C-O dissociation and CO insertion, two main prerequisites for higher alcohol production [63-66]. Rhodium's moderate activity and good selectivity toward oxygenated products has been explained in terms of the position of its *d*-electrons, which is intermediate relative to metals which do not dissociate CO (Ir, Pd, Pt), and those which easily dissociate CO

under reaction conditions (Co, Ru, Fe) and therefore favor higher hydrocarbon production [60, 67-73]. However, the majority of CO hydrogenation studies using unpromoted Rh have observed a strong selectivity for methane with a low oxygenates selectivity [60, 72].

2.1.1 Mechanism of CO Hydrogenation

C_{2+} oxygenate synthesis from syngas is a complex reaction network that consists of a large number of elementary steps, many of which are not probable as determining factors to reactivity. CO hydrogenation has been shown to occur via two mechanisms (Figure 24): direct CO dissociation (carbide mechanism) originally suggested by Fischer and Tropsch in 1926 [67] and later refined by Craxford and Rideal[74], and hydrogen assisted CO dissociation [75]. In the direct CO dissociation mechanism (Figure 24a) CO adsorbs and dissociates to form surface carbide and oxygen species. The carbide species undergo hydrogenation to CH_x species. Next, another CO will be inserted into a CH_x intermediate to form an enol species, before this intermediate is further hydrogenated and finally desorbs [67]. In the H-assisted CO dissociation mechanism (Figure 24b) CO adsorbs and reacts with hydrogen to form either HCO (formyl) or COH (and could conceivably be further hydrogenated to CH_xO). Hydrogenation weakens the C–O bond and enables bond dissociation. Another CO will be inserted and the intermediate will be further hydrogenated and desorb [75].

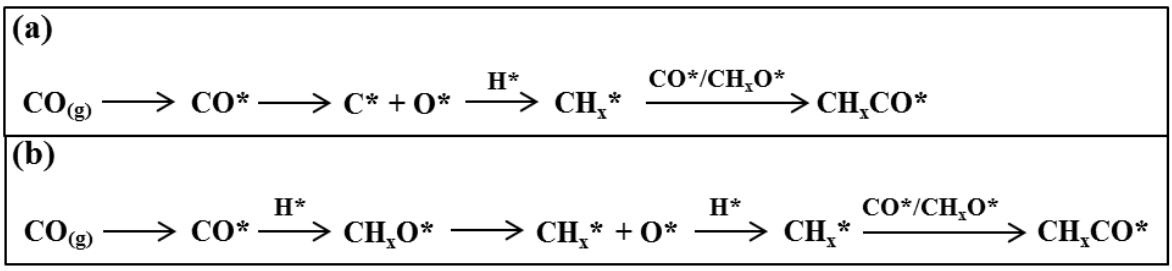

Figure 19. (a) Direct CO dissociation mechanism, and (b) H–assisted CO dissociation mechanism (* indicates surface species).

Irrespective of the prevailing mechanism, a successful catalyst has to exhibit a compromise between strong CO adsorption, which leads to a low activation barrier for CO dissociation, and weak CO adsorption, which enables CO hydrogenation and CO insertion. It has been suggested that C-O bond dissociation is the rate-limiting step for higher alcohol synthesis [76, 77]. However, it is still unknown whether the C-O bond scission occurs prior to hydrogenation of CO surface species or if hydrogenation is required before the scission takes places. Moreover, CH_4 is the thermodynamically favored product for CO hydrogenation under typical reaction conditions (240-350 ºC and pressure in excess of 50 bar) suggesting that an increase in C_{2+} oxygenate selectivity can only be attained by imposing a kinetic limitation to methanation process [60].

Numerous studies have shown that the product selectivity can also be affected by surface morphology due to a change in CO adsorption mode [69, 78, 79]. Evidence indicates that closely spaced step and kink sites play a major role in promoting dissociation of adsorbed CO. CO dissociation was shown by Mavrikakis et al. to be extremely structure sensitive, such that the Rh(111) surface cannot dissociate CO, while steps and other defects may be able to break the C-O bond [69]. This was correlated to undercoordinated metal atoms having a higher *d*-band center, which makes them more reactive. Ren et al. used a high resolution voltage-pulsed atom-probe (HRVP AP) to show that CO adsorbs only molecularly on Rh(111) and Rh(001) surface planes as compared with stepped sites, where CO dissociates with low barrier [78]. Partial CO dissociation was observed on undercoordinated Rh surfaces, and molecular CO adsorption on Rh(111) and Rh(001) planes with the trace of dissociation on higher index plane Rh(113) was observed by Liu et al. [79].

Syngas conversion conditions will cause a near saturation adsorbate coverage, significantly influencing the binding energies of adsorbed species and of reaction intermediates [80]. Lateral interactions between surface species are expected to decrease the adsorption energies and enhance the mobility of the adsorbed species [81]. Destabilization of spectator CO surface species and intermediate species is expected, increasing the feasibility of CO insertion. As shown by Ojeda et al., on 0.5 ML CO covered Fe(110) and Co(0001), surface the binding energies of the surface species decreased by more than 20 kJ/mol compared to the bare surface [82, 83]. Therefore, the incorporation of relevant surface coverage is of principal importance when using theoretical models to simulate heterogeneous catalytic reactions.

The H-assisted CO dissociation mechanism is expected to be the principal mechanism at high adsorbate coverage reaction conditions, facilitating a reaction of intermediates such as formyl (HCO) or COH with adsorbed species instead of reactions involving vacant sites [80, 84]. The direct CO dissociation mechanism is likely to be slow, regardless of the coordination of surface, due to lack of vacancies. A detailed density functional theory (DFT) and microkinetic study of ethanol synthesis on Rh(111) surface was performed by Choi and Liu [68]. It was concluded that a H-assisted CO dissociation via formyl intermediate followed by subsequent CO insertion into CH_3 is the dominant mechanism. An extremely high barrier for CO dissociation (3.72 eV) was identified whereas formation of formyl had a barrier of only 1.28 eV (which was also the rate-limiting step in the mechanism). CO bond cleavage did not occur until CO was hydrogenated to methoxy (CH_3O) at which point C-O bond cleavage becomes favorable with respect to further hydrogenation to CH_3OH (and subsequent desorption), concluding that the selectivity of ethanol on Rh(111) depends on the reaction barriers of CH_3 insertion to form acetyl versus hydrogenation which forms methane. Three major products were formed (CH_4, CH_3OH

and C_2H_5OH), determining that the unpromoted Rh(111) surface is highly selective to methane, exhibiting very low selectivity to ethanol. It was suggested that promotion is necessary to suppress methane formation by lowering the barrier for C-C bond formation.

Choi and Liu found that on Rh(111) the initial step is dominated by hydrogen assisted mechanism to produce formyl, followed by subsequent CO insertion [68]. Ojeda et al. provided experimental and theoretical evidence for hydrogen-assisted CO activation as the predominant mechanism on Fe and Co catalysts for FTS [82]. King and coworkers found that on Co(0001) adsorbed CO will be hydrogenated to CH_2O to yield the CH_2 building block for polymerization in the Fischer-Tropsch process. Hydrogenation to HCO and subsequently to CH_2O successively weakens the CO bond (C-O bonded parallel to the surface through both oxygen and carbon) leading to a lower activation barriers for C-O bond cleavage (E_{act} = 2.82, 1.00 and 0.85 eV for CO, HCO and CH_2O respectively) [83].

Similarly, Zhuo et al. investigated the effect of 0.3 ML CO coverage on CO insertion mechanism for Co(0001) surface [81]. Reaction intermediates (such as CH and CHCO) were 10-30 kJ/mol less stable in the presence of co-adsorbed CO and the calculated TOF (turnover frequency) for CO insertion was increased by five orders of magnitude (in agreement with experimental values) compared to results obtained with low CO coverage. The CO insertion barrier was reduced by more than 60 kJ/mol [81]. Zao and coworkers compared CO vs HCO insertion pathways on Rh (111) and Co(0001) [85]. For Rh(111) it was found that HCO insertion is both thermodynamically and kinetically preferred. The superior activity of HCO compared to CO was attributed to greater charge transfer and hybridization between HCO and the surface due to the variation in HOMO and LUMO energy levels and the smaller HOMO-LUMO gap of HCO compared to CO [85]. Compared to CO, the HOMO level of HCO is shifted upward and the

LUMO level downward; therefore, both levels are closer to the *d*-band centers of transition metals. As a consequence, HCO and CO interact in completely different geometric configurations with the substrates at the transition states [85]. Analogous results on Rh(111) were obtained by Choi and Liu in addition suggesting that promotion is necessary to suppress CH_4 formation by increasing the barrier for CH_3 hydrogenation [68].

Eckle et al. identified adsorbed formyl species using time-resolved DRIFTS measurements [84]. They classified adsorbed formyl with a characteristic band at 1760 cm^{-1} as the reaction intermediate for CO methanation in a $CO/H_2/N_2$ mixture on the Ru/Al_2O_3 catalyst under reaction conditions typical for reformate purification. The identification of formyl as a reaction intermediate rather than a spectator species was based on its formation/reaction rate under steady state conditions, which is of similar order of magnitude as the overall ration rate (CH_4 formation rate) [84].

2.1.2 Rh Promotion

Promotion of Rh catalyst via addition of a second metal performs some critical function dramatically shifting the energetics in the reaction mechanism [60, 72, 86]. For example, Mn promotion of Rh(100) surface was analyzed by Li et al., with aim to modify the observed low activity of Rh(111) surface for CO dissociation [87]. CO dissociation barrier (E_{act} = 0.52 eV) and the CO insertion into chemisorbed CH_3 (E_{act} = 0.30 eV) were both significantly lowered on the Mn monolayer modified Rh(100) compared to the Rh(100) surface (E_{act} = 2.31 and 0.43 eV for CO dissociation and CH_3 insertion, respectively). This was attributed to shift in *d*-band center to higher energy for Mn/Rh(100) which causes more empty *d*-states in turn increase in bonding

strength of CO. In addition, Mn modified surface showed a very small CO + CH_3 barrier of only 0.30 eV, compared to a 0.64 eV barrier for CH_3 hydrogenation.

In a different study, highly oxophilic ions such as Mn, Ti, Zr, and Nb where shown to enhance CO dissociation when located at the Rh surface [86]. Mei et al. postulated that the selectivity and activity of the promoted Rh/M/SiO_2 catalysts (M = Ir, Ga, V, Mn, Ti, Sc, Ca and Li) can be correlated to the electronegativity difference between Rh and the promoter M [70]. The postulate was based on observation that Mn embedded in Rh matrix has a small partial positive charge and acts as a mild Lewis acid site, which favors CO insertion reactions. Their calculations show that the activation barrier for CO insertion into CH decreases with increasing electronegativity difference up to 0.7, after which it increases with increase in electronegativity difference. It was determined that promoters such as Ti, Mn and V yield the best selectivity and productivity for ethanol [70].

The addition of a second promoter such as Li, Na, and K, was shown to further improve the selectivity toward C_2-oxygenates by suppressing the hydrocarbon selectivity [60]. A combined promoting effect of La and V oxides on CO hydrogenation on Rh/SiO_2 catalysts was investigated by Gao et al. [88]. The singly promoted catalysts, Rh-La/SiO_2 and Rh-V/SiO_2, showed improved reactivity (3x) and better ethanol selectivities than the non-promoted Rh/SiO_2 catalyst. However, the doubly promoted Rh-La-V/SiO_2 catalyst showed even higher activity (9x) and selectivity for ethanol and other C_{2+} oxygenates, with the selectivity of total C_{2+} oxygenates greater than 30% at low pressure reaction conditions. The improved performance of the Rh-La-V/SiO_2 catalyst was suggested to be due to a synergistic promoting effect of the combined La and V additions through intimate contact with Rh [88].

Subramani et al. summarized the promotion effects for SiO_2 supported Rh catalyst by relating the promoter type (i.e. position on the periodic table) to both the catalytic activity and selectivity for ethanol formation [89, 90]. Promoters such as Zr, Ti, and V were found to exhibit higher catalytic activity, whereas La, Ce, Y displayed higher ethanol selectivity [60]. As most promoters exhibit a potential to effect only specific steps in reaction mechanisms, it is of interest to note that promotors such as V, Ti and La can affect both CO dissociation as well as CO insertion reaction [63]. Some authors have suggested that the function of V is to boost hydrogenation [91, 92]. Beutel et al. have characterized the impact of promotion on V, Nb and Ta oxide promoted Rh/SiO_2 catalysts using FTIR spectroscopy of adsorbed CO at 85 K [91]. The promotion led to an increase in the overall CO hydrogenation activity, in the order V<Nb<Ta. In addition, selectivity shifted from methane and acetaldehyde for the unpromoted Rh/SiO_2 catalyst to ethanol and methanol over promoted catalysts, where ethanol selectivity changed from 1% for unpromoted to 40% for promoted catalyst [91].

In a different study, the influence of the Rh active component modified by V promoter and of adsorbed hydrogen was performed via IR spectra of adsorbed CO ($Rh\text{-}V/SiO_2$) [70]. The results showed appreciable red shifts of CO bands on promoted catalyst cooled in H_2 to room temperature after reduction by hydrogen at 300°C and exposure to gaseous CO, and no shift to promoted and unpromoted catalyst outgassed at 300°C after reduction. The authors concluded that the high selectivity and activity of V promoted Rh catalysts in the synthesis of C_{2+} oxygenates is a combined effects of Rh, lower valence V and activated hydrogen [70].

As the precise physical relationship between the promoter and the metal catalyst is still largely unknown, it is unclear how to model the promoted catalyst. Common practice is to model the promoter element as an isolated metal atom [93, 94]. However, evidence suggests that the

active phases are often not metallic [95, 96]. Furthermore, modeling a promoted catalyst in DFT can be significantly affected by the location of the promoter in the unit cell [97]. Linic and Barteau found that the difference between the barriers for acetaldehyde formation and ethylene oxide formation is increased by the presence of Cs, leading to a higher selectivity to ethylene oxide, and that the location of Cs in the unit cell was critical to the stability of the transition state [97].

Promoters are added generally as complexes with formal oxidation states other than zero since the calcination/reduction treatment to which the catalysts are exposed often do not result in complete reduction to miscible alloys. A number of studies have indicated that variations in reaction conditions will cause the VOx deposited on metal surface to change structure and composition easily [98-100]. Therefore, a catalyst's surface can possibly contain metallic V atoms along with any form of oxidized clusters (VOx), in concentrations dependent on temperature and partial pressures of reactants. Furthermore, it is unclear if the promoter is present in clusters or if the reaction takes place at an interface between the promoter (oxide cluster) and the metal. This type of "reverse" catalyst model has been studied experimentally by Schoiswohl et al. [101-103]. Although structural models for a VOx clusters supported on Rh(111) have been developed by the Netzer group, their catalytic activity has not been explored.

Kip et al. investigated the influence of V_2O_3 promotion on CO hydrogenation over Rh/SiO_2 [104]. They have shown that the selectivity to C_{2+} oxygenates was significantly improved; however, the CO insertion reaction was only slightly influenced by the promoter oxides. [105]. Gronchi et al. [106] used TPD and TEM to show that the adsorption and catalytic properties of Rh/V_2O_3 are influenced by Rh dispersion. With the increase in temperature up to 500 K, the size of rhodium particles increases causing the fraction of sites capable of CO

dissociation to increases. Due to V_2O_3 promotion, subsequent chain growth (i.e. C-C bond formation) between carbidic surface species improves, increasing the chance for chain growth by about 70% [106].

PSRA (pulse surface reaction rate analysis) was used by Mori et al. to investigate CO hydrogenation on vanadium oxide on Ru/Al_2O_3 surface [107]. Promoter increased the rate constant for the dissociation of CO to form CHx, while decreasing the rate constant for the hydrogenation of CHx to CH_4 [107]. In addition, an increase in surface concentration of (CH) was observed. A promotion mechanism via metal-oxide interface site was proposed in which a metal bound CHOH intermediate adjacent to a V^{3+} oxide ion experiences a pull that promotes dissociation into CO + CH with a simultaneous ion oxidation to V^{4+}. V^{3+} ion was said to reform upon hydrogenation of OH to H_2O [107]. Similarly, V^{3+}/V^{2+} redox model was experimentally observed by Boffa et al. for VO_x on polycrystalline Rh [100]. Using the shifts in core levels in XPS they found a change in the proportion of vanadium's oxidation states (+3 to +2) upon a change in the temperature of the catalyst [100].

As can be seen, a complex reaction network for CO hydrogenation and the formation of various VOx surface structures have been extensively studied. However, a universal mechanistic description of the active sites goes beyond the scope of this work. Instead, our aim is to perform a systematic study to provide insight into the observed catalytic performance as various functions of vanadium have been proposed. Reaction conditions are simulated by imposing a 0.3 ML CO coverage on V/Rh(211) and V_6O_{12}/Rh(111) surfaces. The binding energies of all relevant intermediate species, reaction enthalpies and activation barriers are reported for a subset of model reactions (C-O dissociation, C-H hydrogenation and C-C bond formation) in H-assisted CO dissociation mechanism. Using a Bader charge analysis [108] and Density of States (DOS)

profile [109], the electronic charge on all relevant atoms for the site of interest was obtained and used to help explain the promotion mechanism. For V_6O_{12}/Rh(111) surface, a redox promotion mechanism is observed which can be correlated to previously experimental observations [100, 107].

2.2 Computational Methodology

Results are obtained with density functional theory (DFT) calculations implemented in the Vienna *Ab initio* Simulation Package (VASP) [45, 46]. The generalized gradient approximation with the Perdew-Wang exchange-correlation functional (GGA-PW91) is utilized to calculate exchange and correlation energies [47]. The calculations were performed using a plane wave basis set and ultrasoft pseudopotentials with periodic supercells. The kinetic energy cutoff for the plane wave basis set is 400 eV. Geometries are considered to be optimized when the forces are within a convergence tolerance of 0.02 eV/Å. It should be noted that the GGA-PW91 pseudopotential incorrectly predicts the most favorable CO adsorptions site on metal surfaces and overestimates the CO biding energies [47, 110]. Transition states are calculated using the climbing nudged elastic band method as described by Henkelman et al.[111]. Adsorption energies are calculated according to $E_{ads} = E_{A/Rh} - E_{Rh} - E_{A/gas}$ in which Eads is the adsorption energy of a molecule A on the surface and $E_{A/Rh}$, E_{Rh} and $E_{A/gas}$ represent the total energies of the adsorbate system, the CO saturated surface and the free adsorbent in gas-phase, respectively.

These nonspin-polarized calculations were run with 15 Å of vacuum space above all unit cells to ensure negligible interaction between slabs. The Brillouin zone is sampled using a 3 x 3 x 1 Monkhorst-Pack k-point grid with Methfessel-Paxton smearing of 0.2 eV [48]. Rh(211) surface was modeled by 6 layered slab for a (5 x 3) unit cell and the atomic positions for the bottom

three layers were kept fixed (Figure 20 d-f). Based on a structure model for a VOx clusters supported on Rh(111) developed by Schoiswohl et al. [103], we have simulated a V_6O_{12} cluster on Rh(111) surface as a four layered slab for a (5 × 5) unit cell with the atomic positions for the bottom two layers kept fixed (Figure 20 a-c). The VOx cluster contains 6 V atoms located 2.26 Å above the fcc and hcp threefold hollow sites of the Rh(111) surface, 6 bridging O atoms approximately 3.0 Å above Rh surface, and 6 peripheral O atoms 2.07 Å on atop position above surface Rh. Distance between V and bridging O is 1.79 Å. V bonds to peripheral O are 1.70 Å.

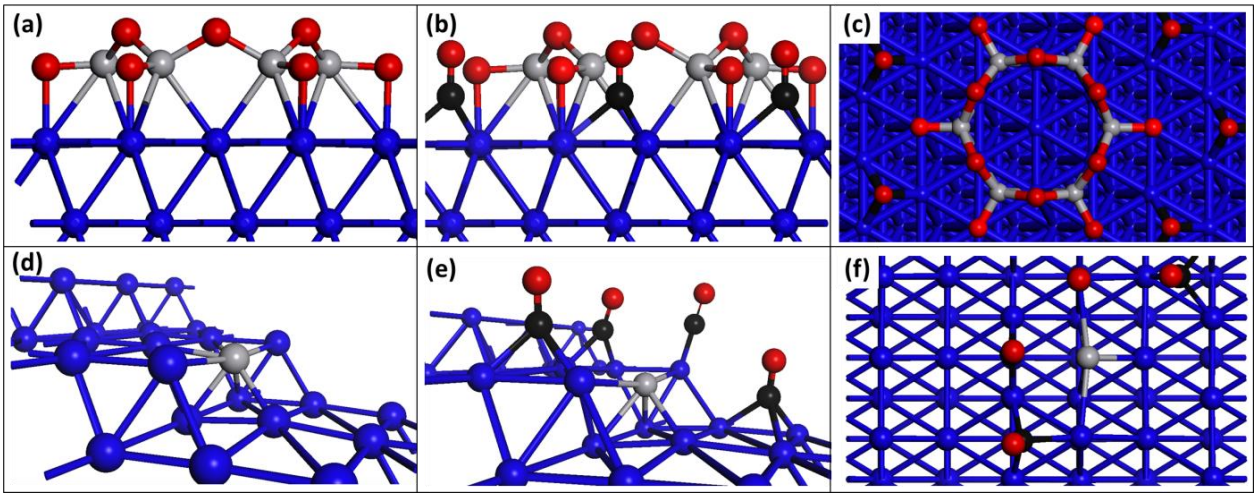

Figure 20. Schematic presentation of V_6O_{12}/Rh(111) surface (a) side view of pristine surface, (b) side view and (c) top view with 0.3 ML CO surface coverage, and V/Rh(211) surface (d) side view of pristine surface, (b) side view and (c) top view with 0.3 ML CO surface coverage. Colors representation: Rh (blue), V (gray), O (red) and C (black).

The electronic structure of the models is analyzed in terms of Bader charges and partial density of states (PDOS). Bader charge analysis was performed using a code developed by Henkelman et al.[108]. This method divides the electron density (space) around given atoms into regions separated by zero-flux surfaces on which the charge density is a minimum perpendicular to the surface. Bulk geometry optimization (VO, VO_2, V_2O_3 and V_2O_5) and PDOS DFT calculations were performed using the CASTEP package in Materials Studio 5.5 software by

Accelrys [109]. A 9×9×9 Monkhorst-Pack kpoint grid was used and all atoms were allowed to completely relax. Structures were optimized by allowing ion relaxation followed by a cell volume optimization; these cycles were repeated finishing with the ion relaxation step (Figure 21).

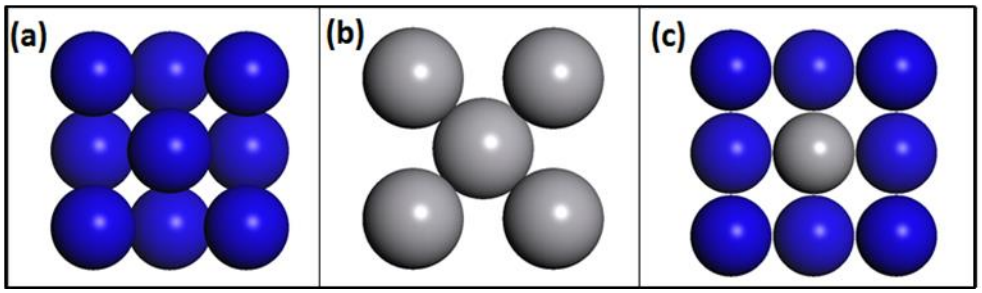

Figure 21. Schematic presentation of bulk (a) Rh, (b) V and (c) RhV.

2.3 Results and Discussion

The reactivity of the unpromoted Rh surface is well documented with general agreement that surface defects (steps and kinks) facilitate a direct CO dissociation mechanism producing mostly methane, a kinetically and thermodynamically preferred product [112]. As such, herein only changes to surface reactivity induced by V containing active sites are considered. However, to deduce which effects are directly related to V promotion first requires accounting for changes due to surface morphology and the presence of nearly saturated surface CO adsorbate coverage.

To understand the role of the defects, e.g. surface morphology, geometric effects related to the facet identity are considered. Defects are associated with the curvature of nanoparticles, which intrinsically contain a number of steps and kinks. The Rh(111) surface will represent an ideal defect-free large nanoparticle catalyst, whereas a stepped Rh(211) surface is used to include the effect of edges. CO chemisorption and surface hydrogen and oxygen dissociative adsorption were analyzed to determinate the most energetically favorable configurations for the initial state

of CO activation. The consistency between the adsorption energies on two modeled surfaces with different unit cell sizes was verified by comparing the CO binding energies on the identical adsorption positions (fcc and hcp sites) on Rh(111) and (111) terrace on Rh(211) surface. Negligible deviations were observed, ranging from 0.02 eV and 0.03 eV for fcc and hcp sites, respectively (TABLE VI). In addition, as expected there is an overestimation in DFT calculated CO adsorption energies relative to the experimental values of 1.65 to 1.43 eV on Rh(111) and 1.65 eV to 1.24 for Rh(100) [113]. However, the trends in adsorption energies with changes in surface facets should be valid as was shown in the experimental work by Efstathiou et al. for CO adsorption on metal clusters present in the supported catalyst [113]. Even when quantitatively different, the trends in adsorption energy of CO were shown to be qualitatively the same, regardless of metal cluster size and relative geometry [113].

TABLE VI
CO ADSORPTION ENERGIES AND BOND DISTANCES

CO chemisorption position		Adsorption Energy (eV)	Bond Distance (Å)	
			C-Rh	C-O
Rh(111)	atop	-1.65	1.86	1.16
	fcc	-1.75	2.13, 2.11, 2.07	1.20
	hcp	-1.90	2.09, 2.09, 2.13	1.19
Rh(211)	atop on step edge	-1.99	1.86	1.16
	fcc on (111) terrace	-1.77	2.11, 2.11, 2.03	1.21
	hcp on (111) terrace	-1.93	2.08, 2.08, 2.08	1.20
	bridge on step edge	-2.09	2.01, 2.01	1.19
	bridge on (100) step	-1.87	2.01, 2.04	1.19
	hollow on (100) step	-1.68	2.15, 2.16	1.21
Rh(211) CO saturated surface	atop step edge	-1.80	1.87	1.16
	fcc on (111) terrace	-1.70	2.12, 2.11, 2.04	1.21
	hcp on (111) terrace	-1.75	2.12, 2.11, 2.05	1.21
	bridge step edge	-2.00	2.01, 2.02	1.18
	bridge on (100) step	-1.80	2.01, 2.01	1.18

Due to the undercoordinated Rh atoms on step edges (the coordination number drops from 9 to 7), a significantly larger CO binding strength is observed for Rh(211) surface relative to Rh(111). Comparing the most favorable adsorption sites between the surfaces shows that step edge contains sites that can increase the CO binding strength by 0.2 eV. The bridge site on the Rh(211) step edge is the preferred CO absorption site (E_{ads} = -2.09 eV) with a 2.01 Å C-Rh bond distance. A similar trend is exhibited for O and C atoms. O preferentially adsorbs 0.24 eV stronger on step edge bridge site when compared to the most favorable Rh(111) hcp site, while C prefers high coordination sites: the 3 fold hollow site for Rh(111) and the hollow site on the (100) step of Rh(211) surface. Increased binding energies on sites containing undercoordinated atoms, is as expected. The coordination number has been shown by Hammer et al. to play a significant role in the reactivity of the surface, such that the undercoordination of atoms results in a shift of the *d*-band center toward the Fermi level causing an increase in the reactivity of the surface [114].

As previously mentioned, CO hydrogenation is performed under high pressure (in excess of 50 bar) causing a near saturation adsorbate coverage [60]. These conditions are modeled by imposing a 0.3 ML CO surface coverage. A decrease in CO adsorption energy is observed on all available sites ranging from 0.1 to 0.3 eV on Rh(111) surface and 0.1 to 0.2 eV on Rh(211) with magnitude correlating to type of site and its proximity to the spectator CO surface species. This implies lateral interaction between surface species that is expected to enhance the mobility of the adsorbates and to have a similar effect on other reaction intermediates.

TABLE VII demonstrates the changes in thermodynamic preferences, induced via surface facet change for CO dissociation, hydrogenation and insertion reactions. All reactions are thermodynamically more preferred on the Rh(211) surface. CO dissociation becomes more

favorable by 0.98 and 0.21 eV for direct and H-assisted mechanism, respectively. This could be associated with an increased stability of the products as the atomic oxygen binding energy (-2.19 eV) increases by 0.15 eV compared to the hcp (111) terrace adsorption, while the atomic carbon binds 0.27 eV stronger to the (100) step hollow site compared to fcc (111) terrace, or 2.03 eV stronger when compared to atop step edge adsorption. It has been suggested by Kapur et al. that the presence of strongly adsorbed CO dissociation products does not block the Rh(211) step sites from participation in subsequent reactions, due to a low hydrogenation barriers to CH_x (~0.6 eV) [112]. Therefore, the driving force of the dissociation reactions is in accord with the observation that the stronger the metal-O interaction, the more likely that CO dissociates [72]. CO dissociation via formyl species becomes exothermic, which correlates with the proposed preference for H-assisted CO dissociation mechanism. The observed preference for the C-C bond formation could be associated with the difference in transition state geometries as compared to C-O dissociation. The transition state for CO dissociation is on the step edge while the insertion reaction is performed on (111) terrace. A 0.32 eV lower CO binding energy is found between the two initial states. A general observation could be postulated that the undercoordinated nature of the surface atoms will create a more reactive surface, while the surface selectivity will be driven by the kinetics of the competing reactions under the operating reaction conditions.

TABLE VII

REACTION ENTHALPIES [a]

	Rh(111)	Rh(211)
$CO \rightarrow C + O$	1.81	0.83
$CO + H \rightarrow HCO$	0.93	0.57
$HCO \rightarrow CH + O$	0.10	-0.11
$HCO + CH \rightarrow CHCHO$	0.61	0.46

[a] Values expressed in eV.

2.3.1 Single Site V Promoted Rh(211) Surface

Vanadium promotion is examined as a single V atom embedded in the Rh(211) step edge and as an oxide (V_6O_{12}) on Rh(111) surface (Figure 20). As previously shown by Reichl et al. variations in reaction conditions will cause vanadium deposited on the metal surface to easily change structure and composition [115]. Under high reduction temperatures (above 1000 K), structure of V atoms diffused in Rh bulk has been shown to exist, while at lower reduction temperatures structures were shown to range from various surface oxide to combinations of surface oxides and subsurface vanadium [115]. Of course, in small nanoparticles the influence of adsorbates may also result in the presence of surface V.

Various V atom promotion sites were examined (Figure 22) with subsurface V calculated to be the most favorable configuration in agreement with the experimental observations of Reichl et al. [115]. A higher surface energy vanadium (3.2 eV/atom) could potentially diffuse into the Rh bulk (2.9 eV/atom) creating a kinetically stable state, therefore remaining metallic. A model of Rh(211) surface with step edge V adatom substitution is chosen (1) as the undercoordinated nature of the surface atom will create a more reactive surface, and (2) to exacerbate the effects of V promotion in an effort to understand how the electronic structure and chemical reactivity of Rh is modified by the formation of bimetallic bonds with V.

TABLE VIII shows the CO binding energies and bond distances for the pristine and 0.3 ML CO covered V step edge promoted Rh(211) surfaces. Upon V step edge substitution, a 0.11 eV increase in the CO binding energy on the atop Rh atom adjacent to V site is observed. This indicates that the presence of V atom on the most reactive surface plane further increases the binding strength on adjacent Rh sites. In contrast, CO adsorption to V containing active sites is decreased by 0.63 eV from atop Rh to atop V and by 0.17 eV from Rh-Rh to Rh-V bridge step-edge sites, indicating a destabilization of surface bound CO. Addition of 0.3 ML CO coverage

increases the CO binding energy for all Rh and V bound surface sites in the range of 0.04 to 0.2 eV.

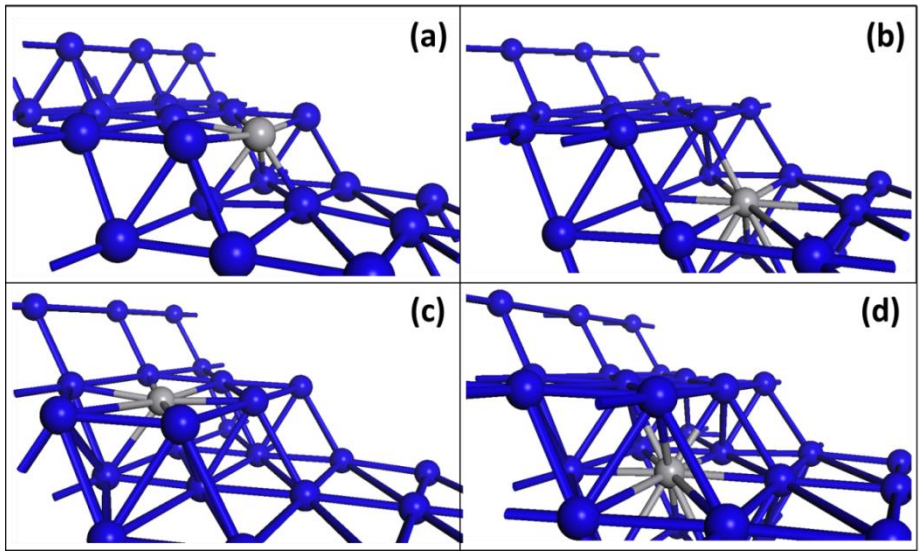

Figure 22. Schematic presentation of V/Rh(211) surface with single atom V substitution at (a) step edge, (b) (100) step, (c) (111) terrace and (d) sublayer.

TABLE VIII
SELECTED CO ADSORPTION ENERGIES AND BOND DISTANCES

CO chemisorption position		Adsorption Energy (eV)	Bond Distances (Å)		
			C-Rh	C-O	C-V
V/Rh(211)	atop V step edge	-1.36	-	1.16	2.00
	atop Rh step edge	-2.10	1.85	1.17	-
	Rh-V bridge step edge	-1.92	1.87	1.17	2.51
	Rh-V bridge (100) step	-1.64	2.10	1.19	2.06
	Rh-Rh bridge (100) step	-1.88	2.00, 2.05	1.19	-
	hcp bellow V (111) terrace	-1.90	2.07, 2.09, 2.10	1.20	-
	hcp (111) terrace	-1.97	2.08, 2.07, 2.08	1.20	-
	fcc (111) terrace	-1.81	2.12, 2.11, 2.04	1.21	-
V/Rh(211) CO saturated surface	atop V step edge	-1.32	-	1.15	2.05
	atop Rh step edge	-1.90	1.88	1.16	-
	Rh-V bridge step edge	-1.89	1.87	1.17	2.61
	Rh-V bridge (100) step	-1.52	2.13	1.18	2.03
	Rh-Rh bridge (100) step	-1.81	2.00, 2.01	1.19	-
	hcp bellow V (111) terrace	-1.68	2.08, 2.03, 2.22	1.20	-
	hcp (111) terrace	-1.78	2.06, 2.12, 2.12	1.20	-
	fcc (111) terrace	-1.70	2.18, 2.08, 2.03	1.22	-

V induced shifts in surface reactivity/selectivity are further analyzed by calculating the reaction enthalpies and activation barriers for our model reactions on V containing active sites. As with the unpromoted Rh(211) catalyst, transition state structures for dissociation reactions involve species bound to the step edge such that undercoordinated metal atoms stabilize the geometries (Figure 23). A 0.11 and 0.28 eV decrease in CO binding energy is observed on the step edge and (100) step, respectively upon substitution of Rh-Rh to Rh-V site, indicating destabilization of the CO due to V promotion. This is manifested in substantial activation barrier of 1.93 eV (ΔE = 0.23 eV) for direct CO dissociation to atomic C and O. CO hydrogenation becomes the preferred CO activation mechanism with substantially lower barriers for HCO and COH formation (0.76 and 0.90 eV, respectively). Preference for HCO vs. COH formation could be attributed to the change in transition state site from the step edge for HCO to (111) terrace for COH. V adatom sites could prevent site blocking due to strongly bound atomic C and O products of the direct CO dissociation, present on unpromoted Rh surface. However, the direct CO dissociation is still expected to be dominant on the step sites not affected by V atom promotion.

Subsequent C-O bond dissociation via step edge bound formyl intermediate (C-O bond length 1.27 Å) is inhibited with a further increase in reaction barrier to 3.04 eV (Figure 24). COH bound to a less reactive (111) terrace has a comparatively lower dissociation barrier of 1.38 eV (ΔE = - 0.37 eV). Formyl hydrogenation to formaldehyde (CH_2O) becomes favored with a significantly lower barrier of 0.48 eV (ΔE = 0.72 eV) while the hydrogenation to CHOH is endothermic and higher by 1.05 eV. Formaldehyde is expected to be a stable surface species (E_{ads} = - 2.18 eV) able to participate in subsequent reactions. Upon hydrogenation to CH_2OH the C-O bond distance has been elongated to 1.46 Å facilitating dissociation to CH_2 + OH with a 0.83 eV barrier (ΔE = - 0.12 eV). If however, CH_2OH is further hydrogenated to methanol

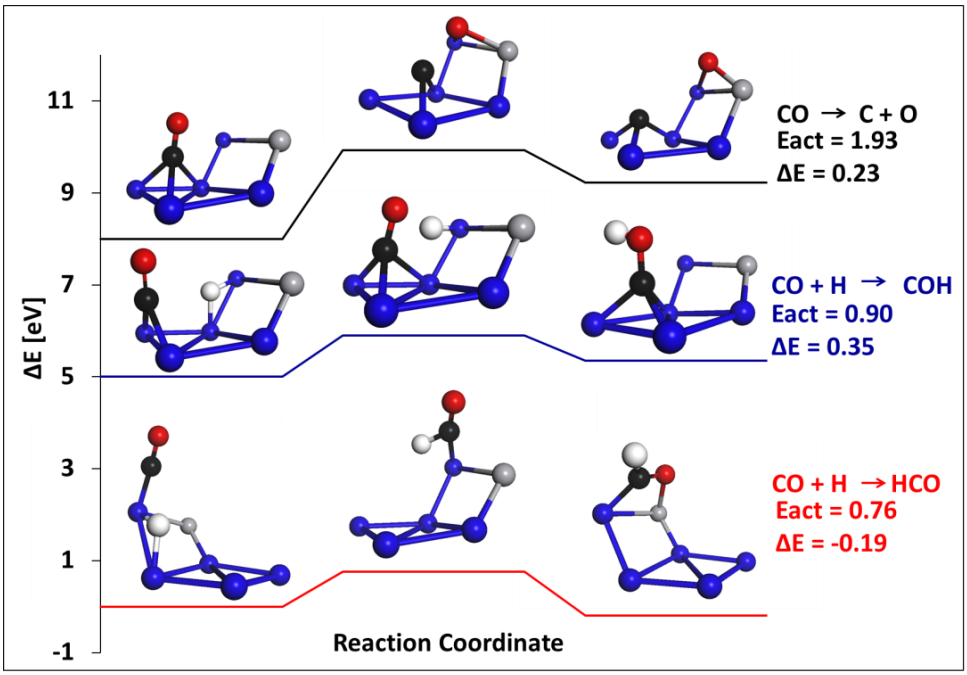

Figure 23. Potential energy diagram and corresponding schematic presentation (section of the step edge) of calculated initial, transition and final states for HCO activation on 0.3 ML CO saturated V/Rh(211) surface. Colors representation: Rh (blue), V (gray), O (red), C (black) and H (white).

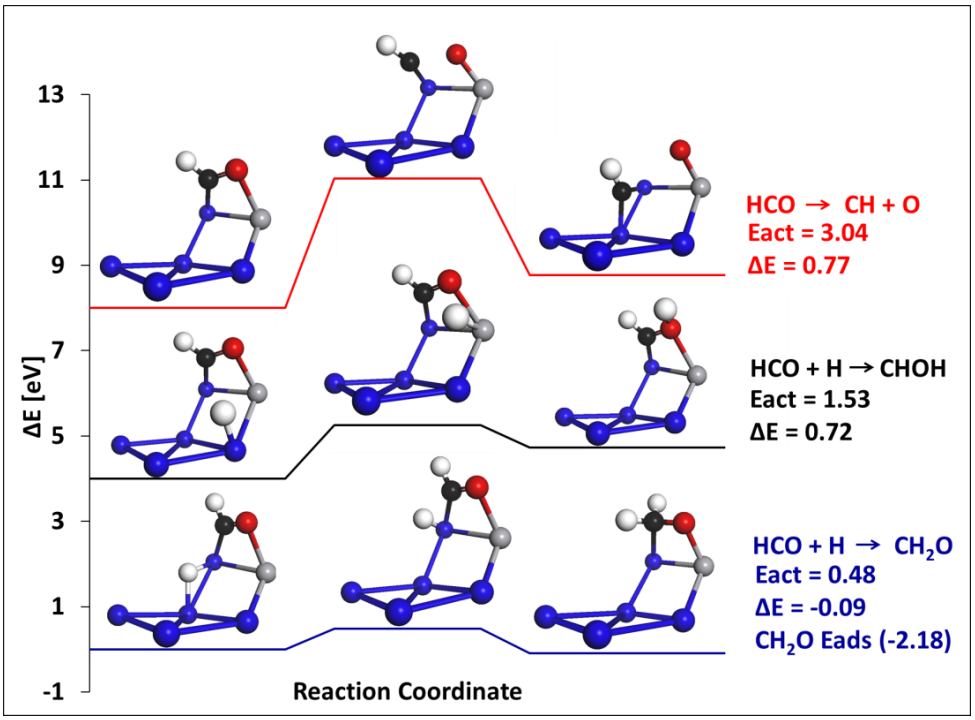

Figure 24. Potential energy diagram and corresponding schematic presentation (section of the step edge) of calculated initial, transition and final states for HCO activation on 0.3 ML CO saturated V/Rh(211) surface.

(CH_3OH) its binding energy decreases to -1.40 eV, indicating a species that under these reaction conditions could potentially be desorbed.

As previously mentioned, the selectivity of the unpromoted Rh surface has been extensively analyzed, most recently by Kapur et al. determining the barriers for CO insertion into CH_x on Rh(211) surface to be 1.0, 0.94 and 1.31 eV for x = 1, 2 and 3 respectively, with the lowest reaction enthalpy (0.12 eV) for CH_3 insertion [112]. The most significant effect of single atom V promotion can be observed in HCO insertion into CH_x reactions, which are highly exothermic with very low reaction barriers (Figure 25). In addition, V promotion provides for a more favorable CO insertion into CH_x (ΔE = 0.02, -0.62 and -1.83 eV for CH_x with x = 1, 2 and 3, respectively) vs CH_x hydrogenation reactions (ΔE = 0.40, -0.45 and -0.32 eV for CH_x with x = 1, 2 and 3, respectively). These observations indicate that V promotion could decrease the selectivity to methane and methanol by lowering the barrier to C-C insertion.

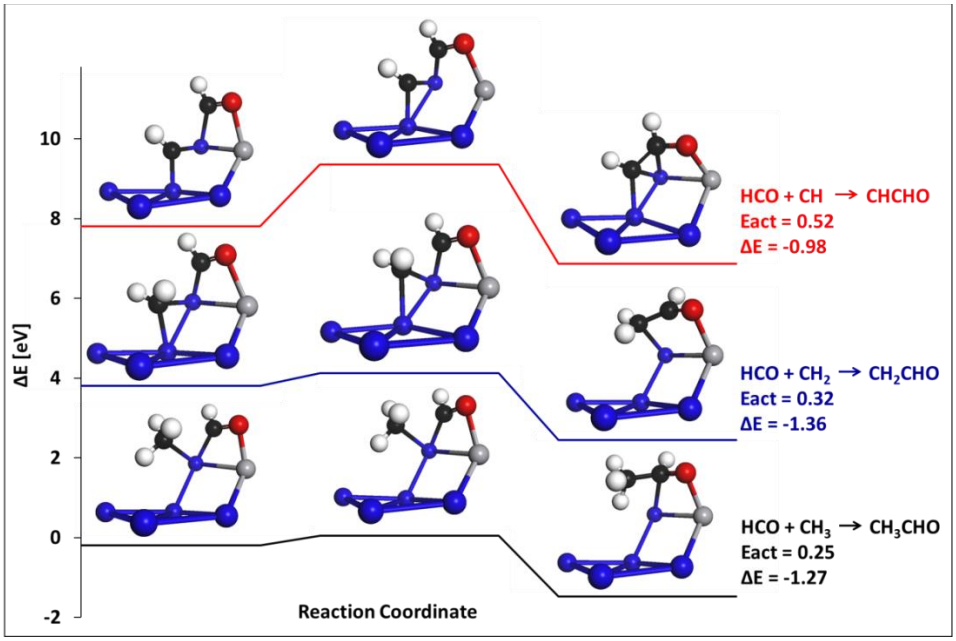

Figure 25. Potential energy diagram and corresponding schematic presentation (section of the step edge) of calculated initial, transition and final states for HCO insertion on 0.3 ML CO saturated V/Rh(211) surface.

The removal of oxygen from the system is expected to proceed via H_2O formation and its subsequent desorption. From the potential energy diagram for H_2O formation (Figure 26) it can be seen that initially O is bound to a V-Rh step edge bridges site (E_{ads} = -2.99 eV, V-O bond distance: 1.69 Å), while H preferentially adsorbs on the Rh (100) step with a -0.37 eV adsorption energy. OH formation is exothermic (E_{act} = 0.91 eV). However, subsequent hydrogenation to H_2O is 0.40 eV uphill with 1.18 eV barrier. Atop V bound H_2O has a 0.66 eV stronger binding to the promoted surface (E_{ads} = -1.2 eV) compared to a non-promoted surface (where no V is present) implying a more stable surface species. Under the high T and P syngas conversion conditions, the calculated barriers for H_2O formation would be in an acceptable range to turn over the catalytic sites proposed for the system. In addition, water gas shift ($CO + H_2O \rightarrow CO_2 + H_2$) is a side reaction that is always present during a syngas conversion to alcohols and therefore some oxygen is effectively converted to CO_2 [60].

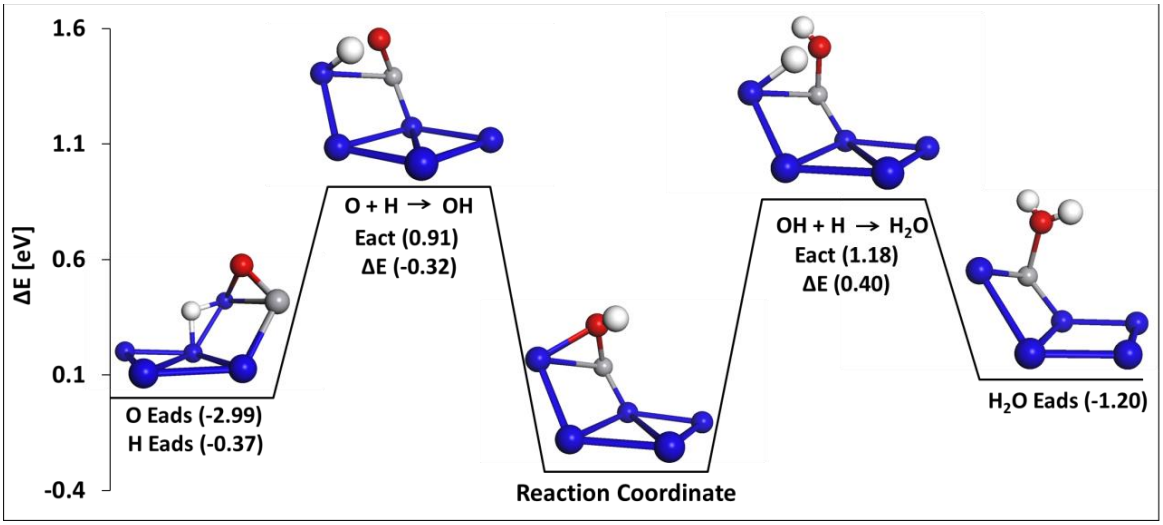

Figure 26. Potential energy diagram and corresponding schematic presentation (section of the step edge) of calculated initial, transition and final states for H_2O formation on 0.3 ML CO saturated V/Rh(211) surface.

The effect of the metallic V promotion on Rh(211) surface can be correlated to the electronic structure changes associated with the active metal's *d*-band filling. Electronic interactions were analyzed by observing the changes to the simulated partial density of states (PDOS) for Rh and V *d*-band in Rh, V and V alloyed Rh bulk (Figure 27). For the Rh *d*-band there is an increase in available *d*-states above the Fermi level and a shift in *d*-band center from -2.02 to -1.90 eV upon alloying. In contrast, V *d*-PDOS shows a significant decrease in the *d*-band center upon alloying (from 1.54 eV to 0.27 eV). In addition, the Bader charge analysis [108] was performed and it was determined that a 0.65 e of charge is transferred from each adjacent Rh to V in the RhV structure correlating to the observed *d*-band center shifts. A combined 1.95 e charge transfer to V atom from all adjacent Rh's is manifested as a visible depletion of available V *d*-states above the Fermi level as filled states now exist below the Fermi level. This shift is evident in the weakly V bound CO (1.32 eV) as well as in a significant decrease in CO biding energy on Rh-V bridge (100) step (-1.52 eV) relative to Rh-Rh bridge (100) step (-1.81 eV). The small change in the *d*-band center of Rh compared to V can be explained in terms of ratio of V to Rh atoms (1:3), which would imply an even smaller effect on Rh within the structure of the technical catalyst (which should have a much lower V loadings).

The small upward shift in the *d*-band center of Rh correlates to the observed increase in Rh bound CO adsorption energy upon V promotion (TABLE VIII). This implies that the metallic V promotion creates more reactive Rh sites necessary for C-O bond breaking reactions while at the same time providing low binding sites on V and adjacent Rh-V bridge sites that could provide a path for hydrogenation and insertion reactions. Vanadium's higher surface energy is likely to create alloys containing subsurface V atoms that further decrease CO binding strength on surface Rh atoms. This type of surface may further inhibit CO dissociation on highly reactive

step edges, hence increasing a probability for hydrogenation and/or C-C bond formation reactions.

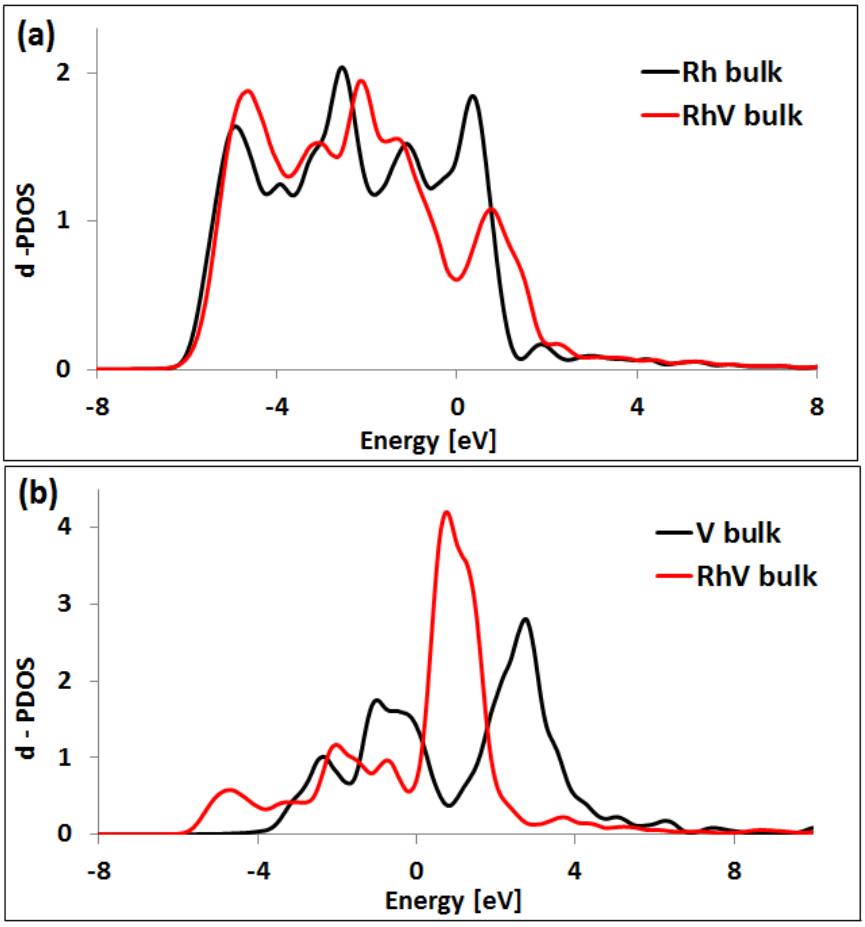

Figure 27. Simulated (a) Rh *d*-PDOS and (b) V *d*-PDOS

2.3.2 V_6O_{12} Promoted Rh(111) Surface

The metal-oxide interface promotion was analyzed based on a structure of the VO_x cluster supported on Rh(111), developed by Schoiswohl et al.[101]. V_6O_{12} promotion is modeled with an undercoordinated V site formed by an oxygen vacancy, assumed to be achieved upon the oxygen removal via desorption of H_2O molecule. As such, the structure would be thermodynamically driven towards regeneration, creating a highly reactive site for CO

dissociation. The presence of 0.3 ML CO surface coverage will affect biding energies of the reactants and reaction intermediates, which are independent of the metal-oxide interface. The metal-oxide interface shows negligible changes in CO adsorption behavior due to CO coverage, as CO does not adsorb on the oxide.

The metal-oxide interface promoted CO activation is induced on sites next to oxygen vacancy. It results in a tilted CO adsorption, in which C is bonded to the surface Rh and O to the undercoordinated V atom (Figure 28). This position is 0.3 eV more stable than the CO adsorption on a three-fold hollow site on Rh(111) and results in lengthening of the CO bond from 1.19 Å to 1.28 Å. The increase in the bond length destabilizes the interface bound CO* (* indicates adsorption into the oxygen vacancy) and facilitates hydrogenation to HCO* with a 0.89 eV lower barrier than that of CO* dissociation (E_{act} = 1.61 eV) and 0.56 eV lower barrier than interface independent CO hydrogenation on Rh(111) surface. This type of interaction between the promoter phase and CO has been experimentally observed by Ichikawa et al. on a Mn promoted Rh catalyst. Using IR spectroscopy, they identified a characteristic band at 1650 cm^{-1} that was ascribed to the Mn oxide bound acetyl (CH_3CO) intermediate, formed by CO insertion onto the surface hydrocarbons and stabilized due to manganese oxide [100].

Formation of a HCO* intermediate further elongates the C-O bond distance to 1.33 Å and facilitates subsequent exothermic dissociation (ΔE = - 0.58 eV) to CH + O* with a reaction barrier of 0.49 eV (Figure 29). Formyl hydrogenation to hydroxycarbene (CHOH) and formaldehyde (CH_2O) are both essentially thermoneutral with reaction barriers of 1.12 and 0.54 eV, respectively. Unpromoted Rh(111) surface binds formaldehyde weakly (ΔE = -0.69 eV) allowing for facile desorption, whereas the binding energy of interface bound CH_2O is -1.52 eV, indicating a stable surface intermediate. Dissociation of the CH_2O* into O* + CH_2 is an

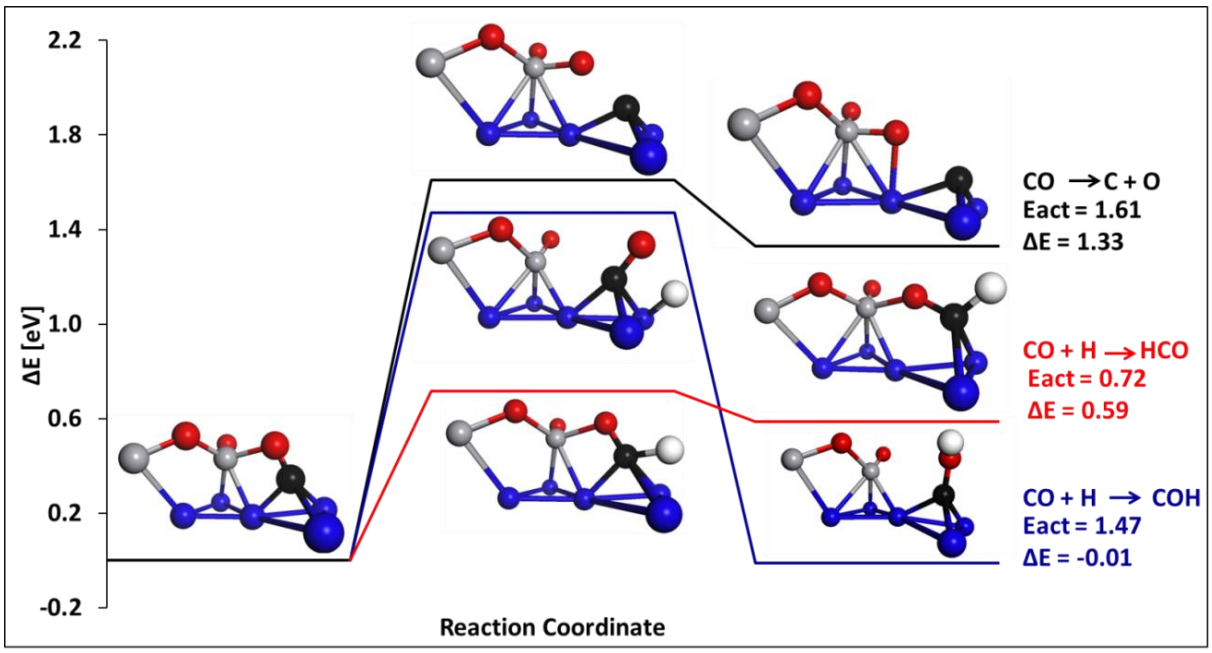

Figure 28. Potential energy diagram and corresponding schematic presentation of calculated initial, transition and final states for CO activation on V_6O_{12}/Rh(111) interface. Abbreviations representation: ΔE (reaction enthalpy) and E_{act} (activation energy).

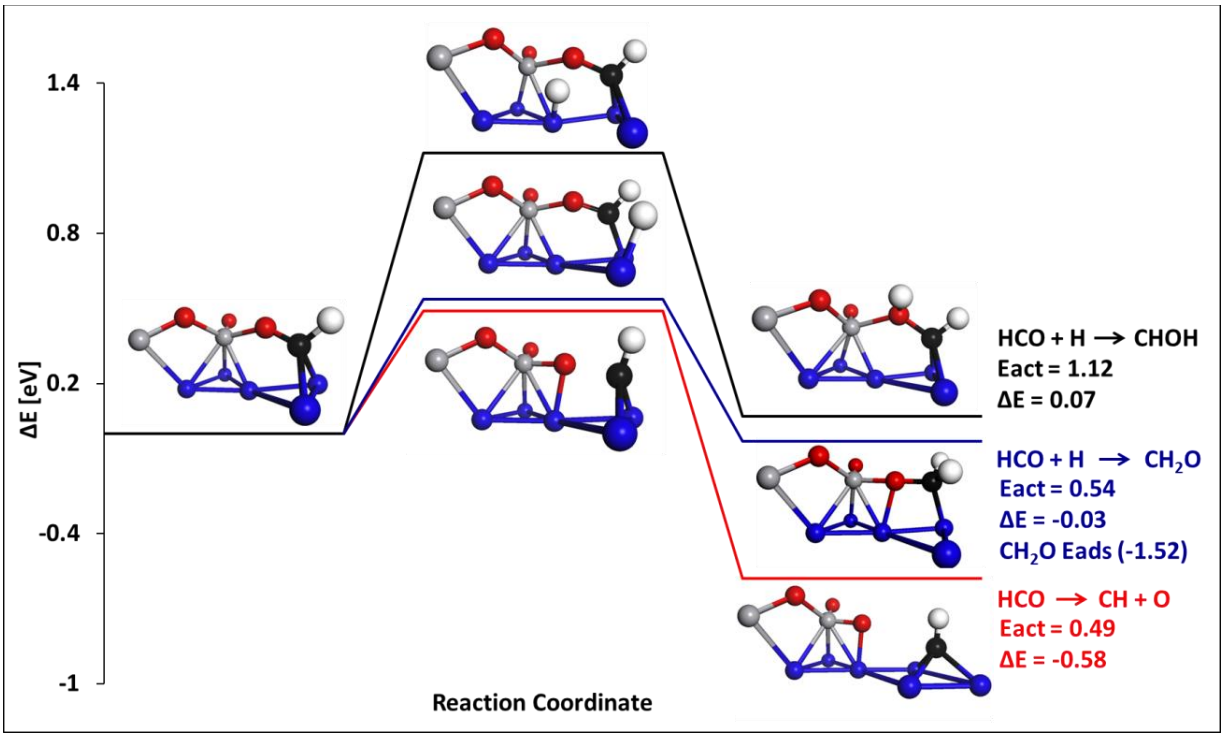

Figure 29. Potential energy diagram and corresponding schematic presentation of calculated initial, transition and final states for HCO activation on V_6O_{12}/Rh(111) interface.

exothermic process (ΔE= -0.44 eV) with a 0.68 eV reaction barrier, which is comparatively similar to HCO* dissociation. As can be seen, preferential hydrogenation of C vs O site on the interface bound species is observed, with high reaction barriers for both CHOH* and COH* formation. However, if formed, subsequent dissociation of these species is decidedly favorable compared to further hydrogenation. CHOH* dissociation to CH + OH* is highly exothermic (ΔE = - 1.20 eV) with a 0.18 eV reaction barrier, while COH* dissociation barrier is 0.53 eV (ΔE = 0.27 eV). Regardless of the intermediate formed, the H-assisted CO dissociation mechanism is preferred.

Upon C-O bond dissociation, subsequent CH_x hydrogenation or C-C bond formation appears to be completely independent of interface (i.e. does not involve the VOx cluster). As the HCO insertion mechanism was shown to be both thermodynamically and kinetically preferred on Rh(111) surface relative to CO insertion [85], herein the effect of CO surface coverage on HCO insertion is analyzed. Analogous to CO insertion [85], an increase in exothermicity is observed with a more hydrogenated CH_x species (ΔE = -0.16, -0.44 and -0.66 eV for CH, CH_2 and CH_3, respectively) . HCO insertion into CH has the lowest activation barrier (E_{act} = 0.76 eV) which increases to 1.01 and 1.44 eV for CH_2 and CH_3 insertion.

O* or OH* created after interface promoted CO bond dissociation is assumed to be hydrogenated to H_2O which may subsequently desorb to regenerate the undercoordinated V (or O vacancy) reaction site. From the potential energy diagram for H_2O formation (Figure 30) it can be seen that O bound to an undercoordinated V atom has a very high adsorption energy (E_{ads}= -3.39 eV), while H preferentially adsorbs on the Rh bridge site (E_{ads}= -0.22 eV). O* hydrogenation to OH* is exothermic with a 0.75 eV activation barrier. Subsequent hydrogenation to H_2O* is 0.30 eV uphill (E_{act} = 0.83 eV). The presence of the oxide interface

increases the H_2O* binding strength (E_{ads} = -1.10 eV) by 0.61 eV compared to unpromoted Rh(111) surface. However, under the T and P required for syngas conversion, the calculated barriers would be in an acceptable range to turn over the catalytic sites proposed for the system.

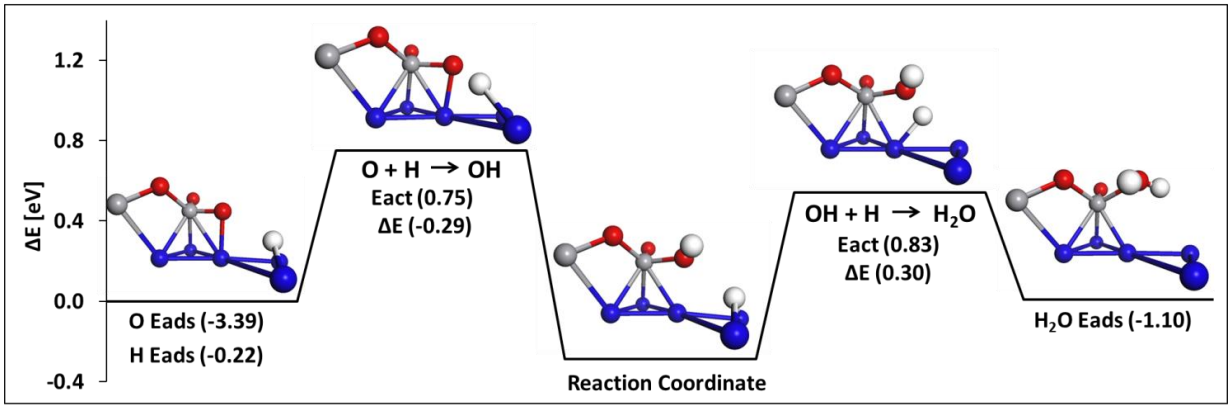

Figure 30. Potential energy diagram and corresponding schematic presentation of calculated initial, transition and final states for H_2O formation on V_6O_{12}/Rh(111) interface.

As the proposed mechanism implies a promotion mechanism via V_6O_{12}/Rh(111) interface sites, Bader charge analysis [108] was utilized to calculate electron charge distribution on all atoms for supported VO_x clusters and all relevant reaction intermediates. Formal charges for V in the surface oxide were determined via interpolations of known charges for reference bulk oxides with a range of V oxidation states from +2 in VO bulk to +5 in V_2O_5 bulk (TABLE IX). As shown by Shapovalov et al. DFT calculated net charge of V atom does not change significantly regardless of VO_x cluster and, as such, deviates substantially from the formal oxidation states [116]. While these values cannot constitute a quantitative measure, they are, in general, correct indicators of the trends in surface reactivity. Formal oxidation states of +2.4 and +3.1 for the V_6O_{11} and V_6O_{12} clusters are predicted. The calculated charges indicate a more reduced surface oxide relative to bulk oxides in the proposed promoter models. This is not surprising, given that

the oxide layers are in direct contact with the Rh(111) surface and the Rh effectively reduces the V.

TABLE IX
NET CHARGES AND FORMAL OXIDATION STATES [a]

	Net charges	Formal oxidation states
VO bulk	+1.71	+2.0
V_6O_{11}/Rh(111)	+1.87	+2.4
V_2O_3 bulk	+2.07	+3.0
V_6O_{12}/Rh(111)	+2.09	+3.1
VO_2 bulk	+2.33	+4.0
V_2O_5 bulk	+2.43	+5.0

[a] Values determined with Bader charge analysis method.

Further Bader charge analysis was performed to obtain an electronic charge on all relevant atoms at metal-oxide interface with O vacancy and with interface bound reaction intermediates (Figure 31). The positive charge indicates the amount of electron charge lost when the atom becomes a part of the adsorbed compound, while negative charge correlates to electron charge gained in the process. A negative charge on the surface of the Rh atoms in contact with oxide and the positive charge on V atoms indicates that some electron charge density is being transferred from V to Rh surface (a continuous electron distribution of a metallic surface). The charge on the V atoms remains fairly consistent (+2.01 to +2.09 e) in the presence of peripheral O; small changes could be attributed to the charge redistribution in presence of various reaction intermediated. However, with O vacancy a 0.22 e charge increase on V atom is observed (+1.87 e). Neighboring atoms undergo small changes in charge density indicating that the reaction mechanism effects more than just the atoms involved in bond braking/making steps.

Since the charge does not always correlate to the electron affinity or to electronegative of the atoms, the most charged site does not necessarily imply the most reactive site [117]. This is observed as the most ionic part of the V_6O_{12}/Rh(111) surface (Figure 31a), the bridging O is least reactive and a highly unfavorable adsorption site for gas phase CO. In consequence, its charge remains constant (-1.09 e) during all reaction steps and its bond length to V shows insensitivity to the change in the nature of interface bound intermediate (TABLE X). As the reaction intermediates are bound via O atom to a peripheral vacancy (Figure 31e-h), significant variations in V-O* bond lengths (TABLE X) are observed corresponding to the nature of the intermediate. As such, a V-O*-Rh site causes the cationic fragments of intermediates to interact with Rh and anionic fragments to interact with V. Oxygen bonded to both Rh and V interface atoms (e.g. O* in V_6O_{12} or $V_6O_{11} – CH_2O$) creates an electron deficient Rh, which upon formation of vacancy in V_6O_{11} becomes electron rich (-0.15 e). In consequence, 0.22 e charge increase is observed for the undercoordinated V atom. A similar trend is observed for all other intermediates, with a distinction of a smaller amount of charge transfer to Rh atom.

TABLE X
BOND LENGTHS FOR SELECTED INTERFACE BOUND REACTION INTERMEDIATES [a]

	V-bridging O	V-peripherally bound O in reaction intermediates	Peripheral bound O-C in reaction intermediates
V_6O_{11}	1.79	-	-
V_6O_{12}	1.79	1.70	-
V_6O_{11}-H_2O	1.78	2.05	-
V_6O_{11}-CO	1.77	1.99	1.28
V_6O_{11}-HCO	1.78	1.89	1.34
V_6O_{11}-CHOH	1.78	2.08	1.49
V_6O_{11}-CH_2O	1.77	1.85	1.40
V_6O_{11}-CH_2OH	1.79	2.09	1.48

[a] Values expressed in Å.

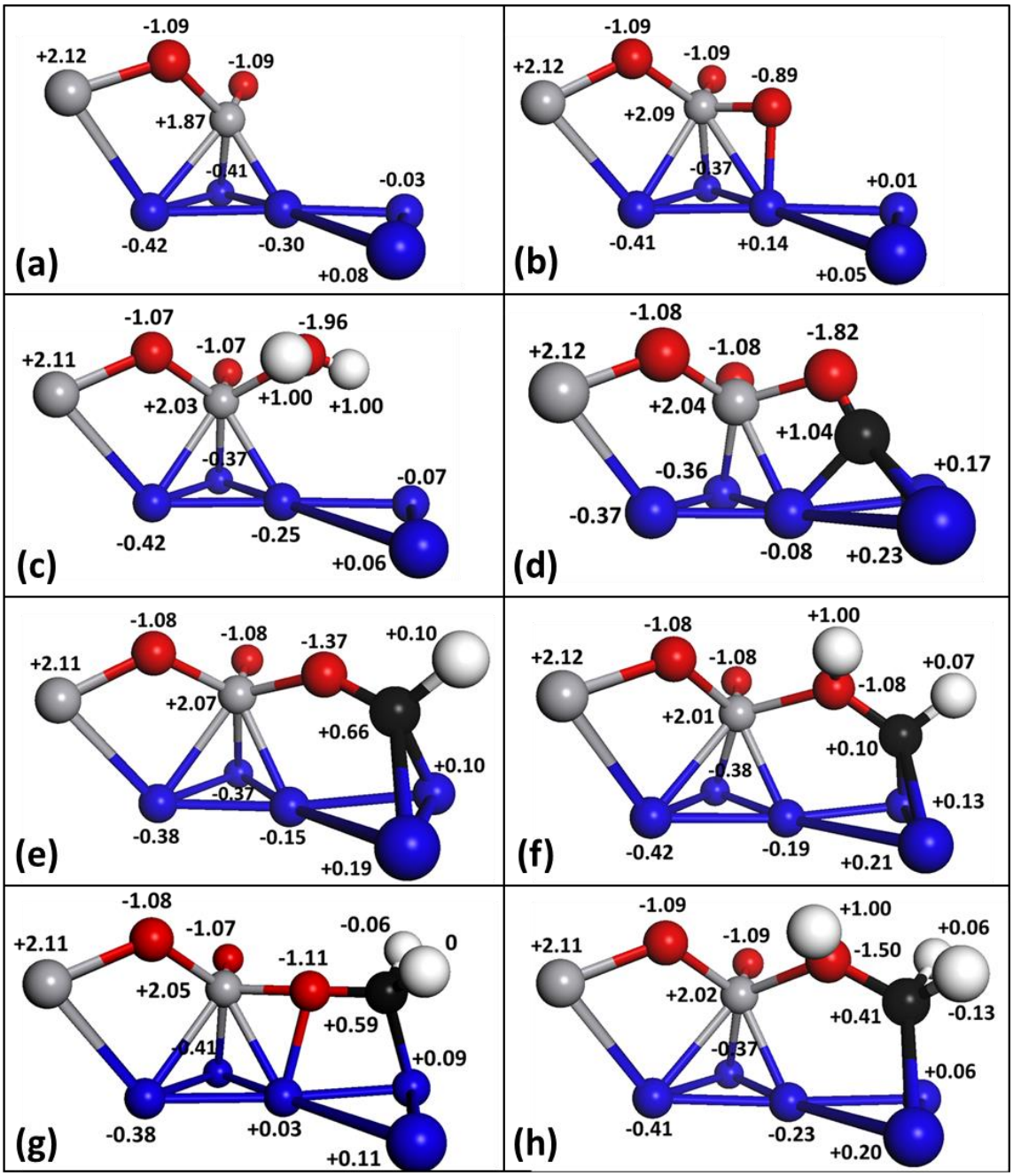

Figure 31. Schematic representation of the Bader charges [e] on (a) V_6O_{11}/Rh(111) interface, (b) V_6O_{12}/Rh(111) interface, and V_6O_{11}/Rh(111) interface bound (c) H_2O, (d) CO, (e) HCO, (f) CHOH, (g) CH_2O and (h) CH_2OH intermediate.

V_6O_{12} promoted Rh(111) surface is an example of a bifunctional catalyst, where the presence of both elements (V and Rh) changes what oxidation states are cycled through. The proposed reduction/oxidation mechanism (Figure 32) is based on the interface bound CO dissociation, which occurs due to an availability of the electropositive V atom (V^{3+}) and O vacancy. CO will act as a source of oxygen, via diffusion and adsorption into the O vacancy site on metal-oxide interface. Consistent with the adsorption is a decrease in electron density on both V and Rh by 0.17 and 0.22 e, respectively. Adsorption of CO into the vacancy site results in an increase in the C-O bond length, which facilitates CO hydrogenation to formyl or some higher intermediate. Formation of HCO* corresponds to a charge transfer from O to Rh and a further elongation of C-O bond from 1.28 to 1.34 Å. Formyl (or other interface bound carbonyl species) dissociation is highly favored, enabling an H-assisted CO dissociation, and results in a change in the formal oxidation state of V to V^{4+}. V^{3+} can be reformed via reduction following O* or OH* hydrogenation to H_2O* and its subsequent desorption. Hydrogenation of O* to H_2O* causes a transfer of charge from H to O, increasing O-V bond length and facilitating H_2O desorption. It is evident that in the presence of a strong electron-withdrawing group such as O or OH, an electron is more likely to be located on O atom than on V or Rh. This type of promotion should be applicable to any experimentally observed surface VO_x. Herein, V^{3+}/V^{4+} model is revealed. However, V^{4+}/V^{5+} or V^{2+}/V^{3+} model is just as probable; as it is the combination of V and a metal surface that gives access to this type of redox cycle.

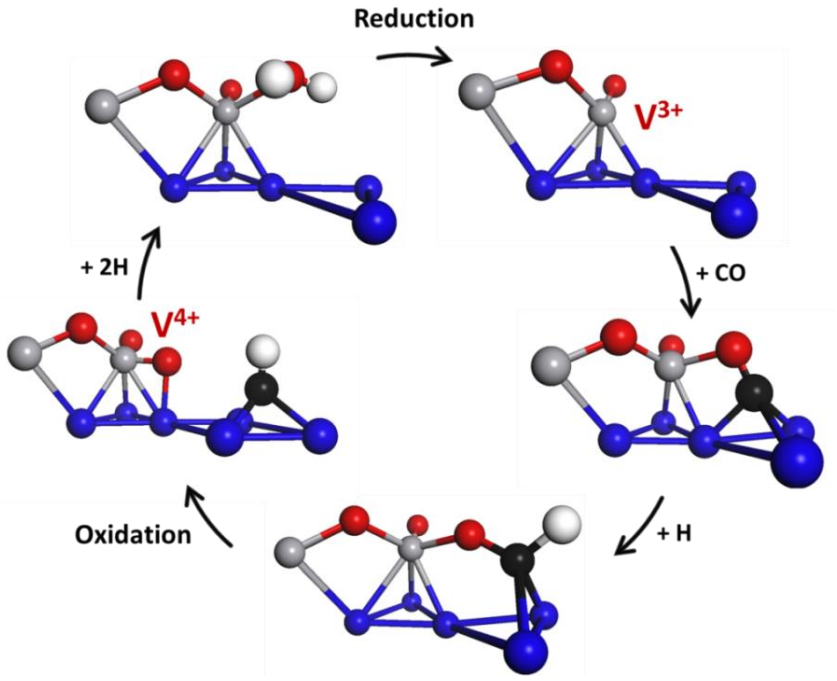

Figure 32. Schematic presentation of the V^{3+}/V^{4+}oxidation/reduction mechanism for H-assisted CO dissociation on V_6O_{12}/Rh(111) interface.

2.4 Conclusion

It was found that the presence of V, both as an alloying element and as an oxide, under the high CO adsorbate coverage present under the syngas conversation conditions should enhance the H-assisted CO dissociation mechanism. Metallic V promotion will induce a charge transferred from each adjacent Rh to V in the RhV structure, creating a more reactive Rh sites necessary for C-O bond breaking reactions while at the same time providing low energy binding sites on V and adjacent Rh-V bridge sites that could provide a path for hydrogenation and insertion reactions. Vanadium's higher surface energy is likely to create alloys containing subsurface V atoms that further decrease CO binding strength on surface Rh atoms. This type of surface may further inhibit CO dissociation on highly reactive step edges, hence increasing a probability for hydrogenation and/or C-C bond formation reactions.

V promotion of Rh(111) surface via surface oxide clusters (V_6O_{12}) is an example of a bifunctional catalyst, where the presence of both elements (V and Rh) is necessary for the proposed V^{3+}/V^{4+} oxidation/reduction cycle. CO adsorbed into an oxygen "vacancy" can be dissociated following hydrogenation by the favorable formation of CH. CO surface coverage decreases CO adsorption energies on all Rh(111) sites, the magnitude correlating to type of site and its proximity to the spectator CO surface species while the metal-oxide interface shows negligible changes as CO does not adsorb on the oxide. Formation of C-H and C-C bond is independent of the interface and will take place on metal. As such, the reaction energetics will be affected by CO surface coverage.

VITA

NAME: Ruzica Todorovic

EDUCATION: Ph.D., Chemical Engineering, University of Illinois at Chicago
Chicago, Illinois, 2016

M.S., Chemical Engineering, University of Illinois at Chicago
Chicago, Illinois, 2011

B.S., Chemical Engineering, University of Illinois at Chicago
Chicago, Illinois, 2010

PRESENTATIONS: AIChE Annual Meeting, Atlanta, GA, 2014.
Chicago Catalysis Club Spring Symposium, Naperville, IL, 2014.

Catalysis Club Spring Symposium, Naperville, IL, 2010.

20th Annual Argonne Symposium for Undergraduates in Science, Engineering and Mathematics, Lemont, IL, 2009.

AIChE Chicago Section Meeting, Chicago, IL, 2010.

PROFESSIONAL American Institute of Chemical Engineers (AIChE)

MEMBERSHIP: Catalysis Club of Chicago (CCC)

North American Catalysis Society (NACS)

PUBLICATIONS: R. Todorovic, "Hydrogen Storage Technologies for Transportation Application". Journal of Undergraduate Research 5 (2015) 1.

R. Tao, R. Todorovic, J. Liu, R.J. Meyer, A. Arnold, W. Walkosz, P. Zapol, A. Romanenko, L. D. Cooley and R. F. Klie, "Electron Energy Loss Spectroscopy Study of Metallic Nb and Nb Oxides". *Journal of Applied Physics* **110** (2011) 124313.

R. Todorovic, R. J. Meyer. A Comparative Density Function Theory Study of the Direct Synthesis of H_2O_2 on Pd, Pt and Au Surfaces. Catalysis Today, 160 (2011) 242-248.

R. Todorovic, P. Aich, J. T. Miller, C. L. Marshall, A. J. Kropf, R. J. Meyer, "An Examination of the Role of the Single-Atom Alloy Pd Promoted Ag Catalyst for Selective Hydrogenation of Acrolein", In preparation.

R. Todorovic and R.J. Meyer, “DFT Study of the Role of the Promoter in V-promoted Rh Catalysts for CO Hydrogenation”, In preparation.

P. Aich, R. Todorovic, H. Wei, J. T. Miller, C. L. Marshall, R. J. Meyer, “Effect of Support Reducibility on the Selective Hydrogenation of Acrolein”, In preparation.

CITED LITERATURE

[1] A. Bendounan, H. Cercellier, Y. Fagot-Revurat, B. Kierren, V.Y. Yurov, D. Malterre, Interplay Between Surface and Electronic Structures in Epitaxial Ag Ultra Thin Films on Cu(111), Appl. Surf. Sci., 212 (2003) 33-37.

[2] A.M. Rodríguez, G. Bozzolo, J. Ferrante, Multilayer Relaxation and Surface Energies of fcc and bcc Metals using Equivalent Crystal Theory, Surf. Sci., 289 (1993) 100-126.

[3] V. Ponec, Active Centres for Synthesis Gas Reactions, Catal. Today, 12 (1992) 227-254.

[4] P. Maki-Arvela, J. Hajek, T. Salmi, D.Y. Murzin, Chemoselective Hydrogenation of Carbonyl Compounds over Heterogeneous Catalysts, Appl. Cataly., A: General, 292 (2005) 1-49.

[5] M.L. Toebesa, F.F. Prinsloob, J.H. Bittera, A.J.v. Dillena, K.P.d. Jonga, Influence of Oxygen-Containing Surface Groups on the Activity and Selectivity of Carbon Nanofiber-Supported Ruthenium Catalysts in the Hydrogenation of Cinnamaldehyde, J. Catal., 214 (2003) 78-87.

[6] P. Reyes, H. Rojas, G. Pecchi, J.L.G. Fierro, Liquid-Phase Hydrogenation of Citral Over Ir-Supported Catalysts, J. Mol. Catal. A: Chem., 179 (2002) 293-299.

[7] U.K. Singh, M.A. Vannice, Liquid-Phase Citral Hydrogenation over SiO_2-Supported Group VIII Metals, J. Catal., 199 (2001) 73-84.

[8] P. Reyes, M.C. Aguirre, I. Melián-Cabrera, M. López Granados, J.L.G. Fierro, Interfacial Properties of an Ir/TiO_2 System and Their Relevance in Crotonaldehyde Hydrogenation, J. Catal., 208 (2002) 229-237.

[9] J.P. Breen, R. Burch, J. Gomez-Lopez, K. Griffin, M. Hayes, Steric effects in the selective hydrogenation of cinnamaldehyde to cinnamyl alcohol using an Ir/C catalyst, Appl. Cataly., A: General, 268 (2004) 267-274.

[10] M. Bron, D. Teschner, A. Knop-Gericke, F.C. Jentoft, J. Krohnert, J. Hohmeyer, C. Volckmar, B. Steinhauer, R. Schlogl, P. Claus, Silver as acrolein hydrogenation catalyst: intricate effects of catalyst nature and reactant partial pressures, PCCP, 9 (2007) 3559-3569.

[11] M. Bron , D. Teschner, A. Knop-Gericke, B. Steinhauer, A. Scheybal, M. Havecker, D. Wang, R. Fodisch, D. Honicke, A. Wootsch, R. Schlogl, P. Claus, Bridging the Pressure and Materials Gap: In-depth Characterisation and Reaction Studies of Silver-Catalysed Acrolein Hydrogenation, J. Catal., 234 (2005) 37-47.

[12] H. Wei, C. Gomez, N. Guo, T. Wu, R.J. Lobo-Lapidus, J. Miller, R.J. Meyer, Selective Hydrogenation of Acrolein on Supported Silver Catalysts: A Kinetics Study of Particle Size Effects, J. Catal., 298 (2012) 18-26.

[13] H. Backman, J. Jensén, F. Klingstedt, J. Wärnå, T. Salmi, D.Y. Murzin, Kinetics and Modeling of H_2/D_2 Exchange over Ag/Al_2O_3, Appl. Cataly., A: General, 273 (2004) 303-307.

[14] P. Claus, Selective Hydrogenation of ά,β-unsaturated Aldehydes and other C=O and C=C Bonds Containing Compounds, Top. Catal., 5 (1998) 51-62.

[15] S. Fujii, N. Osaka, M. Akita, K. Itoh, Infrared Reflection Absorption Spectroscopic Study on the Adsorption Structures of Acrolein on an Evaporated Silver Film, The Journal of Physical Chemistry, 99 (1995) 6994-7001.

[16] M. Bron, D. Teschner, A. Knop-Gericke, A. Scheybal, B. Steinhauer, M. Havecker, R. Fodisch, D. Honicke, R. Schlogl, P. Claus, In situ-XAS and Catalytic Study of Acrolein Hydrogenation over Silver Catalyst: Control of Intramolecular Selectivity by the Pressure, Catal. Commun., 6 (2005) 371-374.

[17] R.A. Van Santen, Complementary Structure Sensitive and Insensitive Catalytic Relationships, Acc. Chem. Res., 42 (2009) 57-66.

[18] D. Uzio, G. Berhault, Factors Governing the Catalytic Reactivity of Metallic Nanoparticles, Catalysis Reviews, 52 (2010) 106-131.

[19] U.K. Singh, M.N. Sysak, M.A. Vannice, Liquid-Phase Hydrogenation of Citral over Pt/SiO_2 Catalysts: II. Hydrogenation of Reaction Intermediate Compounds, J. Catal., 191 (200) 181-191.

[20] K.H. Lim, A.B. Mohammad, I.V. Yudanov, K.M. Neyman, M. Bron, P. Claus, N. Rosch, Mechanism of Selective Hydrogenation of α, β–Unsaturated Aldehydes on Silver Catalysts: A Density Functional Study, J. Phys. Chem. C, 113 (2009) 13231-13240.
[21] R. Kramer, M. Andre, Adsorption of Atomic Hydrogen on Alumina by Hydrogen Spillover, J. Catal., 58 (1979) 287-295.
[22] P. Maki-Arvela, L.-P. Tiainen, A.K. Neyestanaki, R. Sjoholm, T.-K. Rantakyla, E. Laine, T. Salmi, D.Y. Murzin, Liquid Phase Hydrogenation of Citral: Suppression of Side Reactions, Appl. Catal., A, 237 (2002) 181-200.
[23] J. Rodriguez, Physical and Chemical Properties of Bimetallic Surfaces, Surf. Sci. Rep., 24 (1996) 223-287.
[24] V. Ponec, Alloy Catalysts: the Concepts, Appl. Cataly., A: General, 222 (2001) 31-45.
[25] M. English, A. Jentys, J.A. Lercher,
Structure Sensitivity of the Hydrogenation of Crotonaldehyde over Pt/SiO_2 and Pt/TiO_2, J. Catal., 166 (1996) 25.
[26] H. Yan, H. Cheng, H. Yi, Y. Lin, T. Yao, C. Wang, J. Li, S. Wwi, J. Lu, Single-Atom Pd_1/Graphene Catalyst Achieved by Atomic Layer Deposition: Remarkable Performance in Selective Hydrogenation of 1,3-Butadine, J. Am. Chem. Soc., 137 (2015) 10484-10487.
[27] I.J. Shannon, T. Maschmeyer, R.D. Oldroyd, G. Sankar, J.M. Thomas, H. Pernot, J.-P. Balikdjian, M. Che, Metallocene-Derived, Isolated MoVI Active Centres on Mesoporous Silica for the Catalytic Dehydrogenation of Methanol, J. Chem. Soc., Faraday Trans., 94 (1998) 1495-1499.
[28] G. Kyriakou, M.B. Boucher, A.D. Jewell, E.A. Lewis, T.J. Lawton, A.E. Baber, H.L. Tierney, M. Flytzani-Stephanopoulos, E.C.H. Sykes, Isolated Metal Atom Geometries as a Strategy for Selective Heterogeneous Hydrogenations, Science, 335 (2012) 1209-1212.
[29] H.L. Tierney, A.E. Baber, E.C.H. Sykes, Atomic-Scale Imaging and Electronic Structure Determination of Catalytic Sites on Pd/Cu Near Surface Alloys, Journal of Physical Chemistry C, 113 (2009) 7246-7250.
[30] A.E. Baber, H.L. Tierney, T.J. Lawton, E.C.H. Sykes, An Atomic-Scale View of Palladium Alloys and their Ability to Dissociate Molecular Hydrogen, ChemCatChem, 3 (2011) 607-614.
[31] H.L. Tierney, A.E. Baber, J.R. Kitchin, E.C.H. Sykes, Hydrogen Dissociation and Spillover on Individual Isolated Palladium Atoms, Physicall Review Letters, 103 (2009) 2461021-2461024.
[32] P. Aich, H. Wei, B. Basan, A.J. Kropf, N.M. Schweitzer, C.L. Marshall, J.T. Miller, R.J. Meyer, Single Atom Alloy Pd-Ag Catalysts for Selective Hydrogenation of Acrolein, J. Phys. Chem. C, 119 (2015) 18140−18148.
[33] M.A. Vannice, B. Sen, Metal-Support Effects on the Intramolecular Selectivity of Crotonaldehyde Hydrogenation Over Platinum, J. Catal., 115 (1989) 65-78.
[34] M.A. Vannice, The Influence of MSI (Metal–Support Interactions) on Activity and Selectivity in the Hydrogenation of Aldehydes and Ketones, Top. Catal., 4 (1997) 241-248.
[35] P. Claus, S. Schimpf, R. Schödel, P. Kraak, W. Mörke, D. Hönicke, Hydrogenation of crotonaldehyde on Pt/TiO_2 catalysts: Influence of the phase composition of titania on activity and intramolecular selectivity, Appl. Cataly., A: General, 165 (1997) 429-441.
[36] J.R. Regalbuto, Strong Electrostatic Adsorption of Metals onto Catalyst Supports, in: Handbook of Catalyst Preparation, 2006, pp. 297-318.
[37] J. Jaklevic, J.A. Kirby, M.P. Klein, A.S. Robertson, G.S. Brown, P. Eisenberger, Fluorescence Detection of EXFS: Sensitivity Enhancement for Dilute Species and Thin Films, Solid State Communications, 23 (1977) 679-682.
[38] J.A. Kropf, J.R. Finch, A.J. Fortner, S. Aase, C. Karanfil, U.C. Segre, J. Terry, G. Bunker, D.L. Chapman, On a Bent Silicon Crystal in the Laue Geometry to Resolve X-ray Fluorescence for X-ray absorption Spectroscoy, Rev. Sci. Instrum., 74 (2003).
[39] Y. Lei, J. Jelic, L.C. Nitsche, J. Miller, R.J. Meyer, Effect of Particle Size and Adsorbates on the L3, L2 and L1 X-ray Absorption Near Edge Structure of Supported Pt Nanoparticles, Top. Catal., 54 (2011) 334.

[40] D. Childers, An Exploration of Geometric and Electronic Effects in Metal Nanoparticle Catalysts, in: Chemical Engineering, University of Illinois at Chicago, Ann Arbor, 2014, pp. 181.
[41] K. Tamaru, Dynamic Heterogeneous Catalysis Academic Press, New York, 1978.
[42] J.B. Butt, Reaction Kinetics and Reactor Design, Dekker, New York, 200.
[43] N.A. Bhore, M.T. Klein, K.B. Bischoff, The Delplot Technique: A New Method for Reaction Pathway Analysis, Industrial & Engineering Chemistry Research, 29 (1990) 313-316.
[44] L. Petrov, Problems and Challenges About Accelerated Testing of the Catalytic Activity of Catalysts, in: NATO Science Series II Mathematics, Physics and Chemistry 2002.
[45] G. Kresse, J. Furthmuller, Efficiency of Ab-initio Total Energy Calculations for Metals and Semiconductors Using a Plane-wave Basis Set, Comput. Mater. Sci., 6 (1996) 15-50.
[46] G. Kresse, J. Furthmuller, Efficient Iterative Schemes for Ab-initio Total-Energy Calculations Using a Plane-Wave Basis Set, Phys. Rev. B, 54 (1996) 11169-11186.
[47] J.P. Perdew, Y. Wang, Accurate and Simple Analytic Representation of the Electron-Gas Correlation-Energy, Phys. Rev. B, 45 (1992) 13244-13249.
[48] H.J. Monkhorst, J.D. Pack, Special Points for Brillonin-Zone Integrations, Phys. Rev. B, 13 (1976) 5188-5192.
[49] M. Bron, D. Teschner, A. Knop-Gericke, F.C. Jentoft, J. Krohnert, J. Hohmeyer, C. Volckmar, B. Steinhauer, R. Schlogl, P. Claus, Silver as Acrolein Hydrogenation Catalyst: Intricate Effects of Catalyst Nature and Reactant partial Pressures, Phys. Chem. Chem. Phys., 9 (2007) 3559-3569.
[50] N. Schweitzer, H. Xin, E. Nikolla, S. Linic, T.J. Miller, Establishing Relationships Between the Geometric Structure and Chemical Reactivity of Alloy Catalysts Based on their Measured Electronic Structure, Top. Catal., 53 (2010) 348−356.
[51] P. Reyes, G. Pecchi, J.L.G. Fierro, Surface Structures of Rh−Cu Sol−Gel Catalysts and Performance for Crotonaldehyde Hydrogenation, Langmuir, 17 (2001) 522-527.
[52] R. Mélendrez, G. Del Angel, V. Bertin, M.A. Valenzuela, J. Barbier, Selective Hydrogenation of Carvone and o-xylene on Pd–Cu Catalysts Prepared by Surface Redox Reaction, J. Mol. Catal. A: Chem., 157 (2000) 143-149.
[53] L. Zhou, R.J. Madix, Strong Structure Sensitivity in the Partial Oxidation of Styrene on Silver Single Crystals, Surf. Sci., 603 (2009) 1751-1755.
[54] S. Lögdberg, M. Lualdi, S. Järås, J.C. Walmsley, E.A. Blekkan, E. Rytter, A. Holmen, On the Selectivity of Cobalt-Based Fischer–Tropsch Catalysts: Evidence for a Common Precursor for Methane and Long-Chain Hydrocarbons, J. Catal., 274 (2010) 84-98.
[55] J.P. Den Breejen, J.R.A. Sietsma, H. Friedrich, H.J. Bitter, K.P. de Jong, Design of Supported Cobalt Catalysts with Maximum Activity for the Fischer–Tropsch Synthesis, J. Catal., 270 (2010) 146–152.
[56] S.C. Chuang, J.G. Goodwin Jr, I. Wender, Investigation by Ethylene Addition of Alkali Promotion of CO Hydrogenation on $RhTiO_2$, J. Catal., 92 (1985) 416-421.
[57] C.H. Bartholomew, R.B. Pannell, J.L. Butler, Support and Crystallite Size Effects in CO Hydrogenation on Nickel, J. Catal., 65 (1980) 335-347.
[58] Y. Soong, K. Krishna, P. Biloen, Catalyst Aging Studied with Isotopic Transients: Methanation over Raney Nickel, J. Catal., 97 (1986) 330-343.
[59] L. Guczi, Chapter 8: Effect of Hydrogen in Controlling Co Hydrogenation, Stud. Surf. Sci. Catal., 64 (1991) 350.
[60] V. Subramani, S.K. Gangwal, A Review of Recent Literature to Search for an Efficient Catalytic Process for the Conversion of Syngas to Ethanol, Energy & Fuels, 22 (2008) 814-839.
[61] M. Voith, Chemical and Engineering News, in, 2010.
[62] P. Sabatier, La Catalyse en Chimie Organique, (1920).
[63] S.S.C. Chuang, J. Stevens, R. W., R. Khatri, Mechanism of C_{2+} Oxygenate Synthesis on Rh Catalysts, Top. Catal., 32 (2005) 225-232.
[64] N.D. Subramanian, J. Gao, X. Mao, J.G. Goodwin Jr, W. Torres, J.J. Spivey, La and/or V Oxide Promoted Rh/SiO_2 Catalysts: Effect of Temperature, H_2/CO Ratio, Space Velocity, and Pressure on Ethanol Selectivity from Syngas, J. Catal., 272 (2010) 204-209.

[65] T.P. Wilson, P.H. Kasai, P.C. Ellgen, The State of Manganese Promoter in Rhodium-Silica Gel Catalysts, J. Catal., 69 (1981) 193-201.
[66] M.M. Bhasin, W.J. Bartely, P.C. Ellgen, Synthesis Gas Conversion Over Supported Rhodium and Rhodium-Iron Catalysts, J. Catal., 54 (1978) 120-128.
[67] F. Fischer, H. Tropsch, Reduction and Hydrogenation of Carbon Monoxide, Brennstoff- Chemi, 7 (1926) 97-104.
[68] P. Liu, Y.M. Choi, Mechanism of Ethanol Synthesis from Syngas on Rh(111), J. Amer. Chem. Soc., 131 (2009) 13054-13061.
[69] M. Mavrikakis, M. Baumer, H.J. Freund, J.K. Norskov, Structure Sensitivity of CO Dissociation on Rh Surfaces, Catal. Lett., 81 (2002) 153-156.
[70] D. Mei, R. Rousseau, S.M. Kathmann, V.A. Glezakou, M.H. Engelhard, W. Jiang, C. Wang, M.A. Gerber, J.F. White, D.J. Stevens, Ethanol Synthesis from Syngas Over Rh-based/SiO_2 Catalysts: A Combined Experimental and Theoretical Modeling Study, J. Catal., 271 (2010) 325-342.
[71] W. Schultz, B.E. Dale, D. Pimentel, The Cost of Biofuels: A Debate on Ethanol, Chem. Eng. News, 85 (2007) 12-16.
[72] J.J. Spivey, A. Egbebi, Heterogeneous Catalytic Synthesis of Ethanol from Biomass-derived Syngas, Chem. Soc. Rev., 36 (2007) 1514-1528.
[73] M.A. Vannice, Catalytic Synthesis of Hydrocarbons from H_2-CO Mixtures over Group-8 Metals .1. Specific Activities and Product Distributions of Supported Metals, J. Catal., 37 (1975) 449-461.
[74] S.R. Craxford, On the Mechanism of the Fischer-Tropsch Reaction, Trans. Farad. Soc., 42 (1946) 576-580.
[75] H. Pichler, H. Schulz, Recent Findings in the Field of Synthesis of Hydrocarbons from CO and H_2, Chem. Ing. Tech., 42 (1970) 1162-1174.
[76] A. Kladi, X.E. Verykios, Z.L. Zhang, Surface Species Formed During CO and CO_2 Hydrogenation over Rh/TiO_2 (W6+) Catalysts Investigated by FTIR and Mass-Spectroscopy, J. Catal., 156 (1995) 37-50.
[77] I.A. Fisher, A.T. Bell, A Comparative Study of CO and CO_2 Hydrogenation over Rh/SiO_2, J. Catal., 162 (1996) 54-65.
[78] D.M. Ren, W. Liu, A Study of Chemisorption Behavior of Carbon Monoxide on Rhodium Surfaces, Surf. Sci., 232 (1990) 316-322.
[79] W. Liu, D.M. Ren, The Surface Structure Effect on the Chemisorption of CO on Rh, Surf. Sci., 232 (1990) 323-328.
[80] B.T. Loveless, C. Buda, M. Neurock, E. Iglesia, CO Chemisorption and Dissociation at High Coverages During CO Hydrogenation on Ru Catalysts, J. Amer. Chem. Soc., 135 (2013) 6107-6121.
[81] M. Zhuo, A. Borgna, M. Saeys, Effect of the CO Coverage on the Fischer–Tropsch Synthesis Mechanism on Cobalt Catalysts, J. Catal., 297 (2013) 217-226.
[82] M. Ojeda, R. Nabar, Milekar, A.U., A. Ishikawa, M. Mavrikakis, E. Iglesia, CO Activation Pathways and the Mechanism of Fischer–Tropsch Synthesis, J. Catal., 277 (2010) 287-297.
[83] O.R. Inderwildi, S.J. Jenkins, D.A. King, Fischer-Tropsch Mechanism Revisited: Alternative Pathways for the Production of Higher Hydrocarbons from Synthesis Gas, J. Phys. Chem. C, 112 (2008) 1305-1307.
[84] S. Eckle, H. Anfang, R.J. Behm, Reaction Intermediates and Side Products in the Methanation of CO and CO_2 over Supported Ru Catalysts in H_2-Rich Reformate Gases, J. Phys. Chem. C, 115 (2011) 1361-1367.
[85] Y.H. Zhao, K. Sun, X. Ma, J. Liu, D. Sun, H.Y. Su, Carbon Chain Growth by Formyl Insertion on Rhodium and Cobalt Catalysts in Syngas Converstion, Angew. Chem., 50 (2011) 5335-5338.
[86] M. Ichikawa, W.M.H. Sachtler, Catalytic Site Requirements for Elementary Steps in Syngas Conversion to Oxygenates over Promoted Rhodium, J. Phys. Chem., 90 (1986) 4752–4758.
[87] F. Li, D. Jing, X.C. Zeng, Z. Chen, Mn Monoleyer Modified Rh for Syngas-to-Ethanol Conversion: A First-Principles Study, Nanoscale, 4 (2012) 1123-1129.
[88] J. Gao, X. Mo, J.G. Goodwin, La, V and Fe Promotion of Rh/SiO_2 for CO Hydrogenation: Detailed Analysis of Kinetics and Mechanism, J. Catal., 268 (2009) 142-149.

[89] M. Ichikawa, K. Shikakura, M. Kawai, Heterogeneous Catalysis Related to Energy Problems, in: Proceedings of Symposium, Dalian, China, 1982.
[90] V. Ponec, Chapter 4, Selectivity in the Syngas Reactions: The Role of Supports and Promoters in the Activation of Co and in the Stabilization of Intermediates, Stud. Surf. Sci. Catal., 64 (1991) 117-157.
[91] T. Beutel, O.S. Alekseev, Y.A. Ryndin, V.A. Likholobov, H. Knözinger, FTIR Spectroscopic Study and CO Hydrogenation on V, Nb, and Ta Oxide Promoted Rh/SiO_2 Catalysts, J. Catal., 169 (1997) 132-142.
[92] H.Y. Luo, H.W. Zhou, L.W. Lin, B.D. Liang, Q. Xin, Q. Xin, Role of Vanadium Promoter in $Rh-V/SiO_2$ Catalysts for the Synthesis of C_2-Oxygenates from Syngas, J. Catal., 145 (1994) 232-234.
[93] A. Marimuthu, J. Zhang, S. Linic, Tuning Selectivity in Propylene Epoxidation by Plasmon Mediated Photo-Switching of Cu Oxidation State, Science, 339 (2013) 1590-1593.
[94] Y. Zhai, D. Pierre, R. Si, W. Deng, P. Ferrin, A.U. Nilekar, G. Peng, J.A. Herron, D.C. Bell, H. Saltsburg, M. Mavrikakis, M.F. Stephanopoulos, Alkali-Stabilized Pt-OHx Species Catalyze Low-Temperature Water-Gas Shift Reactions, Sci., 329 (2010) 1633-1636.
[95] C. Kuang-Hsiu , P. Ying-Chih , C. Kao-Der , L. Yi-Fan , L. Chia-Ming, Y. Jien-Wei , S. Han-C. , J. Yung, Ag-Nanoparticle-Decorated SiO_2 Nanospheres Exhibiting Remarkable Plasmon-Mediated Photocatalytic Properties, J. Phys. Chem. C, 116 (2012) 19039–19045.
[96] S. Linic, P. Christopher, H. Xin, A. Marimuthu, Catalytic and Photocatalytic Transformations on Metal Nanoparticles with Targeted Geometric and Plasmonic Properties, Acc. Chem. Res., 46 (2013) 1890–1899.
[97] S. Linic, M.A. Barteau, On the Mechanism of Cs Promotion in Ethylene Epoxidation on Ag, J. Am. Chem. Soc., 126 (2004) 8086-8087.
[98] M.E. Levin, M. Salmeron, A.T. Bell, G.A. Somorjai, The Enhancement of CO Hydrogenation on Rhodium by TiO, Overlayers J. Catal., 106 (1987) 401-409.
[99] A.B. Boffa, A.T. Bell, G.A. Somorjai, Vanadium Oxide Deposited on an Rh Foil: CO and CO_2 Hydrogenation Reactivity, J. Catal., 139 (1993) 602-610.
[100] T. Fukushima, H. Arakawa, M. Ichikawa, High-pressure IR Spectroscopic Evidence of Acetyl and Acetate Species Directly Formed in $CO-H_2$ Converstion on SiO_2-Supported Rh and Rh-Mn Catalysts, J. Chem. Soc., Chem. Commun., (1985) 729-731.
[101] J. Schoiswohl, G. Surney, S. Surnev, M. Sock, M.G. Ramsey, F.P. Netzer, Planar Vanadium Oxide Clusters: Two-Dimensional Evaporation and Diffusion on Rh(111), Phys. Rev. Lett., 92 (2004) 206103-206106.
[102] J. Schoiswohl, M. Sock, S. Eck, S. Surnev, M.G. Ramsey, F.P. Netzer, Atomic-level Growth Study of Vanadium Oxide Nanostructures on Rh(111), Phys. Rev. B, 69 (2004) 155403-155413.
[103] J. Schoiswohl , S. Eck , M.G. Ramsey , J.N. Andersen , S. Surnev , F.P. Netzer Vanadium Oxide Nanostructures on Rh(111): Promotion Effect of CO Adsorption and Oxidation, Surf. Sci., 580 (2005) 122-136.
[104] B.J. Kip, P.A.T. Smeets, J.H.M.C. van Wolput, H.W. Zandbergen, Preparation and Characterization of Vanadium Oxide Promoted Rhodium Catalysts, Appl. Catal., 33 (1987) 157-180.
[105] B.J. Kip, E.G.F. Hermans, R. Prins, Carbon Monoxide Hydrogenation Over Alkali-promoted Rh/Al_2O_3, $Rh/V_2O_3/SiO_2$ and $Rh/TiO_2/SiO_2$, Appl. Catal., 35 (1987) 141-152.
[106] P. Gronchi, E. Tempesti, C. Mazzocchia, Metal Dispersion Dependent Selectivities for Syngas Conversion to Ethanol on V_20_3 Supported Rhodium, Appl. Catal., A, 120 (1994) 115-126.
[107] T. Mori, A. Miyamoto, N. Takahashi, M. Fukagaya, T. Hattori, Y. Murakami, Promotion Effects of Vanadium, Niobium, Molybdenum, Tungsten, and Rhenium Oxides on Surface Reactions in the CO Hydrogenation over Ru/Al_2O_3 Catalyst, J. Phys. Chem., 90 (1986) 5197-5201.
[108] G. Henkelman, A. Arnaldsson, H. Jonsson, A fast and robust algorithm for Bader decomposition of charge density, Comput. Mater. Sci., 36 (2006) 254-360.
[109] V. Milman, K. Refson, S.J. Clark, C.J. Pickard, J.R. Yates, S.P. Gao, P.J. Hasnip, M.I.J. Probert, A. Perlov, M.D. Segall, Electron and Vibrational Spectroscopies Using DFT, Plane Waves and Pseudopotentials: CASTEP Implementation, J. Mol. Struct. THEOCHEM, 954 (2010) 22-36.

[110] S.E. Mason, I. Grinberg, A.M. Rappe, First-Principles Extrapolation Method for Accurate CO Adsorption Energies on Metal Surfaces, Phys. Rev. B, 69 (2004) 161401-161404.
[111] G. Henkelman, B.P. Uberuaga, H. Jonsson, A Climbing Image Nudged Elastic Band Method for Finding Saddle Points and Minimum Energy Paths, J. Chem. Phys., 113 (2000) 9901-9904.
[112] N. Kapur, J. Hyun, B. Shan, J.B. Nicholas, K. Cho, Ab Initio Study of CO Hydrogenation to Oxygenates on Reduced Rh Terraces and Stepped Surfaces, J. Phys. Chem. C, 114 (2010) 10171–10182.
[113] C.D. Zeinalipour-Yazdi, A.L. Cooksy, A.M. Efstathiou, CO adsorption on transition metal clusters: Trends from density functional theory, Surf. Sci., 602 (2008) 1858–1862.
[114] B. Hammer, O.H. Nielsen, J.K. Norskov, Structure Sensitivity in Adsorption: CO Interaction with Stepped and Reconstructed Pt Surfaces, Catal. Lett., 46 (1997) 31-35.
[115] W. Reichl, K. Hayek, Vanadium Oxide Overlayers on Rhodium: Influence of the Reduction Temperature on the Composition and on the Promoting Effect in CO Hydrogenation, J. Catal., 208 (2002) 422-434.
[116] V. Shapovalov, H. Metiu, VOx (x = 1-4) Submonolayers Supported on Rutile TiO_2(110) and CeO_2(111) Surfaces: The Structure, the Charge of the Atoms, the XPS Spectrum, and the Equilibrium Composition in the Presence of Oxygen, J. Phys. Chem. C, 111 (2007) 14179-14188.
[117] M. Calatayud, A. Markovits, C. Minot, Electron-Count Control on Adsorption upon Reducible and Irreducible Clean Metal-Oxide Surfaces, Catal. Today, 89 (2004) 269-278.

APPENDIX

TABLE XI

LIST OF POSSIBLE ELEMENTARY REACTIONS AND CORRESPONDING RATES OF REACTIONS FOR HYDROGENATION OF ACROLEIN [a, b]

Elementary reaction	Reaction rate expressions
$AC + * \overset{K_{AC}}{\longleftrightarrow} AC^*$	$r_{AC} = k_{AC}\left[P_{AC}\theta^* - \frac{\theta_{AC}}{K_{AC}}\right]$
$H_2 + 2* \overset{K_{H_2}}{\longleftrightarrow} 2H^*$	$r_{H_2} = k_{H_2}\left[P_{H_2}\theta^{*^2} - \frac{\theta_H^2}{K_{H_2}}\right]$
$AA^* \overset{K_{AA}}{\longleftrightarrow} AA + *$	$r_{AA} = k_{AA}[\theta_{AA} - K_{AA}P_{AA}\theta^*]$
$PA^* \overset{K_{PA}}{\longleftrightarrow} PA + *$	$r_{PA} = k_{PA}[\theta_{PA} - K_{PA}P_{PA}\theta^*]$
$1\text{–}P^* \overset{K_{1-P}}{\longleftrightarrow} 1\text{–}P + *$	$r_{1-P} = k_{1-P}[\theta_{1-P} - K_{1-P}P_{1-P}\theta^*]$
$P^* \overset{K_P}{\longleftrightarrow} P + *$	$r_P = k_P[\theta_P - K_P P_P \theta^*]$
$AC^* + H^* \overset{K_{11}}{\longleftrightarrow} HA^* + *$	$r_{11} = k_{11}\left[\theta_{AC}\theta_H - \frac{\theta_{HA}\theta^*}{K_{11}}\right]$
$HA^* + H^* \overset{K_{12}}{\longleftrightarrow} AA^* + *$	$r_{12} = k_{12}\left[\theta_{HA}\theta_H - \frac{\theta_{AA}\theta^*}{K_{12}}\right]$
$AC^* + H^* \overset{K_{21}}{\longleftrightarrow} F^* + *$	$r_{21} = k_{21}\left[\theta_{AC}\theta_H - \frac{\theta_F\theta^*}{K_{21}}\right]$
$F^* + H^* \overset{K_{22}}{\longleftrightarrow} PA^* + *$	$r_{22} = k_{22}\left[\theta_F\theta_H - \frac{\theta_{PA}\theta^*}{K_{22}}\right]$
$AA^* \overset{k_3}{\longrightarrow} PA^*$	$r_3 = k_3\left[\theta_{AA} - \frac{\theta_{PA}}{K_3}\right]$
$AA^* + 2H^* \overset{K_4}{\longleftrightarrow} P^* + H_2O + 2*$	$r_4 = k_4\theta_{AA}\theta_H$
[c] $AA^* + 2H^* \overset{K_5}{\longleftrightarrow} 1\text{–}P^* + 2*$	$r_5 = k_5\theta_{AA}\theta_H^2$
[c] $PA^* + 2H^* \overset{K_6}{\longleftrightarrow} 1\text{–}P^* + 2*$	$r_6 = k_6\theta_{PA}\theta_H$

[a] Surface bound species is indicated with *

[b] Notation for reaction species: acrolein (AC), allyl alcohol (AA), propionaldehyde (PA), hydroxyallyl (HA), n-formylethyl (F), 1-propanol (1-P) and propene (P).

[c] Reactions 12 to 14 are not necessarily elementary reactions.

DERIVATION OF RATE EXPRESSIONS FOR COMPETITIVE ADSORPTION MODEL

Hydrogenation of Acrolein to Form Allyl Alcohol via Hydroxyallyl Intermediate

$$H_2 + 2* \overset{K_{H_2}}{\longleftrightarrow} 2H^*$$

$$AC + * \overset{K_{AC}}{\longleftrightarrow} AC^*$$

$$AC^* + H^* \overset{K_1}{\longleftrightarrow} HA^* + *$$

$$HA^* + H^* \overset{K_2}{\longleftrightarrow} AA^* + *$$

$$AA^* \overset{K_{AA}}{\longleftrightarrow} AA + *$$

(1) H_2 adsorption as the rate-limiting step

$$r = k_{H_2} P_{H_2} \theta^{*2}$$

Expressions for fractional coverages are as follows:

- Dissociative hydrogen adsorption

$$\theta_H = \left(\frac{K_{AA} P_{AA}}{K_1 K_2 K_{AC} P_{AC}}\right)^{1/2} \theta^*$$

- Molecular acrolein adsorption

$$\theta_{AC} = K_{AC} P_{AC} \theta^*$$

- Hydroxyallyl reaction intermediate

$$\theta_{HA} = \left(\frac{K_1 K_{AC} P_{AC} K_{AA} P_{AA}}{K_2}\right)^{1/2} \theta^*$$

- Allyl alcohol desorption

$$\theta_{AA} = K_{AA} P_{AA} \theta^*$$

From the site balance we obtain

$$\theta^* = \frac{1}{1 + K_{AC}P_{AC} + K_{AA}P_{AA} + \left(\frac{K_{AA}P_{AA}}{K_1K_2K_{AC}P_{AC}}\right)^{\frac{1}{2}} + \left(\frac{K_1K_{AC}P_{AC}K_{AA}P_{AA}}{K_2}\right)^{\frac{1}{2}}}$$

The rate law can now be expressed in terms of equilibrium constants and partial pressures of the reactants:

$$r = \frac{k_{H_2}P_{H_2}}{\left[1 + K_{AC}P_{AC} + K_{AA}P_{AA} + \left(\frac{K_{AA}P_{AA}}{K_1K_2K_{AC}P_{AC}}\right)^{\frac{1}{2}} + \left(\frac{K_1K_{AC}P_{AC}K_{AA}P_{AA}}{K_2}\right)^{\frac{1}{2}}\right]^2}$$

(2) Molecular adsorption of acrolein as the rate-limiting step

$$r = k_{AC}P_{AC}\theta^*$$

Expressions for fractional coverages are as follows:

- Molecular acrolein adsorption

$$\theta_{AC} = \frac{K_{AA}P_{AA}}{K_1K_2K_{H_2}P_{H_2}}\theta^*$$

- Dissociative hydrogen adsorption

$$\theta_H = \left(K_{H_2}P_{H_2}\right)^{\frac{1}{2}}\theta^*$$

- Hydroxyallyl reaction intermediate

$$\theta_{HA} = \frac{K_{AA}P_{AA}}{K_2\left(K_{H_2}P_{H_2}\right)^{\frac{1}{2}}}\theta^*$$

- Allyl alcohol desorption

$$\theta_{AA} = K_{AA}P_{AA}\theta^*$$

From the site balance we obtain

$$\theta^* = \frac{1}{1 + \left(K_{H_2} P_{H_2}\right)^{\frac{1}{2}} + K_{AA} P_{AA} \left[1 + \frac{1}{K_1 K_2 K_{H_2} P_{H_2}} + \frac{1}{K_2 \left(K_{H_2} P_{H_2}\right)^{\frac{1}{2}}}\right]}$$

The rate law can now be expressed in terms of equilibrium constants and partial pressures of the reactants:

$$r = \frac{k_{AC} P_{AC}}{1 + \left(K_{H_2} P_{H_2}\right)^{\frac{1}{2}} + K_{AA} P_{AA} \left[1 + \frac{1}{K_1 K_2 K_{H_2} P_{H_2}} + \frac{1}{K_2 \left(K_{H_2} P_{H_2}\right)^{\frac{1}{2}}}\right]}$$

(3) Irreversible surface hydrogenation of acrolein to hydroxyallyl as the rate-limiting step

$$r = k_1 \theta_{AC} \theta_H$$

Expressions for fractional coverages are as follows:

- Molecular acrolein adsorption

$$\theta_{AC} = K_{AC} P_{AC} \theta^*$$

- Dissociative hydrogen adsorption

$$\theta_H = \left(K_{H_2} P_{H_2}\right)^{\frac{1}{2}} \theta^*$$

- Hydroxyallyl reaction intermediate

$$\theta_{HA} = \frac{K_{AA} P_{AA}}{K_2 \left(K_{H_2} P_{H_2}\right)^{\frac{1}{2}}} \theta^*$$

- Allyl alcohol desorption

$$\theta_{AA} = K_{AA} P_{AA} \theta^*$$

From the site balance we obtain

$$\theta^* = \frac{1}{1 + K_{AC}P_{AC} + \left(K_{H_2}P_{H_2}\right)^{\frac{1}{2}} + K_{AA}P_{AA}\left(1 + \frac{1}{K_2\left(K_{H_2}P_{H_2}\right)^{\frac{1}{2}}}\right)}$$

The rate law can now be expressed in terms of equilibrium constants and partial pressures of the reactants:

$$r = \frac{k_1 \; K_{AC}P_{AC}\left(K_{H_2}P_{H_2}\right)^{\frac{1}{2}}}{\left[1 + K_{AC}P_{AC} + \left(K_{H_2}P_{H_2}\right)^{\frac{1}{2}} + K_{AA}P_{AA}\left(1 + \frac{1}{K_2\left(K_{H_2}P_{H_2}\right)^{\frac{1}{2}}}\right)\right]^2}$$

(4) Irreversible surface hydrogenation of hydroxyallyl to allyl alcohol as the rate-limiting step

$$r = k_2\theta_{HA}\theta_H$$

Expressions for fractional coverages are as follows:

- Molecular acrolein adsorption

$$\theta_{AC} = \; K_{AC}P_{AC}\theta^*$$

- Dissociative hydrogen adsorption

$$\theta_H = \left(K_{H_2}P_{H_2}\right)^{\frac{1}{2}}\theta^*$$

- Hydroxyallyl reaction intermediate

$$\theta_{HA} = \; K_1K_{AC}P_{AC}\left(K_{H_2}P_{H_2}\right)^{\frac{1}{2}} \; \theta^*$$

- Allyl alcohol desorption

$$\theta_{AA} = \; K_{AA}P_{AA}\theta^*$$

From the site balance we obtain

$$\theta^* = \frac{1}{1 + K_{AA}P_{AA} + \left(K_{H_2}P_{H_2}\right)^{\frac{1}{2}} + K_{AC}P_{AC}\left(1 + K_1\left(K_{H_2}P_{H_2}\right)^{\frac{1}{2}}\right)}$$

The rate law can now be expressed in terms of equilibrium constants and partial pressures of the reactants:

$$r = \frac{k_2\ K_1\ K_{AC}P_{AC}K_{H_2}P_{H_2}}{\left[1 + K_{AA}P_{AA} + \left(K_{H_2}P_{H_2}\right)^{\frac{1}{2}} + K_{AC}P_{AC}\left(1 + K_1\left(K_{H_2}P_{H_2}\right)^{\frac{1}{2}}\right)\right]^2}$$

Hydrogenation of Acrolein to Propionaldehyde via n-formylethyl Reaction Intermediate

$$H_2 + 2* \overset{K_{H_2}}{\longleftrightarrow} 2H^*$$

$$AC + * \overset{K_{AC}}{\longleftrightarrow} AC^*$$

$$AC^* + H^* \overset{K_1}{\longleftrightarrow} F^* + *$$

$$F^* + H^* \overset{K_2}{\longleftrightarrow} PA^* + *$$

$$PA^* \overset{K_{PA}}{\longleftrightarrow} PA + *$$

Following is a list of rate expressions obtained by applying the same procedure as for hydrogenation of acrolein to allyl alcohol:

(1) H_2 adsorption as the rate-limiting step

$$r = \frac{k_{H_2}P_{H_2}}{\left[1 + K_{AC}P_{AC} + K_{AA}P_{AA} + \left(\frac{K_{PA}P_{PA}}{K_1K_2K_{AC}P_{AC}}\right)^{\frac{1}{2}} + \left(\frac{K_1K_{AC}P_{AC}K_{PA}P_{PA}}{K_2}\right)^{\frac{1}{2}}\right]^2}$$

(2) Molecular adsorption of acrolein as the rate-limiting step

$$r = \frac{k_{AC}P_{AC}}{1 + \left(K_{H_2}P_{H_2}\right)^{\frac{1}{2}} + K_{PA}P_{PA}\left[1 + \frac{1}{K_1K_2K_{H_2}P_{H_2}} + \frac{1}{K_2\left(K_{H_2}P_{H_2}\right)^{\frac{1}{2}}}\right]}$$

(3) Irreversible surface hydrogenation of acrolein to n-formylethyl as the rate-limiting step

$$r = \frac{k_1\ K_{AC}P_{AC}\left(K_{H_2}P_{H_2}\right)^{\frac{1}{2}}}{\left[1 + K_{AC}P_{AC} + \left(K_{H_2}P_{H_2}\right)^{\frac{1}{2}} + K_{PA}P_{PA}\left(1 + \frac{1}{K_2\left(K_{H_2}P_{H_2}\right)^{\frac{1}{2}}}\right)\right]^2}$$

(4) Irreversible surface hydrogenation of n-formylethyl to propionaldehyde as the rate-limiting step

$$r = \frac{k_2\ K_1\ K_{AC}P_{AC}K_{H_2}P_{H_2}}{\left[1 + K_{PA}P_{PA} + \left(K_{H_2}P_{H_2}\right)^{\frac{1}{2}} + K_{AC}P_{AC}\left(1 + K_1\left(K_{H_2}P_{H_2}\right)^{\frac{1}{2}}\right)\right]^2}$$

ANALYSIS OF RATE EXPRESSIONS FOR NON-COMPETITIVE ADSORPTION MODEL

Hydrogenation of Acrolein to Form Allyl Alcohol via Hydroxyallyl Intermediate

Total site balance in terms of fractional coverage of each species θ_i is

$$1 = \theta^* + \theta_i$$

The concentration of each species at equilibrium is expressed as

$$\frac{\theta_i}{1 - \theta_i} = K_iP_i$$

Following rate expressions are obtained:

- H_2 adsorption as the rate-limiting step

$$r_{H_2} = \frac{k_{H_2} P_{H_2} K_{AC} P_{AC}}{\left[(K_1 K_2 K_{AC} P_{AC})^{1/2} + (K_{AA} P_{AA})^{1/2} \right]^2}$$

- Molecular adsorption of acrolein as the rate-limiting step

$$r_{AC} = \frac{k_{AC} P_{AC} K_{H_2} P_{H_2}}{K_{H_2} P_{H_2} + \frac{K_{AA} P_{AA}}{K_1 K_2}}$$

- Irreversible surface hydrogenation of acrolein to hydroxyallyl as the rate-limiting step

$$r_1 = \frac{k_1 \, K_{AC} P_{AC} \left(K_{H_2} P_{H_2}\right)^{1/2}}{(1 + K_{AC} P_{AC}) \left(1 + \left(K_{H_2} P_{H_2}\right)^{1/2}\right)}$$

- Irreversible surface hydrogenation of hydroxyallyl to allyl alcohol as the rate-limiting step

$$r_2 = \frac{k_2 \, K_1 \, K_{AC} P_{AC} K_{H_2} P_{H_2}}{1 + \left(K_{H_2} P_{H_2}\right)^{1/2}}$$

Partial pressure of allyl alcohol is expected to be lower that of acrolein and hydrogen, so that $P_{AA} << P_{H2}$ and P_{AC}, which reduces the rate expressions to

$$r_{AC} = k_{AC} P_{AC}$$

$$r_1 = \frac{k_1 \, K_{AC} P_{AC} \left(K_{H_2} P_{H_2}\right)^{1/2}}{(1 + K_{AC} P_{AC}) \left(1 + \left(K_{H_2} P_{H_2}\right)^{1/2}\right)}$$

$$r_2 = \frac{k_2 \, K_1 \, K_{AC} P_{AC} K_{H_2} P_{H_2}}{1 + \left(K_{H_2} P_{H_2}\right)^{1/2}}$$

Assuming acrolein is weakly adsorbed on the surface, so that $K_{AC} << K_{H_2}$

$$r_1 = \frac{k_1 K_{AC} P_{AC} \left(K_{H_2} P_{H_2}\right)^{1/2}}{1 + \left(K_{H_2} P_{H_2}\right)^{1/2}}$$

$$r_2 = \frac{k_2 K_1 K_{AC} P_{AC} K_{H_2} P_{H_2}}{1 + \left(K_{H_2} P_{H_2}\right)^{1/2}}$$

As such, at high pressure rate expressions become

$$r_1 = k_1 K_{AC} P_{AC}$$

$$r_2 = \frac{k_2 K_1 K_{AC} P_{AC} K_{H_2} P_{H_2}}{1 + \left(K_{H_2} P_{H_2}\right)^{1/2}}$$

For low pressure $K_{H_2} P_{H_2} << 1$, and the rate expressions become

$$r_1 = k_1 K_{AC} P_{AC} \left(K_{H_2} P_{H_2}\right)^{1/2}$$

$$r_2 = k_2 K_1 K_{AC} P_{AC} K_{H_2} P_{H_2}$$